



NTNU – Trondheim
Norwegian University of
Science and Technology

Cooling System for High Energy Efficient Electric Motors

Kjølesystemer for energieffektive elektriske
motorer

Lars Clad

Innovative Sustainable Energy Engineering
Submission date: October 2013
Supervisor: Trygve Magne Eikevik, EPT

Norwegian University of Science and Technology
Department of Energy and Process Engineering

EPT-M-2013-32

MASTEROPPGAVE

for

Stud.techn. Lars Clad

Våren 2013

Kjølesystemer for energieffektive elektriske motorer*Cooling System for High Energy Efficient Electric Motors***Bakgrunn og målsetting**

Trenden i utvikling av elektrisk motorer er at de blir mer energieffektive med bedre virkningsgrader opp mot 97–98 %. Oppbyggingen av slike motorer fordrer en annen kjøling en tradisjonell kjøling med luft. Denne oppgaven er et samarbeid mellom institutt for elkraftteknikk og institutt for energi- og prosesseteknikk med en student fra hvert miljø som skal se på mulige løsninger for effektiv kjøling. Oppgaven vil være nært knyttet til industriell aktør. Oppgaven vil gi mulighet til å komme med nye løsninger for kjøling.

Målsetting med oppgaven er å utvikle kjølesystem for energieffektive elektriske motorer

Oppgaven bearbeides ut fra følgende punkter

1. Litteraturstudium innen oppgavens fokuspunkter
2. Evaluere ulike kjølemedier for elektriske motorer
3. Bygge en forsøksoppstilling for måling av trykktap og varmeovergang i spalter
4. Undersøke påvirkning av strømningsviersnitt, rotasjon og spaltegeometri med hensyn til trykktap og varmeovergang
5. Videreutvikle beregnings og simuleringsmodeller for motorer
6. Skrive et vitenskapelig "paper" med hovedresultater fra oppgaven
7. Forslag til eventuell videreføring av oppgaven

" - "

Senest 14 dager etter utlevering av oppgaven skal kandidaten levere/sende instituttet en detaljert fremdrift- og eventuelt forsøksplan for oppgaven til evaluering og eventuelt diskusjon med faglig ansvarlig/veiledere. Detaljer ved eventuell utførelse av dataprogrammer skal avtales nærmere i samråd med faglig ansvarlig.

Besvarelsen redigeres mest mulig som en forskningsrapport med et sammendrag både på norsk og engelsk, konklusjon, litteraturliste, innholdsfortegnelse etc. Ved utarbeidelsen av teksten skal

kandidaten legge vekt på å gjøre teksten oversiktlig og velskrevet. Med henblikk på lesning av besvarelsen er det viktig at de nødvendige henvisninger for korresponderende steder i tekst, tabeller og figurer anføres på begge steder. Ved bedømmelsen legges det stor vekt på at resultatene er grundig bearbeidet, at de oppstilles tabellarisk og/eller grafisk på en oversiktlig måte, og at de er diskutert utførlig.

Alle benyttede kilder, også muntlige opplysninger, skal oppgis på fullstendig måte. For tidsskrifter og bøker oppgis forfatter, tittel, årgang, sidetall og eventuelt figurnummer.

Det forutsettes at kandidaten tar initiativ til og holder nødvendig kontakt med faglærer og veileder(e). Kandidaten skal rette seg etter de reglementer og retningslinjer som gjelder ved alle (andre) fagmiljøer som kandidaten har kontakt med gjennom sin utførelse av oppgaven, samt etter eventuelle pålegg fra Institutt for energi- og prosesssteknikk.

Risikovurdering av kandidatens arbeid skal gjennomføres i henhold til instituttets prosedyrer. Risikovurderingen skal dokumenteres og inngå som del av besvarelsen. Hendelser relatert til kandidatens arbeid med uheldig innvirkning på helse, miljø eller sikkerhet, skal dokumenteres og inngå som en del av besvarelsen. Hvis dokumentasjonen på risikovurderingen utgjør veldig mange sider, leveres den fulle versjonen elektronisk til veileder og et utdrag inkluderes i besvarelsen.


I henhold til "Utfyllende regler til studieforskriften for teknologistudiet/sivilingeniørstudiet" ved NTNU § 20, forbeholder instituttet seg retten til å benytte alle resultater og data til undervisnings- og forskningsformål, samt til fremtidige publikasjoner.

Besvarelsen leveres digitalt i DAIM. Et faglig sammendrag med oppgavens tittel, kandidatens navn, veileders navn, årstall, instituttnavn, og NTNUs logo og navn, leveres til instituttet som en separat pdf-fil. Innlevert oppgave i Word og PDF format, sammen med separat fil for sammendrag, vitenskapelig "paper", samt alt relevant materiale brukt under utarbeidelsen av oppgaven leveres faglig ansvarlig veileder i digitalt format på en DVD/CD-rom på innlevingstidspunktet.

- Arbeid i laboratorium (vannkraftlaboratoriet, strømningsteknisk, varmeteknisk)
 Feltarbeid

NTNU, Institutt for energi- og prosesssteknikk, 16. januar 2013


Prof. Olav Bolland
Instituttleder


Prof. Trygve M. Eikevik
Faglig ansvarlig veileder

The subject of this thesis is the development of an efficient cooling system for an axial flux permanent magnetic machine. This study was carried out in cooperation between the Norwegian University of Science and Technology - NTNU and Greenway Energy LLC. The expenses for a heat transfer experiment were funded by Greenway Energy LLC, the company for which the cooling system was designed. Trygve Magne Eikevik, Professor at the Department of Energy and Process Engineering at NTNU was the supervisor of the thesis and Jon Eirik Brenvall was the contact person from Greenway Energy LLT.

The design of the coils used in the motor were content of the master thesis of Sigbjørn Lomheim and the thesis was carried out in close cooperation with him. This collaboration was especially close during the development of the geometry for the heat transfer experiment. Measurements of material properties that were used in the experimental setup were carried out by Ignat Tolstorebrov and Christian Schlemminger. The experimental geometry was manufactured by Øystein Gjervan Hagemo. Odin Hoff Gardå assisted the student with the installation and calibration of the measurement equipment. During the work in the lab, Reidar Tellebon assisted with advise concerning mechanical issues.

The presented master thesis was the continuation to the project work that was carried out in fall 2012. Some of the content of this work were included in this thesis.

Freiburg, October 31, 2013

Lars Johan Clad

Abstract

The development of an efficient cooling system for an axial magnetic flux machine was the subject of the presented master thesis. Throughout the study, an experimental model was designed which offers the possibility to investigate the cooling performance of the presented cooling system in dependence of various design parameters. The model was designed in a way that the coil element which is embedded in the geometry is interchangeable which enables the testing of different stator layouts and coil materials with the presented model. In addition to the experimental setup, a numerical simulation model was created, allowing the comparison between the obtained results. For this simulation model a thorough study of the influence of the mesh size parameters in different regions on the resulting solution quality was carried out.

With the presented experimental model, the performance of the developed cooling system was investigated and subsequently compared to the results obtained from numerical simulations. The deviation between the simulated and measured values were marginal and demonstrated that the developed cooling system fulfills all demands that were set.

By the experimental and numerical investigation, additional design parameters which showed to be of great importance were identified besides the ones that were studied in detail with an analytical heat transfer model. Also the analytical model was compared to results from numerical simulations. Based on the fact that both numerical simulation setups were modeling the heat transfer problem using the same physical models and showed good accordance to the corresponding analytical and experimental results, it was concluded that the analytical model and the 2D-simulation model deliver reliable results for the average surface heat transfer coefficient for laminar flow regimes. Based on the outcomes of the thesis, possible ways to further improve the performance of the presented cooling system were outlined and recommendations for future work were given.

List of Figures

- 1.1 Layout of the motor 3

- 4.1 Thermal setup of the heat transfer problem. 12
- 4.2 Section view of the motor design, illustrating the flow path of the coolant entering the motor through holes in the stator and flowing radially outwards over the coils. The flow of the cooling fluid is marked with blue arrows. . . 15
- 4.3 Section view of the motor design, illustrating the flow path of the coolant entering the motor through the motor shaft and flowing radially outwards over the coils. The flow of the cooling fluid is marked with blue arrows. . . 15

- 5.1 Setup of the heat transfer problem described by the analytical model. . . . 20
- 5.2 Flowchart of the MATLAB code used to study the influence of different parameters on the heat transfer for the analytical laminar flow model with one heated plate. 25

- 6.1 Setup of the heat transfer problem described in section 5.1 in COMSOL. . . 26
- 6.2 Sector of the structured, graded mesh, which was used for the velocity-sweep simulation. 27

- 7.1 In the experiment a sector of the motor is modeled as shown in the figure. 29
- 7.2 Comparison of a sector of the motor coil (a) and the coil element modeling the active part of the sector in the experiment (b). 30
- 7.3 Overview of the experimental model consisting of two separate parts. The lower part models the stator while the upper part models the rotor. 31
- 7.4 Top-view of the lower part of the experimental model. The flow path of the coolant is marked with blue arrows. 32
- 7.5 Sectional view of the model along the symmetry axis (Figure 7.4) 32
- 7.6 Overview of the measurement setup. 35

7.7	Geometry which was used in the simulation setup, representing the area in which water will be able to flow. A prolonged inlet, showed to be an effective tool to reduce the turbulences, which led to a non-uniformity in the velocity profile.	38
7.8	Measured resistance of the coil element in dependence of temperature. . . .	42
7.9	Overview of the experimental setup in the lab.	44
8.1	Overview of the setup used to simulate the heat transfer experiment in COMSOL.	53
8.2	Exploded view of the simulation model.	56
8.3	Influence of the total number of mesh elements on the calculated values of $\bar{\alpha}$ and T_c	57
8.4	Simulation results for T_c in dependence of the minimum and maximum element size limits for the boundary mesh between the heated area and water.	58
9.1	Influence of the mean fluid velocity, \bar{u} , on the fluid outlet temperature, T_{out} , and the heat transfer rate, \dot{Q}	63
9.2	Influence of the mean fluid velocity on the heat transfer per mass unit. . .	64
9.3	Influence of the mean fluid velocity on the rate of change of the heat that is transferred per mass unit.	65
9.4	Influence of the mean fluid velocity, \bar{u} , on the resulting Reynolds number, Re , and average Nusselt number, Nu	65
9.5	Influence of the plate distance, d , on the fluid outlet temperature, T_{out} , and the heat transfer rate, \dot{Q}	66
9.6	Influence of the mean fluid velocity on the heat transfer per mass unit. . .	67
9.7	Influence of the plate distance on the rate of change of the heat that is transferred per mass unit.	67
9.8	Influence of the plate distance, d , on the resulting Reynolds number, Re , and average Nusselt number, Nu	68
9.9	Influence of the heated plate length, L , on the fluid outlet temperature, T_{out} , and the heat transfer rate, \dot{Q}	69
9.10	Influence of the heated plate length, L , on the resulting Reynolds number, Re , and average Nusselt number, Nu	69
10.1	Comparison between the results from the analytical model and numerical simulation for the heat transfer problem with one heated plate and laminar flow.	71

11.1	Resulting average coil element temperature which was measured with nonuniform flow distribution throughout across the coil element.	72
11.2	Resulting average coil element temperature at maximal current and flow rate. At $t = 165$ s, the current was switched off.	73
12.1	Comparison of the experimental and simulation results for $\bar{\alpha}$ in dependence of the mass flow rate at a gap width of 2 mm.	74
12.2	Comparison of the experimental and simulation results for $\bar{\alpha}$ in dependence of the mass flow rate at a gap width of 4 mm.	77
13.1	Comparison of $\bar{\alpha}$ and $\bar{\alpha}_{T_s}$ for a gap width of 2 mm.	79
13.2	Comparison of $\bar{\alpha}$ and $\bar{\alpha}_{T_s}$ for a gap width of 4 mm.	79

List of Tables

4.1	Comparison of the characteristics of water and air when used as a cooling fluid.	17
5.1	Default initial conditions and parameters used in MATLAB code.	23
6.1	Boundary conditions that were used in the simulation.	26
7.1	Selection list of materials considered to model lamination steel.	41
7.2	Properties of the materials used in the experimental model. The listed values were measured or taken from[19, 1, 3].	42
7.3	Constants for different geometries used in equation 7.20	48
8.1	Boundary conditions that were applied in the simulation model.	54
8.2	Element size limits of boundary mesh and resulting total number of mesh elements and calculated value of T_c	58
8.3	Mesh-parameters that were used in the simulation.	59
9.1	Parameters that were held constant during the fluid velocity sweep.	62
9.2	Values of the gradient $d\dot{Q}/d\bar{u}$ in different fluid velocity regions.	63
9.3	Parameters that were held constant during the fluid plate distance sweep.	65
9.4	Parameters that were held constant during the parameter sweep of the heated plate length.	68
9.5	Increase of \dot{Q} and T_{out} resulting from adding half a meter to the plate length for different initial plate lengths.	69
12.1	Overview of the results obtained from numerical simulations and experiment for a gap width of 2 mm.	75
12.2	Overview of the results obtained from numerical simulations and experiment for a gap width of 4 mm.	76
13.1	Simulation results for a gap width of 2 mm.	78

13.2 Simulation results for a gap width of 4 mm.	79
17.1 Simulated coil element and water temperatures for different flow rates. . .	87

Nomenclature

Latin Letters

A	m^2	Area
b	m	plate width
c_p	$\text{J kg}^{-1} \text{K}^{-1}$	Specific heat capacity
d	m	plate distance
Gr	–	Grashof number
g	m s^{-2}	gravitational acceleration
I	A	current
L	m	plate length
L_e	m	entrance length
\dot{m}	kg s^{-1}	Mass flow rate
Nu	–	Nusselt number
\overline{Nu}	–	average Nusselt number
Nu_x	–	local Nusselt number
Pr	–	Prandtl number
\dot{q}	W m^{-2}	heat flux per unit area
\dot{Q}	W	heat transfer rate
Re	–	Reynolds number
R_l	Ωm^{-1}	electrical resistance per meter
R	Ω	electrical resistance
J	A m^{-2}	current density
A_c	m^2	conductor cross section area
d_c	m^2	conductor thickness in y-direction
d_h	m	hydraulic diameter
T	$^{\circ}\text{C}$	temperature
\overline{T}	$^{\circ}\text{C}$	mean temperature
T_{in}	$^{\circ}\text{C}$	fluid temperature at the inlet
T_{max}	$^{\circ}\text{C}$	temperature of the coil element at hottest position
T_c	$^{\circ}\text{C}$	average surface temperature of the coil element on cooled side
T_{diff}	$^{\circ}\text{C}$	difference in calculated temperature between two iterations

T_{cout}	°C	calculated fluid temperature at the outlet
T_w	°C	surface temperature of the heated plate
T_m	°C	average fluid temperature after heat transfer area
T_{out}	°C	fluid temperature at the outlet
T_f	°C	film temperature
T_∞	°C	fluid temperature outside the thermal boundary layer
$LMTD$	°C	logarithmic temperature difference
u	m s^{-1}	fluid velocity
U	$\text{W m}^{-2} \text{K}^{-1}$	thermal conductance
V	V	voltage
V_c	V	voltage drop across coil element inside area of interest
u	m s^{-1}	fluid velocity
u_f	m s^{-1}	free stream velocity
\bar{u}	m s^{-1}	mean fluid velocity along the plate length
b	m	distance from the leading edge
b_0	m	distance from the leading edge at which the heating begins
y	m	distance to the wall (in normal direction to the wall surface)
Δx_{stat}	–	statistical uncertainty
S	–	standard deviation
n	–	number of measurements
t	–	correction factor Student's t-distribution

Greek Letters

α	$\text{W m}^{-2} \text{K}^{-1}$	surface heat transfer coefficient
$\Delta \bar{\alpha}_-$	$\text{W m}^{-2} \text{K}^{-1}$	measurement uncertainty of $\bar{\alpha}$ in negative direction
$\Delta \bar{\alpha}_+$	$\text{W m}^{-2} \text{K}^{-1}$	measurement uncertainty of $\bar{\alpha}$ in positive direction
$\bar{\alpha}$	$\text{W m}^{-2} \text{K}^{-1}$	average surface heat transfer coefficient
α_x	$\text{W m}^{-2} \text{K}^{-1}$	local surface heat transfer coefficient
γ	K^{-1}	linear temperature coefficient of resistance
β	–	thermal expansion coefficient
δ_h	m	hydraulic boundary layer thickness
δ_t	m	thermal boundary layer thickness
κ	$\text{W m}^{-1} \text{K}^{-1}$	thermal conductivity
l	m	characteristic length
μ	Pa s	dynamic viscosity
ν	$\text{m}^2 \text{s}^{-1}$	kinematic viscosity
ρ	kg m^{-3}	density
σ	S m^{-1}	electrical conductivity
τ	Pa	shear stress

Subscripts

<i>al</i>	aluminum
<i>air</i>	air
<i>b</i>	bottom
<i>cond</i>	conduction
<i>#</i>	Number of thermocouple
<i>ht</i>	Heat-Transfer
<i>i</i>	inner
<i>POM</i>	POM
<i>r</i>	room
<i>sys</i>	systematic uncertainty
<i>stat</i>	statistical uncertainty
<i>si</i>	Silicone
<i>s</i>	Surface
<i>w</i>	Water

Abbreviations

AFPM Axial flux permanent magnetic

POM polyoxymethylene

Contents

Abstract	iii
Nomenclature	ix
Abbreviations	xii
I Introduction	1
1 Introduction	2
1.1 Thesis structure	2
1.2 Motor layout	3
1.3 Demands on the cooling system	4
2 Literature Review	5
2.1 Heat transfer models - analytical approach	5
2.2 Heat transfer models based on numerical simulations	6
2.3 Cooling methods for AFPM machines	7
3 Theory	8
3.1 The hydrodynamic boundary layer	8
3.2 Transition from laminar to turbulent flow	9
3.3 The thermal boundary layer	10
4 Key problem and fundamental considerations	12
4.1 Description of the key problem	12
4.2 Choice of the coolant flow path	14
4.3 Air cooling vs. water cooling	16

II	Methods	18
5	Analytical Heat Transfer Model	19
5.1	Model Layout	19
5.2	Definitions used in the model	20
5.3	Mathematical Modeling	22
5.4	MATLAB code	23
6	2D Heat transfer simulation	26
7	Development of the heat transfer experiment	28
7.1	Aim of the experiment	28
7.2	Layout	28
7.3	Measuring method	30
7.3.1	Measurement principle	30
7.3.2	Measurement setup	34
7.3.3	Calculation errors	36
7.4	Calibration of thermocouples	37
7.5	Flow considerations	37
7.5.1	Jet effect - horizontal water inlet	37
7.5.2	Turbulences at the inlet-angle	38
7.6	Materials	39
7.6.1	Material selection	39
7.6.2	Material properties	41
7.7	Fabrication	43
7.8	Experimental procedure	43
7.8.1	Setup	43
7.8.2	Procedure and data acquisition	45
7.9	Estimation of the measurement accuracy	45
7.9.1	Measurement uncertainties	45
7.9.2	Heat transferred to surrounding	47
7.9.3	Propagation of uncertainty	50
8	Numerical simulation of the experimental setup	52
8.1	Setup	52
8.2	Boundary conditions and physical modeling	53
8.3	Solver	55
8.4	Mesh	55
8.4.1	Influence of the number of mesh elements	56

8.4.2	Influence of the boundary between heated area and water	57
8.5	Evaluation	59
III	Results	61
9	Analytical heat transfer model	62
9.1	Influence of the fluid velocity	62
9.2	Influence of the plate distance	64
9.3	Influence of the heated plate length	68
10	2D Heat transfer simulation	71
11	Experiment	72
11.1	Nonuniform flow	72
11.2	Maximum cooling capacity	73
12	Comparison of experimental and simulation results	74
12.0.1	Results obtained with a 2 mm gap width	75
12.0.2	Results obtained with a 4 mm gap width	76
13	Simulation	78
IV	Discussion	81
14	Analytical heat transfer model	82
14.1	Influence of the fluid velocity	82
14.2	Influence of the plate distance	82
14.3	Influence of the heated plate length	83
15	2D Heat transfer simulation	84
16	Experiment	85
17	Comparison of experimental and simulation results	86
18	Simulation	89
V	Conclusions	91
19	Experiment	92

20 Simulation	94
21 Overall outcome of the thesis	95
22 Recommendations for future work	97
Bibliography	99
Appendix	101
Appendix A	103
A.1 Risk-report	103
A.2 Risk-report appendix	103

Part I

Introduction

1 | Introduction

Modern axial flux permanent magnetic (AFPM) machines are highly energy efficient and offer a high power-to-weight ratio due to their compact design. These features make AFPM machines versatile applicable and considerable research has been done on the electrical design of AFPM machines throughout the last few years. Cooling of AFPM machines has, however, proven to be problematic due to their compactness and high power output. This is a critical problem of AFPM machines since high operating temperatures limit the power output, the electrical efficiency and the lifetime of the engine. However, the importance of an efficient cooling system is often underestimated and up to date only little focus was put on the research concerning the thermal design of AFPM machines [4].

Therefore, the aim of this thesis is to develop the electrical design hand in hand with the thermal design of an AFPM machine in order to optimize the overall performance of the machine by considering both, electrical and thermal demands in the layout. The objective of this work is to design an efficient cooling system for an AFPM machine in close cooperation with Sigbjørn Lomheim (Dep. of Electric Power Engineering), who is in charge of the electrical layout of the engine. This study builds the baseline for a master-thesis, which will continue the development of the AFPM machine.

1.1 Thesis structure

The presented thesis is divided into five main parts. In the first part, the Introduction, an overview of the motor for which the cooling system was designed is given. This part of the thesis also includes a literature review, an overview of the theory background and a description of fundamental considerations.

In the second part the methods that were used to obtain the results of the thesis are described. In the third part the results are presented, followed by their discussion in the fourth main part. The fifth and last part of the thesis presents the conclusions that were made based on the obtained results.

1.2 Motor layout

As already mentioned, the studied motor is an axial flux permanent magnet machine. Thus the magnetic field flows parallel to its axis, in contrast to radial flux machines, where the magnetic field flows in radial direction. This allows a thinner and more compact design of the motor, leading to a high power density and large torque. An overview of the motor layout, which was designed and drawn by Sigbjørn Lomheim, is given in figure 1.1 through a 3D-drawing of the design.

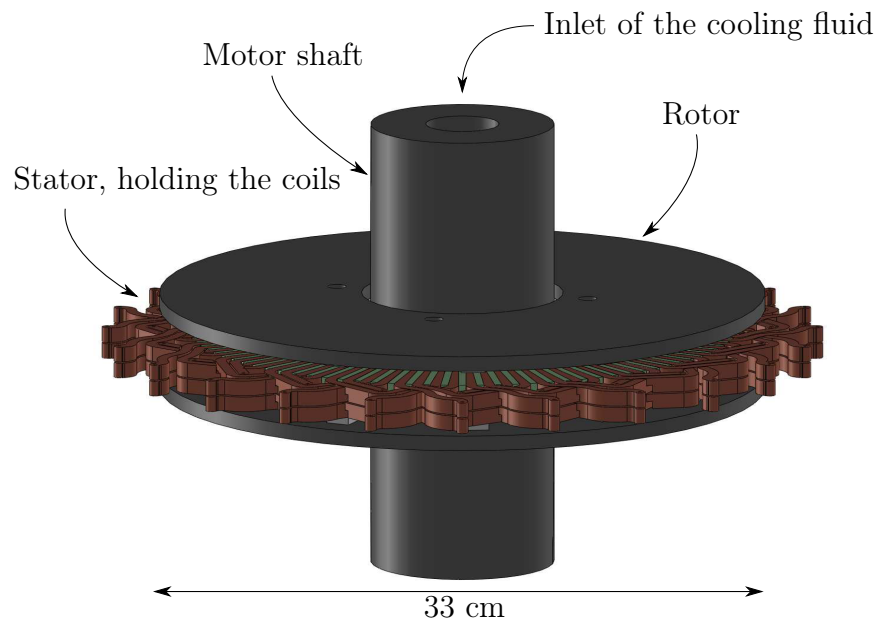


Figure 1.1: Layout of the motor

The main advantage of the motor from the thermal design point of view is that the coils form a plane surface, which is accessible for the cooling fluid. This large surface facilitates the cooling, leading to a lower operating temperature, which in turn increases the efficiency and lifetime of the motor [6].

Besides the advantages from a thermal point of view the layout of the motor holds various other important advantages such as:

- large power density of about 670 W/kg
- compact design, leading to a small size and increased applicability
- front and back of the motor are flat, facilitating the installation of the motor
- high power density enables quick changes in speed
- easy manufacturing of the coils based on the coil design

These characteristics make the presented machine applicable for different areas of use, requiring large torque and power densities such as Stirling systems [23] and electrical vehicles [12, 7]. But the layout of the machine is not limited to the application as a motor but could also be used as a generator, for example in wind mills [20].

1.3 Demands on the cooling system

The demands on the cooling system of the motor can be summarized to the following main characteristics that need to be fulfilled:

- Ensure sufficient cooling of the entire machine during rotation as well as when the motor stands still at constant torque.
- Cooling capacity of approximately 40 kW/m^2
- The cooling fluid has to be compatible with the electrical layout of the machine
- To limit the losses in the coils, the coil temperature should be kept below $90 \text{ }^\circ\text{C}$ at all times
- An even temperature distribution across the coil is favorable

2 | Literature Review

Although the thermal design of AFPM machines is of great significance to the overall performance as well as on the life time of the machine only little research work has been carried out in this area throughout the last decade [4]. In general research, which is done concerning the thermal design of AFPM machines can be divided into two groups. The analysis of the cooling performance based on an analytical approach and on the other hand the approach by numerical simulations.

2.1 Heat transfer models - analytical approach

Numerical simulations of the thermal characteristic of axial flux permanent magnetic (AFPM) machines require large computational resources. This slows down the development process, especially when the influence of different design parameters are unknown. To accelerate the development of the thermal layout of this type of machines a number of models have been developed to describe the heat transfer in AFPM machines.

A model for the heat transfer in air cooled AFPM machines was developed and presented by [21]. Starting from the assumption of the rotor being an ideal impeller the velocity distribution was modeled in 1D. This basic model was then extended by including pressure losses occurring throughout the fluid path and taking recalculations into account. This was done in order to predict the mass flow rate of the air through the machine. Additionally a thermal model of the losses inside the machine was set up as a resistance circuit. The average Nusselt number was estimated by existing correlations for rotating disks. The results of this model were subsequently compared to experimental data, which was obtained from a prototype of the machine. The big advantage of such a model is that it enables a quick estimation of the temperature of the windings and the cooling capacity of the system. However, the comparison between the developed model with the experimental results showed a difference of more than 10 °C. At a measured temperature of about 45 °C this is a relatively large variation.

Another thermal model for an air cooled AFPM machine was presented by [20]. Just as the model of [21] this model was based on analytical correlations to estimate the fluid flow

in the machine. The model for transient temperature analysis had the main aim to enable the quick estimation of the influence of different design parameters on the temperature that can be expected inside the machine. From the thermal model it was concluded that the temperature of the inlet air has a large influence on the maximum temperature value, while the surrounding temperature as well as the gap-ratio do not have a big effect on this value. Unlike the results of [21] the obtained correlations were not compared to experimental data. Thus, the obtained results should be used as a general guideline for the principle influence of the different parameters, rather than expecting an exact solution of the problem. A general disadvantage of both thermal models presented by [21, 20] was pointed out by [2]. For both heat transfer models variables such as values for heat transfer coefficients need to be estimated or found experimentally before the model can be used.

A lumped parameter model was developed by [14], describing the steady state temperature distribution inside an air cooled AFPM machine. In contrast to the analytically derived models [21, 20], the machine was divided into several control volumes and connected by thermal impedances. The results which were calculated using the lumped parameter model were compared to experimental results as well as CFD-simulation results and showed to be comparably accurate. However, also in this model the heat transfer coefficient needs to be estimated before the model can be used. When this was done by CFD-simulations and the calculated heat transfer coefficient value was used in the presented model, the obtained results were considerably improved compared to the obtained results with the heat transfer coefficient derived from correlations.

2.2 Heat transfer models based on numerical simulations

One of the main advantages of an approach of the heat transfer problem in AFPM machines using numerical simulations is the ability to simulate any geometry. However, the computation time can be very high, which is why correlations for the heat transfer have been investigated depending on different design parameters.

Based on the lack of correlations for the local heat transfer coefficient for rotating discs with geometries standing out of the surface, the study presented by [2] aimed to find a correlation for this problem. The local heat transfer coefficient across the stator surface was calculated by simulating the heat transfer problem in a CFD program (Fluent). Two peaks of the local heat transfer coefficient were obtained, one in the region of the leading edge and the other one at the outer edge of the stator. A linear increase of the heat transfer coefficient with an increase in rotational speed was observed.

In [16] the cooling performance of an air cooled AFPM machine was analyzed with

the help of the finite-element-method applied in three dimensions. A lumped parameter analysis was used to model the steady state situation of the machine. The results which were obtained from the simulation were subsequently compared to experimental data. The study showed an increase of the heat transfer coefficient in radial direction due to the rotation of the motor, while the core of it was much hotter than expected. Furthermore, the results showed to be largely dependent on the accuracy of the boundary conditions.

From this and the previous section and can be seen that the thermal modeling of the heat transfer taking place in an AFPM machine is a complex problem. The most difficult value to find is the surface heat transfer coefficient which is mainly influenced by convectional heat transfer.

2.3 Cooling methods for AFPM machines

Most AFPM machines are cooled with air or water being used as cooling fluid [2, 21, 20]. If air is used as coolant, usually the the air-gap between rotor and stator is used as flow path, offering a large surface area and facilitating the cooling process [6]. When water is utilized as cooling fluid, this normally is done through leading flow channels along the casing. The stator is then cooled by being in thermal contact with the stator and the cooling of the coils takes place by air cooling. This way of cooling is however not the most efficient way since a large number of thermal resistances limit the cooling performance [5].

A water-cooled AFPM machine was presented by [7], which was used as direct drive wheel motor. Demineralized water was filled into the completely closed housing of the motor. Thus the water got in direct contact with the winding, which led to an highly effective cooling performance. Through this the motor could be used in 100% and a very compact design was achieved. A water to air cooling system was utilized for cooling the water down to a specified upper temperature before it reentered the machine. Copper with an insulation layer on the outer surface was chosen as coil material. The temperature increase throughout the motor was kept relatively low by a water circulation of several l/min. This design was reported to be very light, efficient and also well suited for other applications such as in generators.

3 | Theory

This chapter provides the basic theory needed to understand this work. Primarily the hydraulic boundary layer and its development is described, followed by the theoretical background of the transition from laminar to turbulent flow. With the help of the law of the wall the distribution between the laminar boundary layer and the turbulent core is described. This chapter concludes with the theory concerning the development of the thermal boundary layer for a flow across a flat plate. The information in this chapter was taken from [10, 22].

3.1 The hydrodynamic boundary layer

For any flow problem the fluid velocity is zero at the wall, leading to viscous forces acting on the fluid. Due to these forces, a profile of the fluid velocity will begin to develop in normal direction to the wall, starting from the leading edge. The viscous forces between the fluid layers acting in this region are described by the so called *shear stress* (τ)

$$\tau = \mu \frac{du}{dy} \quad (3.1)$$

where μ is the dynamic viscosity, which is a temperature dependent fluid property, u is the fluid velocity and y is the normal distance to the wall. The developing velocity profile is very thin at the beginning of the wall and expands with increasing distances from the leading edge. The region in which the velocity profile develops is called *boundary layer*. Its thickness in y -direction is defined as the distance from the wall where the fluid velocity reaches 99 % of the free stream velocity (u_f).

The hydraulic boundary layer thickness (δ_h) for a flat plate in dependence on the distance from the leading edge (b) is given by

$$\delta_h = \frac{5 b}{\sqrt{Re_x}}. \quad (3.2)$$

with Re_x being the local Reynolds number.

When a pipe flow is considered the flow is called to be *fully developed*, when the boundary layer reaches a thickness of the pipe radius and thus gets in contact with the boundary layer originating from the opposite side of the pipe. The distance from the pipe inlet at which this happens is called *entrance length* (L_e).

3.2 Transition from laminar to turbulent flow

At a specific fluid velocity, the flow will start a transition process from laminar to turbulent flow. The region of transition is dominated by chaotic flow directions leading to a mixing of the fluid.

At which fluid velocity this transition occurs, is dependent on the fluid properties as well as the geometry of the pipe and is usually expressed by the *Reynolds number* (Re)

$$Re = \frac{\bar{u} l \rho}{\mu} = \frac{\bar{u} l}{\nu} \quad (3.3)$$

where \bar{u} is the mean fluid velocity, ρ is the density and ν is the kinematic viscosity of the fluid. l is a characteristic length, which depends on the flow problem. In a pipe flow l is the pipe diameter and for a flow over a plain plate l is the distance from the leading edge. The value of the Reynolds number at which transition takes place is largely dependent on the flow problem, its geometry and on parameters such as the surface roughness. However, a number of critical Reynolds number values have been set for various flow problems and are widely accepted. For the flow over a plane plate the critical value of Re at which the flow turns turbulent is about $5 \cdot 10^5$, while a pipe flow is considered turbulent at values of Re above 10^4 .

The turbulent flow consists of a turbulent core, a thin laminar sub-layer and a buffer layer in between them. The velocity profile for turbulent flows is described by *the law of the wall*, which will be explained in the following section.

3.3 The thermal boundary layer

In the same way as a hydrodynamic boundary layer is developed when a fluid flow gets in contact with a wall (section 3.1), a thermal boundary layer is formed when a fluid flows across the surface of a heated plate. This thermal boundary layer, in which temperature gradients exist, starts to develop at the point at which the fluid gets in contact with the heated plate and grows in thickness in flow direction.

At the surface of the plate the fluid velocity is zero, thus the heat transfer will take place by conduction. To fulfill conservation of energy at the wall the following condition must be satisfied:

$$\dot{q} = -\kappa \frac{\partial T}{\partial y_s} = \alpha (T_s - T_\infty) \quad (3.4)$$

where \dot{q} is the heat flux per unit area, κ the thermal conductivity of the fluid, $\partial T/\partial y_s$ the temperature gradient at the plate surface, α the surface heat transfer coefficient, T_s the surface temperature of the plate, and T_∞ the fluid temperature outside the thermal boundary layer.

By considering the boundary conditions and mathematical transformation it can be shown that the thermal boundary layer thickness δ_t can be calculated to

$$\delta_t = \delta_h \frac{1}{1.026} Pr^{-1/3} \left(1 - \left(\frac{b_0}{b} \right)^{3/4} \right)^{1/3} \quad (3.5)$$

where δ_h is the hydraulic boundary layer thickness (see section 3.1), Pr the Prandtl number of the fluid (a temperature dependent fluid property), b_0 the distance from the leading edge at which the heating begins, and b is the distance from the leading edge. The Prandtl number is defined as

$$Pr = \frac{c_p \mu}{\kappa} \quad (3.6)$$

where c_p is the Specific heat capacity of the fluid. The Prandtl number relates the thickness of the hydraulic boundary layer with the thermal boundary layer thickness. This relation is approximately given by

$$\frac{\delta_h}{\delta_t} \approx Pr^{1/3}. \quad (3.7)$$

For fluids with a Prandtl number higher than 0,7, equation 3.5 can be rewritten to:

$$Nu_x = 0,322 Pr^{1/3} Re_x^{1/2} \left(1 - \left(\frac{b_0}{b} \right)^{3/4} \right)^{-1/3} \quad (3.8)$$

with

$$Nu_x = \frac{\alpha_x b}{\kappa} \quad (3.9)$$

where Nu_x is the local Nusselt number, Re_x the Reynolds number at the distance b from the leading edge of the plate, and α_x the local surface heat transfer coefficient. The Nusselt number is a measure for the temperature gradient at the surface. Heat transfer correlations deliver values of the Nusselt number from which the surface heat transfer coefficient can be found.

4 | Key problem and fundamental considerations

In this chapter an outline of the key problem for the design of the cooling system is given. Following, fundamental considerations that were made before starting with the actual development of the system are presented. These include the choice of the flow path of the coolant as well as a comparison between the characteristics of water and air as cooling fluid.

4.1 Description of the key problem

This section aims to describe the main problem for the development of an efficient cooling system for the motor and is based on the information given in [10]. To do this a conductor, which is thermally insulated on the one side and cooled by a cooling fluid flowing across its surface on the other side, as it is illustrated in figure 4.1.

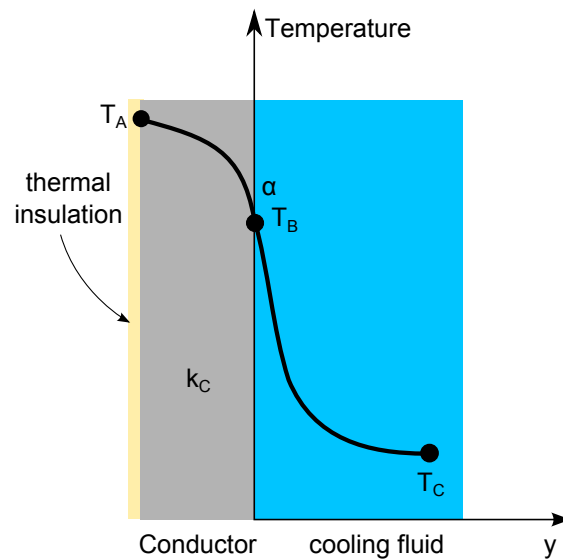


Figure 4.1: Thermal setup of the heat transfer problem.

When the non-cooled side is perfectly insulated, all heat is transferred through the coolant and given to

$$\dot{Q} = \dot{m} c_p \Delta T_{fluid} = \alpha A (T_B - T_C) \quad (4.1)$$

where \dot{Q} is the heat transfer rate, \dot{m} the fluid Mass flow rate, c_p the Specific heat capacity of the fluid, T_{fluid} is the temperature increase of the fluid due to the heat transfer, α the surface heat transfer coefficient, A the heat transfer area, and $(T_B - T_C)$ is the temperature difference in the fluid.

When all heat, generated by the electric current flowing through the conductor, is dissipated through the cooling fluid, the temperature distribution declines in a parabolic shape in positive y-direction from the thermally insulated side of the conductor to its cooled surface. The temperature distribution can be written to:

$$\dot{q} = (T_A - T_B) \frac{\kappa_c}{d_c^2} = J^2 A_c R_l \quad (4.2)$$

where \dot{q} is the heat flux per unit area, $(T_A - T_B)$ is the temperature difference inside the conductor, κ_c the thermal conductivity of the conductor, d_c the conductor thickness in y-direction, A_c the conductor cross section area, and R_l the electrical resistance per meter.

Consequently, the following equation must be satisfied for steady state conditions:

$$\alpha (T_B - T_C) = (T_A - T_B) \frac{\kappa_c}{d_c^2} \quad (4.3)$$

In equation 7.1 all variables are known or can be measured when the material of the conductor is selected besides the surface heat transfer coefficient (α). The value of α is largely dependent on the cooling fluid and the flow across the surface that is to be cooled. The estimation of the α -value will be the main subject of the rest of the report.

4.2 Choice of the coolant flow path

Two different ways of inserting the cooling fluid into the motor were considered, which were based on the fundamental design of the motor which was developed by Greenway Energy LLC. These two options were to either insert the fluid through holes in the rotor disk as illustrated in Figure 4.2 or through the motor shaft as shown schematically in Figure 4.3. The advantage of the first option is that coil regions with higher current densities which lead to larger resistive losses and consequently increased heat generation can be cooled in an efficient way by placing holes above these regions. On the other hand option two ensures the cooling of the coils over their entire length (in radial direction) since the cooling fluid enters the motor closer to the axis of rotation. Moreover, this option allows the addition of further rotor-stator layers without requiring larger changes of the overall design. However, a combination of both options might be the best solution, combining the advantages of both of them.

Since the engine is still in development and the final coil design was the subject of the master thesis of Sigbjørn Lomheim [15], no final decision has yet been taken on how the coolant should enter the motor. However, the main characteristics of both options are the same. In both options the air gap between rotor and stator is used as flow path of the coolant and in both of the options the cooling fluid flows across the entire stator surface. Therefore, other design parameters such as the influence of the air gap on the cooling performance were studied in this work, independently of the final choice of the entrance method of the cooling fluid.

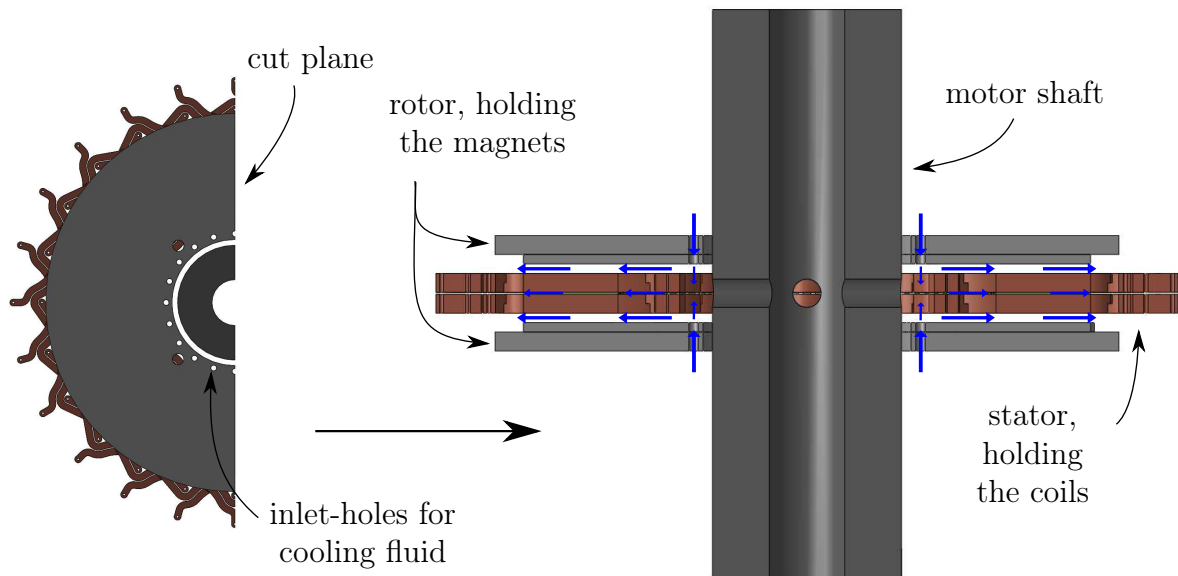


Figure 4.2: Section view of the motor design, illustrating the flow path of the coolant entering the motor through holes in the stator and flowing radially outwards over the coils. The flow of the cooling fluid is marked with blue arrows.

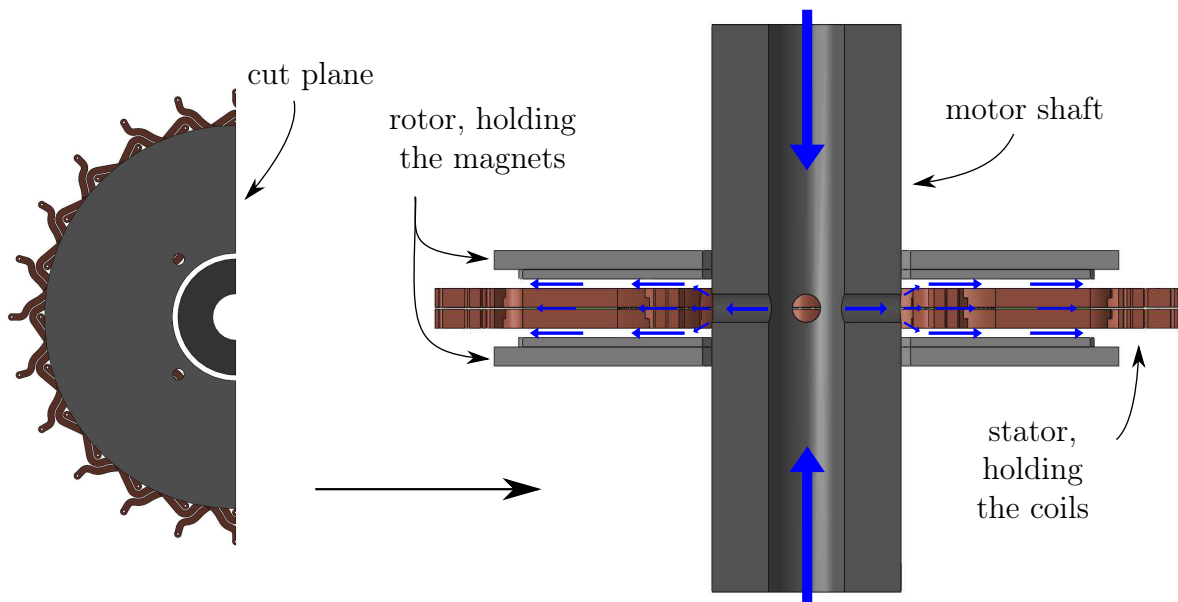


Figure 4.3: Section view of the motor design, illustrating the flow path of the coolant entering the motor through the motor shaft and flowing radially outwards over the coils. The flow of the cooling fluid is marked with blue arrows.

4.3 Air cooling vs. water cooling

One of the most important decisions for the design of a cooling system is the choice of the cooling fluid. In this study air and water, which are both widely used as coolants, were considered possible choices. These two fluids were therefore compared to each other in respect to their characteristics as cooling fluids. In section 3.3 of the theory chapter the Nusselt number and its importance on the heat transfer was addressed. It was stated that the local Nusselt number (Nu_x) for the flow over a plane plate can be calculated to

$$Nu_x = 0,322 Pr^{1/3} Re_x^{1/2} \left(1 - \left(\frac{b_0}{b}\right)^{3/4}\right)^{-1/3} = \frac{\alpha_x b}{\kappa} \quad (4.4)$$

where Re_x is the Reynolds number at a distance b from the leading edge. Solving equation 4.4 for the local surface heat transfer coefficient (α_x) yields:

$$\alpha_x = 0,322 Pr^{1/3} Re_x^{1/2} \left(1 - \left(\frac{b_0}{b}\right)^{3/4}\right)^{-1/3} \frac{\kappa}{b} \quad (4.5)$$

To compare water and air to each other when used as cooling fluid, the local surface heat transfer coefficient term $Pr^{1/3} Re_x^{1/2} \kappa$ was calculated for a temperature range $0^\circ\text{C} \leq T \leq 100^\circ\text{C}$. In this comparison b was set to 4 mm and u_f to 1 m/s. The fluid properties were taken from [13] and the results of this comparison are listed in table 4.1.

An observation of table 4.1 shows that the calculated value of the term $Pr^{1/3} Re_x^{1/2} \kappa$ for water is 167-times higher than the one of air at a temperature of 0°C . At a temperature of 100°C the obtained value for water is even 259-fold compared to the one of air.

This comparison demonstrates that even if the Reynolds number for the air cooling is increased significantly, the local surface heat transfer coefficient of the water cooled system will still be substantially higher. Therefore, water was chosen as coolant in this study, although water cooling of electrical systems is connected with additional problems such as the indispensability of sufficient electrical insulation of the electrical parts.

Table 4.1: Comparison of the characteristics of water and air when used as a cooling fluid.

Temperature in °C	$(Pr^{1/3} Re_x^{1/2} \kappa)$ in W/mK	
	Water	Air
0	63,08	0,3768
20	72,30	0,3736
40	80,11	0,3713
60	86,49	0,3697
80	91,53	0,3683
100	95,38	0,3677

Part II

Methods

5 | Analytical Heat Transfer Model

As already mentioned earlier, the value of the heat transfer coefficient at the surface of the coils across which the cooling fluid flows, is one of the key factors for the thermal design of the motor and it is therefore crucial to estimate its value in a realistic way. The heat transfer coefficient is, however, influenced by various design parameters that need to be matched in order to optimize the cooling performance of the system.

Before this can be done the key design parameters need to be identified and the influence of each of them on the heat transfer coefficient needs to be studied. This was done with the help of an analytical model of the heat transfer for a flow between two parallel plates. This model was chosen since it comes close to the situation of the motor when standing still. As it was already mentioned in section 4.3 water was chosen as cooling fluid, which is why the analytical model was only carried out for water as fluid. The analytical model used in this chapter was taken from [13].

5.1 Model Layout

The analytical laminar flow model describes the heat transfer from a heated plate into the cooling fluid when the fluid is flowing between two plain parallel plates. Only one of the plates is being heated to a specified temperature T_w , while the other one is thermally insulated. Heating takes place across the entire plate length with the plate temperature T_w . The cooling fluid enters at a temperature T_{in} and exits at the other end of the plates at a temperature T_{out} . The plates have the length L , a width b and are placed at a distance d from each other. Figure 5.1 displays schematically the setup of the system described by the model.

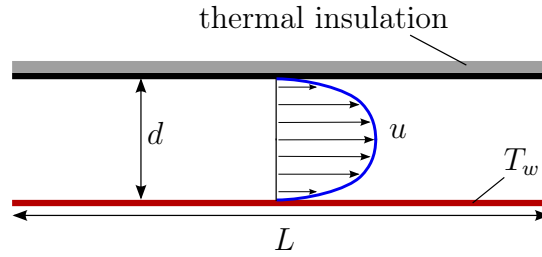


Figure 5.1: Setup of the heat transfer problem described by the analytical model.

The model is based on the following boundary conditions and assumptions:

- The temperature of the heated plate is constant over time and the plate is heated over its entire surface area A ($A = L b$).
- The non-heated plate is thermally insulated. Thus only the heat transfer between the heated plate and the fluid is considered.
- The flow is assumed to be laminar and fully developed.
- The flow is considered to be laminar up to a Reynolds number of 2300.

5.2 Definitions used in the model

Several definitions were used in the analytical model. These definitions are described in this section and will be used in the following sections.

The hydraulic diameter (d_h) for a flow between two parallel plates is twice the plate distance (d) and given to

$$d_h = 2 d. \quad (5.1)$$

The Reynolds number is defined as

$$Re = \frac{\bar{u} d_h}{\nu}. \quad (5.2)$$

where \bar{u} is the mean fluid velocity along the plate length and ν is the kinematic viscosity of the coolant. For the flow between two parallel plates, the flow is considered to be laminar up to a Reynolds number value of $\approx 2200 - 3600$. At Reynolds number values above $3 \cdot 10^4$ the flow is considered fully turbulent. In between these values the flow is in transition between laminar and turbulent flow.

The Nusselt number is defined as

$$Nu = \frac{\alpha d_h}{\kappa}. \quad (5.3)$$

where α is the surface heat transfer coefficient and κ the thermal conductivity of the cooling fluid.

The average surface heat transfer coefficient is given to

$$\dot{q} = \bar{\alpha} LMTD. \quad (5.4)$$

with

$$LMTD = \frac{(T_w - T_{in}) - (T_w - T_{out})}{\ln \frac{T_w - T_{in}}{T_w - T_{out}}} \quad (5.5)$$

with \dot{q} being the heat flux per unit area and $LMTD$ the logarithmic temperature difference.

Due to the temperature dependency of the coolant properties and the temperature difference between inlet and outlet, the material properties should be evaluated for the average fluid temperature (mean temperature (\bar{T})). In the following sections the fluid properties at T_m were used unless stated otherwise.

$$\bar{T} = \frac{T_{in} + T_{out}}{2} \quad (5.6)$$

5.3 Mathematical Modeling

To model the setup described in section 5.1 mathematically, the correlations given in [13] were used. According to these correlations, the average Nusselt number (\overline{Nu}) for the given problem can be calculated to

$$\overline{Nu} = (Nu_1^3 + Nu_2^3)^{1/3} \quad (5.7)$$

with

$$Nu_1 = 4,861 \quad (5.8)$$

and

$$Nu_2 = 1,841 \sqrt[3]{\frac{Re Pr d_h}{L}} \quad (5.9)$$

Nu_1 is the final Nusselt number value when the flow is thermally fully developed. Nu_2 gives the Nusselt number value for regions of thermally developing flow and L is the length over which the plate is heated. In the studied case the plate is heated across the entire length, thus the length of the heated area is equal to the plate length. Due to the temperature dependency of the cooling fluid properties, the direction of the heat transfer (cooling or heating of the plate) has an influence on the heat transfer. In order to take this into account, \overline{Nu} needs to be multiplied by a factor of $(Pr/Pr_w)^{0,11}$ for liquid cooling mediums [11], with Pr and Pr_w being the values of the Prantl number of the coolant at the average fluid temperature, T_m , and the plate temperature, T_w .

Knowing the value of the average Nusselt number (\overline{Nu}), the average surface heat transfer coefficient ($\overline{\alpha}$) can be calculated from equation 5.3 and the amount of heat that is transferred into the coolant per second (\dot{Q}), is then given to

$$\dot{Q} = L b \alpha LMTD \quad (5.10)$$

5.4 MATLAB code

A MATLAB code¹ using the equations from section 5.3 was written in order to facilitate the study of the influence of different design parameters on the heat transfer rate. The program calculates the fluid temperature at the outlet (T_{out}) that results from the parameters set at the beginning of the code. Table 5.1 lists the default initial conditions and parameters, which were used for the calculations in the following sections unless stated otherwise.

Table 5.1: Default initial conditions and parameters used in MATLAB code.

Parameter	value	unit
\bar{u}	0,15	m/s
b	2	m
L	0,5	m
d	2	mm
T_c	90	°C
T_{in}	15	°C
T_{out}	60	°C
T_{diff}	1	°C

The calculation of T_{out} is an iterative process since T_{out} is needed to calculate $LMTD$ and T_m , which are required for the following calculation process and the evaluation of the fluid properties at T_m . In the first iteration a guessed value of T_{out} was used, which was updated at the end of the first iteration step using the following equation:

$$T_{out}^{i+1} = \frac{T_{out}^i + T_{cout}}{2} \quad (5.11)$$

where T_{out}^i is the outlet fluid temperature that was used in the current iteration step and T_{out}^{i+1} the outlet fluid temperature that used in the following iteration step. T_{cout} is the calculated fluid temperature at the outlet, which results from the calculated heat transfer rate (\dot{Q}):

$$T_{cout} = \frac{\dot{Q}}{d b \rho c_p \bar{u}} + T_{in} \quad (5.12)$$

where ρ and c_p are the density and the specific heat capacity of the fluid at T_m ².

¹The MATLAB code which was used was included in the ZIP-file that was submitted with the thesis.

²Instead of using equation 5.11 to update T_{out} for the next iteration step, the outlet temperature calculated in the current iteration step could also have been set as new outlet temperature for the next iteration step ($T_{out}^{i+1} = T_{out}^i$). Equation 5.11 showed, however, to be more efficient, leading to a lower number of required iteration steps to find an accurate solution for T_{out} .

For the evaluation of the fluid properties at the required temperatures, a look-up table was used. The fluid properties in this table were taken from [13].³ At temperature levels between the temperatures that were listed in the look-up table, the values were interpolated linearly, utilizing a linear interpolation function “interp1”.

To determine whether the calculated solution was accurate enough, the difference of the fluid temperature at the outlet between two iteration steps, T_{diff} ,

$$T_{diff} = T_{cout} - T_{out} \quad (5.13)$$

was calculated at the end of each iteration step. If the value of T_{diff} was below the specified termination condition, the iteration process was stopped. $T_{diff} \leq 0,01^\circ\text{C}$ was used as default termination condition.

In order to enable a parameter sweep, a ‘for loop’ was used. The for loop set the value of the swept parameter before the start of each iteration process. Starting with the minimum parameter value, the parameter was increased by a specified ‘step size’ after an iteration process was completed until the maximum parameter value was reached. At the end of the program the calculation results were exported to an Excel file. Figure 5.2 depicts the structure of the MATLAB code in a flowchart.

³The table which was used was included in the ZIP-file that was submitted with the thesis.

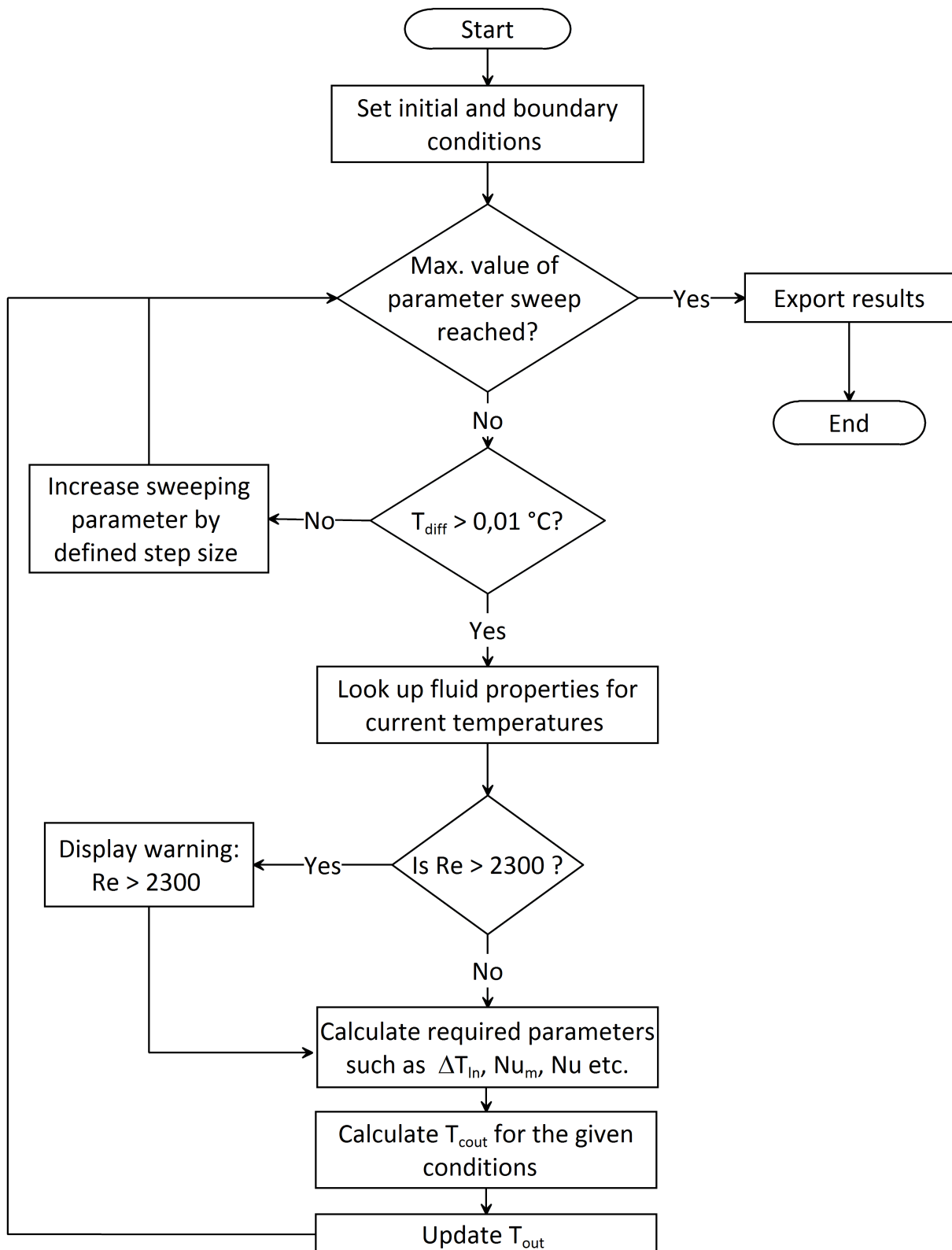


Figure 5.2: Flowchart of the MATLAB code used to study the influence of different parameters on the heat transfer for the analytical laminar flow model with one heated plate.

6 | 2D Heat transfer simulation

A numerical simulation of the heat transfer problem that was modeled analytically in chapter 5 was carried out to compare the simulation results with the analytical ones. This was done to ensure that the simulation delivers accurate results for this simple setup before simulating more complex problems. The simulations were carried out with the simulation software 'COMSOL Multiphysics 4.3a' developed by COMSOL AB using the so-called 'conjugated heat transfer model'.

In the simulation setup, the same boundary conditions as the ones that were used in the analytical model were applied and are listed in table 6.1. A schematic overview of the simulation setup is depicted in Figure 6.1.

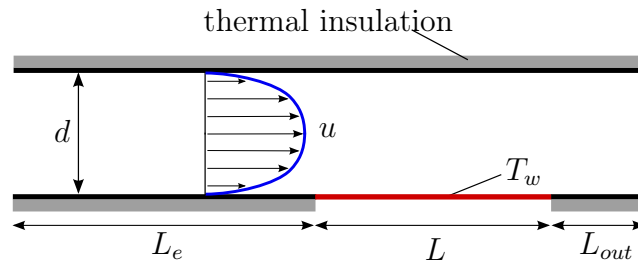


Figure 6.1: Setup of the heat transfer problem described in section 5.1 in COMSOL.

For later comparison with the analytical model, the same velocity sweep, starting from a minimum \bar{u} -value of $0,05 \text{ m/s}$ to a maximum value of $0,5 \text{ m/s}$ with a step size of $0,01 \text{ m/s}$ was simulated. The plate distance as well as the heated plate length were kept constant

Table 6.1: Boundary conditions that were used in the simulation.

Boundary	Boundary condition	
	thermal	fluid flow
Walls	thermal insulation	No-Slip ($u = 0$)
Heated plate surface	$T_w = 90 \text{ }^\circ\text{C}$	No-Slip ($u = 0$)
Inlet	$T_{in} = 15 \text{ }^\circ\text{C}$	\bar{u}
Outlet	Outflow	zero pressure

at $d = 2 \text{ mm}$ and $L = 0,5 \text{ m}$.

To ensure a fully developed flow at the start of the heating plate, the minimum length of the channel was chosen to be twice the estimated entrance length (L_e). The entrance length was approximated to

$$\frac{L_e}{d_h} \approx 0,06 Re \quad (6.1)$$

which is a correlation used for laminar pipe flow [22]. Since only a rough value of L_e was required, equation 6.1 was used, although a laminar channel flow is studied. The maximum entrance length was estimated to $0,5 \text{ m}$, thus the channel length before the heated plate was set to 1 m and was used for the entire velocity sweep.

As solver the standard 'PARDISO-solver' was chosen. A structured, graded mesh with 60 grid points across the plate distance and a grading factor of 3 in this direction was created. This high grid point density was applied in order to ensure that both the hydraulic as well as the thermal boundary layer are solved with a high accuracy. In the flow direction the resolution of the grid was set to 3.4 grid points per mm without any grading. Figure 6.2 shows a sector of the mesh which was used in the simulation.

Grid-independence of the solution was proven by running the same case with a mesh of 80 grid points across the plate distance with a grading factor of 3 and a non graded grid resolution of 4.4 grid points per mm in flow direction. For all \bar{u} -values the obtained change in the calculated water outlet temperature due to the mesh refinement was below 0,1 %. By changing the demanded residual convergence condition from 10^{-3} to 10^{-5} without obtaining a change in the calculated T_{out} -value larger than $0,07 \text{ }^\circ\text{C}$, the solution was shown to be fully converged. The fluid temperature at the outlet was evaluated by calculating the average temperature on the outlet boundary. \dot{Q} was calculated with the help of equation 5.10, where b was set to 2 m , as it was done in the analytical model.

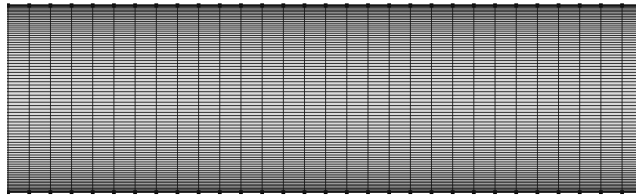


Figure 6.2: Sector of the structured, graded mesh, which was used for the velocity-sweep simulation.

7 | Development of the heat transfer experiment

In this chapter the development of the heat transfer experiment is described. The development of this experimental model and the experimental investigation of the cooling performance of the system was the main content of the thesis.

7.1 Aim of the experiment

The aim of the experiment was to investigate the cooling performance of the cooling system in dependence of various design parameters in an experimental setup, similar to the final motor design.

Of main interest was the evaluation of the influence of the following parameters:

1. coolant mass flow rate and fluid velocity
2. gap width of the flow path
3. current density in the coil

7.2 Layout

In the motor the coolant will flow in the gap between motor and stator and in gaps between the coil windings as illustrated in Figure 4.2 and Figure 4.3. The experimental setup models the flow of water flowing radially outwards between rotor and stator with a variable distance between them.

Due to financial reasons not a complete prototype of the motor was constructed. Instead the experiment was designed to model a sector of the motor as schematically shown in figure 7.1. A sector angle of 40° was chosen as a trade off between costs and comparability between the model and the real motor. A smaller sector might have led to

lower fabrication costs, yet also to a larger share of undesired influences, caused by the triangular shape of the model, which might have distorted the results.

Rotation of the motor will lead to increased fluid velocities, leading to a higher overall heat transfer coefficient and consequently to an improved cooling performance. In the experiment, the stationary state is investigated, since it is assumed that the cooling capacity has the lowest value in this state. Studying the rotational case would have increased the complexity and costs of the experiment significantly.

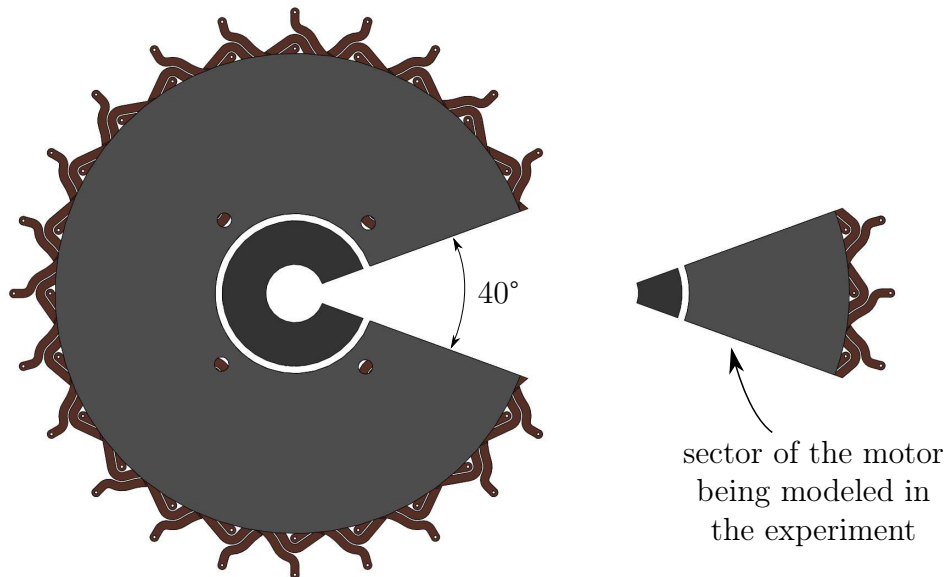


Figure 7.1: In the experiment a sector of the motor is modeled as shown in the figure.

In the experiment a current carrying coil element is used to model the coil of the motor. This coil element was designed to show the same geometric characteristics as the active part of the motor coil. In both the motor coil and the coil element the conductors are directed radially outwards and the width of the conductors increases linearly with the radius. For being able to model the lamination steel between the windings in the motor coil, a small gap was left between the windings in the coil element. These gaps can subsequently be filled with a material with similar thermal properties as lamination steel. Figure 7.2(a) shows the sector of the motor coil which is modeled by the coil element in Figure 7.2(b).

To simulate the flow conditions in the motor, the coil element was embedded into a body made of POM, as shown in Figure 7.3. The body consists of two parts, the lower part in which the coil element is embedded modeling the stator and the upper part modeling the rotor. For being able to investigate the influence of the gap width of the flow path, the distance between the two parts can be varied.

A top-view of the lower part of the experimental model, illustrating the flow path of

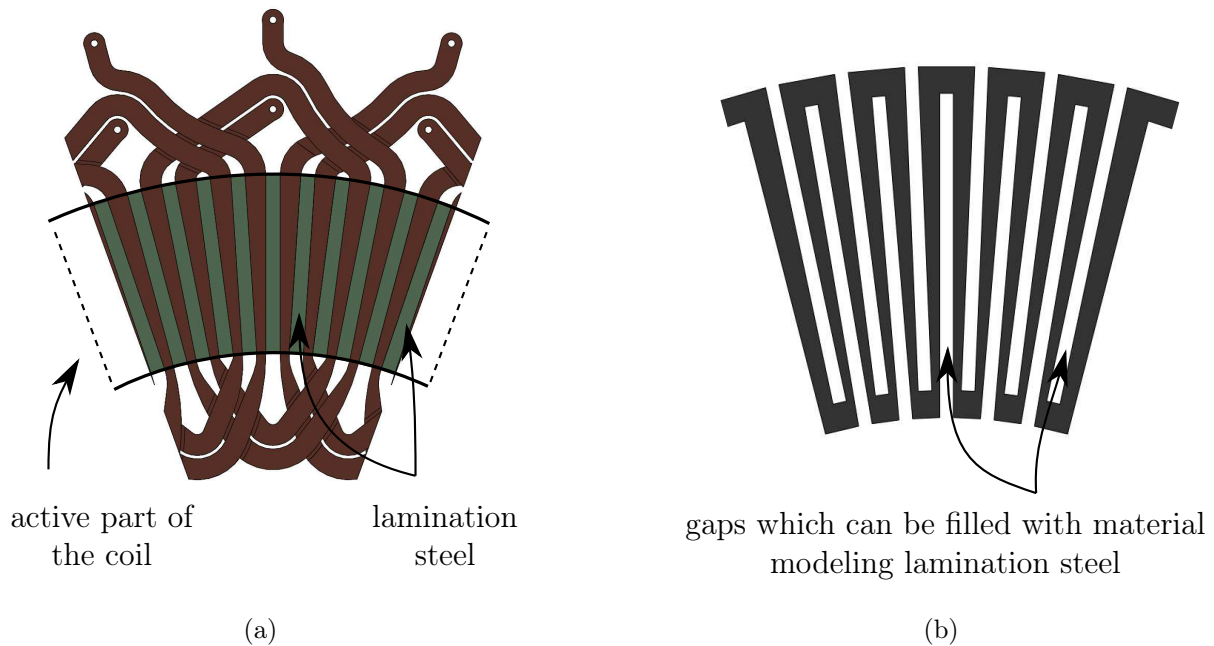


Figure 7.2: Comparison of a sector of the motor coil (a) and the coil element modeling the active part of the sector in the experiment (b).

the water during the experiment is shown in Figure 7.4. Figure 7.5 depicts a sectional view of the model along the symmetry axis, which is marked in Figure 7.4. The water flow path models water entering the motor through the shaft and flowing radially outwards over the stator cooling the coils. In the experiment the coil element is heated by resistive losses. Due to the comparable design of the coil element and the coil in the motor (Figure 7.2), the heat generation is expected to be similar to the one in the motor.

7.3 Measuring method

In this section the measuring method that was used during the experiment is described.

7.3.1 Measurement principle

As it was mentioned earlier, the aim of the experiment was to measure the cooling performance of the system in dependence of various design parameters. Recapitulating equation 7.1 in section 4.1, the following equation has to be satisfied at steady-state conditions:

$$\alpha (T_s - T_\infty) = (T_c - T_s) \frac{\kappa_c}{d_c^2} \quad (7.1)$$

where T_s is the surface temperature of the conductor on the cooled side, T_∞ is the water temperature outside the thermal boundary layer, T_c the conductor temperature on

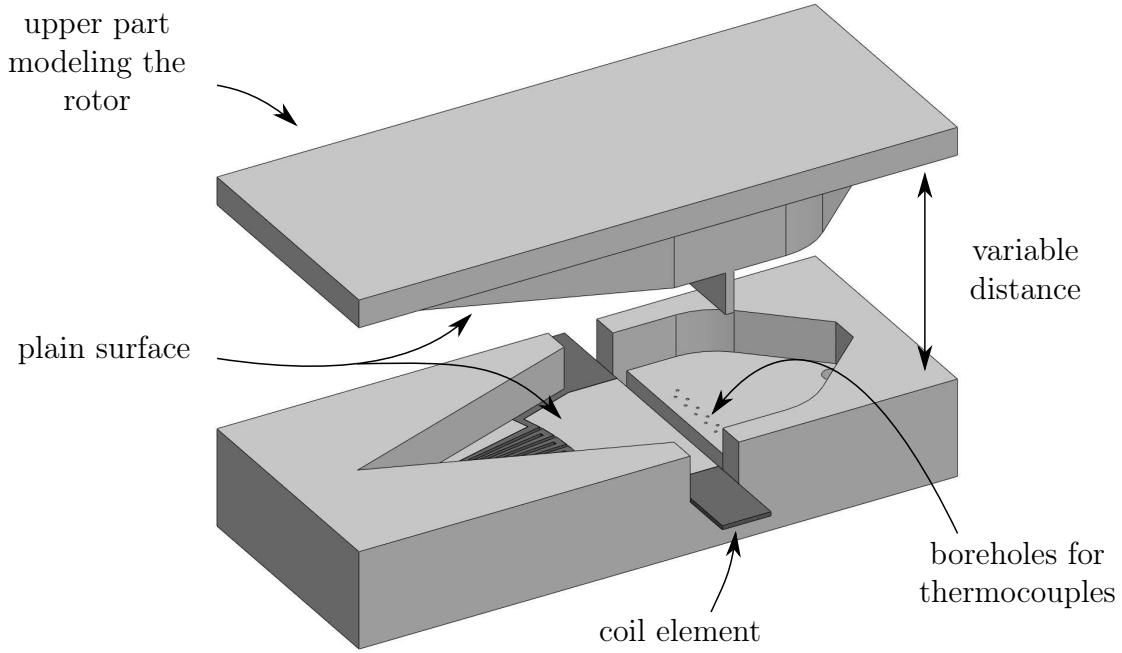


Figure 7.3: Overview of the experimental model consisting of two separate parts. The lower part models the stator while the upper part models the rotor.

the non-cooled side, κ_c the thermal conductivity of the conductor and d_c the conductor thickness.

When all heat is dissipated through the water, this equation can be rewritten to

$$\alpha (T_s - T_\infty) = J^2 A_c R_l \quad (7.2)$$

with J being the current density, A_c the cross section area of the conductor, and R_l the electrical resistance per meter.

When the current density and the fluid temperature outside the thermal boundary layer (T_∞) are held constant while other parameters such as the mass flow rate or the gap width of the flow path are changed, this will lead to a change in the heat transfer coefficient. As a consequence of this the surface temperature of the conductor will increase or decrease until steady-state conditions are reached again.

Based on these considerations, the resulting temperature of the coil element was measured for various parameters. For being able to relate the measured coil element temperature to the flow rate and better comparability of the results, the average heat transfer coefficient was measured indirectly during the experiment, as an indicator of the cooling performance. This was done by measuring the water temperature before and after the coil element as well as the temperature of the coil element. Additionally the current flowing through the coil element and the voltage across it were measured. Assuming that all heat

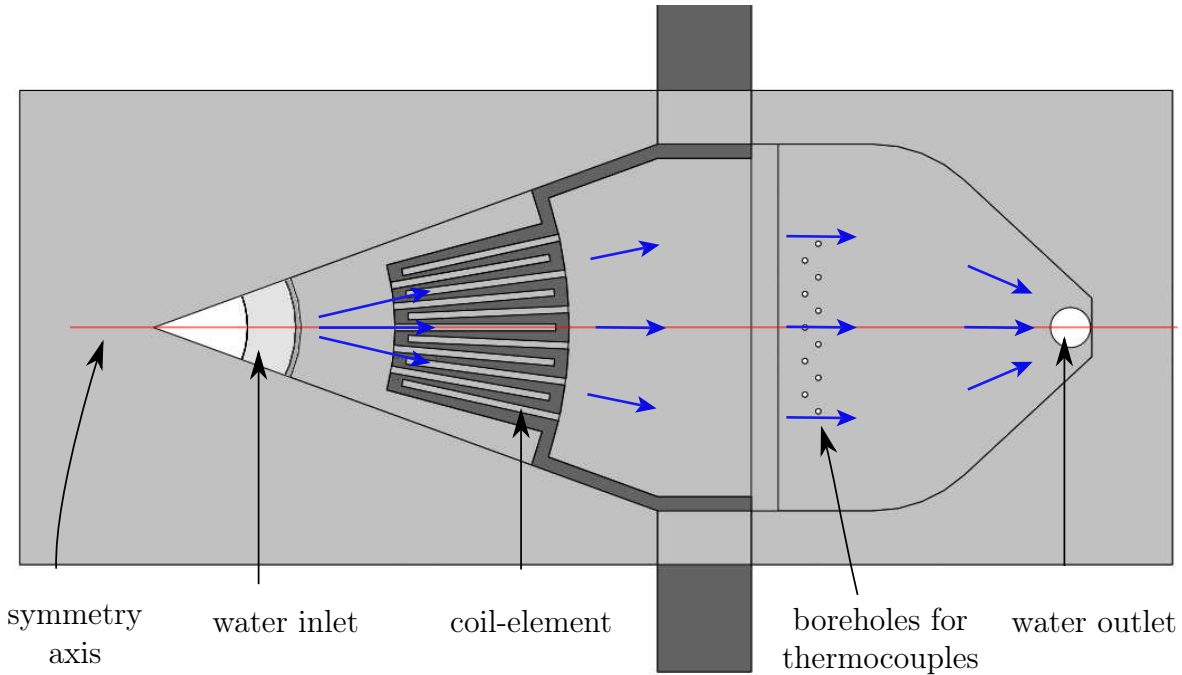


Figure 7.4: Top-view of the lower part of the experimental model. The flow path of the coolant is marked with blue arrows.

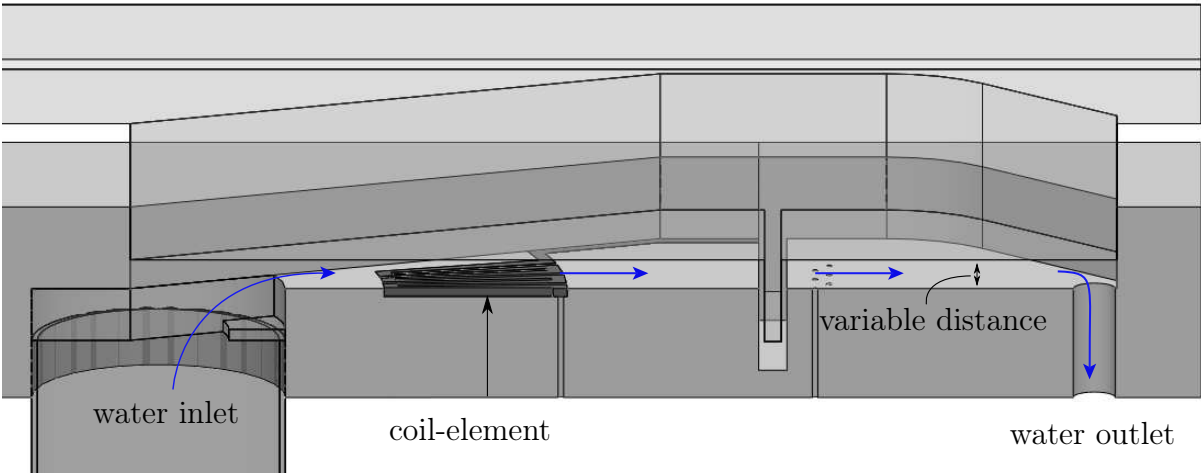


Figure 7.5: Sectional view of the model along the symmetry axis (Figure 7.4)

was dissipated through the cooled surface, the average heat transfer coefficient can be calculated using the following equation:

$$\dot{Q} = V_c I = \bar{\alpha} A_{ht} LMTD = \bar{\alpha} A_{ht} \frac{(T_s - T_{in}) - (T_s - T_m)}{\ln\left(\frac{T_s - T_{in}}{T_s - T_m}\right)} \quad (7.3)$$

where \dot{Q} is the heat transfer rate, V_c the voltage drop across the part of coil element within the area of interest, I the current through the coil element, $\bar{\alpha}$ the average heat transfer coefficient, A_{ht} the heat transfer area, $LMTD$ the logarithmic temperature difference, T_s the average surface temperature inside the area of interest, T_{in} the water temperature at the inlet and T_m the average water temperature behind the heat transfer area.

However, in the experiment some of the heat was not dissipated through the cooled surface, but transferred by conduction to the region outside the area of interest. What proportion of the total heat was transported by this means could however not be measured in the experiment. In order to take these losses into account, the amount of heat transported to regions outside the area of interest by conduction (\dot{Q}_{cond} was measured in the numerical simulations (see chapter 8)). Thus, equation 7.3 was modified resulting in the following equation which was used to calculate the average heat transfer coefficient.

$$\bar{\alpha} = \frac{V_c I - \dot{Q}_{cond}}{A_{ht} LMTD} \quad (7.4)$$

with

$$LMTD = \frac{(T_s - T_{in}) - (T_s - T_m)}{\ln\left(\frac{T_s - T_{in}}{T_s - T_m}\right)} \quad (7.5)$$

How the variables in the equation were measured is described in the following section.

7.3.2 Measurement setup

Due to the triangular shape of the experimental layout, the flow profile and the temperature distribution in the outer regions differ from the one close to the symmetry axis. In order to minimize measurement errors based on these differences an area of interest, in which the measurements were taken, was defined. The area of interest and the positioning of thermocouples and voltmeters is illustrated in Figure 7.6.

As it can be seen from the Figure, the coil element was connected to a current source and the voltage drop across it was measured with a voltmeter. Boreholes with a diameter of 2 mm were drilled for being able to connect a second voltmeter to the non-cooled side of the coil. This was done in order to measure the amount of heat generated in the area of interest.

Through additional boreholes several thermocouples were placed at the back of the coil element. Due to the limited amount of temperatures that could be logged and the symmetry of the layout, all thermocouples were placed on one side of the symmetry axis. Two thermocouples (No. 8 & 9) measured the coil temperature at the start of the coil element, close to the inlet. Three thermocouples (No. 10 – 12) were placed at the hottest spot, with thermocouples No. 10 & 11 measuring the coil temperature inside the area of interest. Thermocouples No. 13 & 14 were measuring the temperature at the end of the coil element during the experiment.

In order to calculate the average heat transfer coefficient, the average water temperature after the heated area had to be measured, which was done with five thermocouples (No. 1 – 5). Measuring the average water temperature right behind the coil element would have led to larger measurement errors, based on the difference in temperature close to the bottom and top part of the model. Therefore an obstacle, which led to a prolonged flow path and thus to a homogenous water temperature (between bottom and top part of the model), was inserted between coil element and measuring point (see Figure 7.5).

The water temperature at the inlet and outlet was measured by thermocouple No. 7 and No. 15. To avoid increased temperatures at the measurement point at the inlet due to insufficient distance from the heated area, thermocouple No. 7 was placed in the inlet pipe (see Figure 7.9). Also thermocouple No. 15 was placed with some distance (approximately 15 cm) from the outlet to assure a homogenous temperature level in the water.

Since the temperature of the coil element on the non-cooled side was measured instead of the average surface temperature of the heat transfer area, the surface of the coil element inside the area of interest (A_{al}) was used as heat transfer area in the calculations. The errors resulting from the approximations that were made are described in the following section.

Based on the measurements the variables in equation 7.3 were calculated as follows:

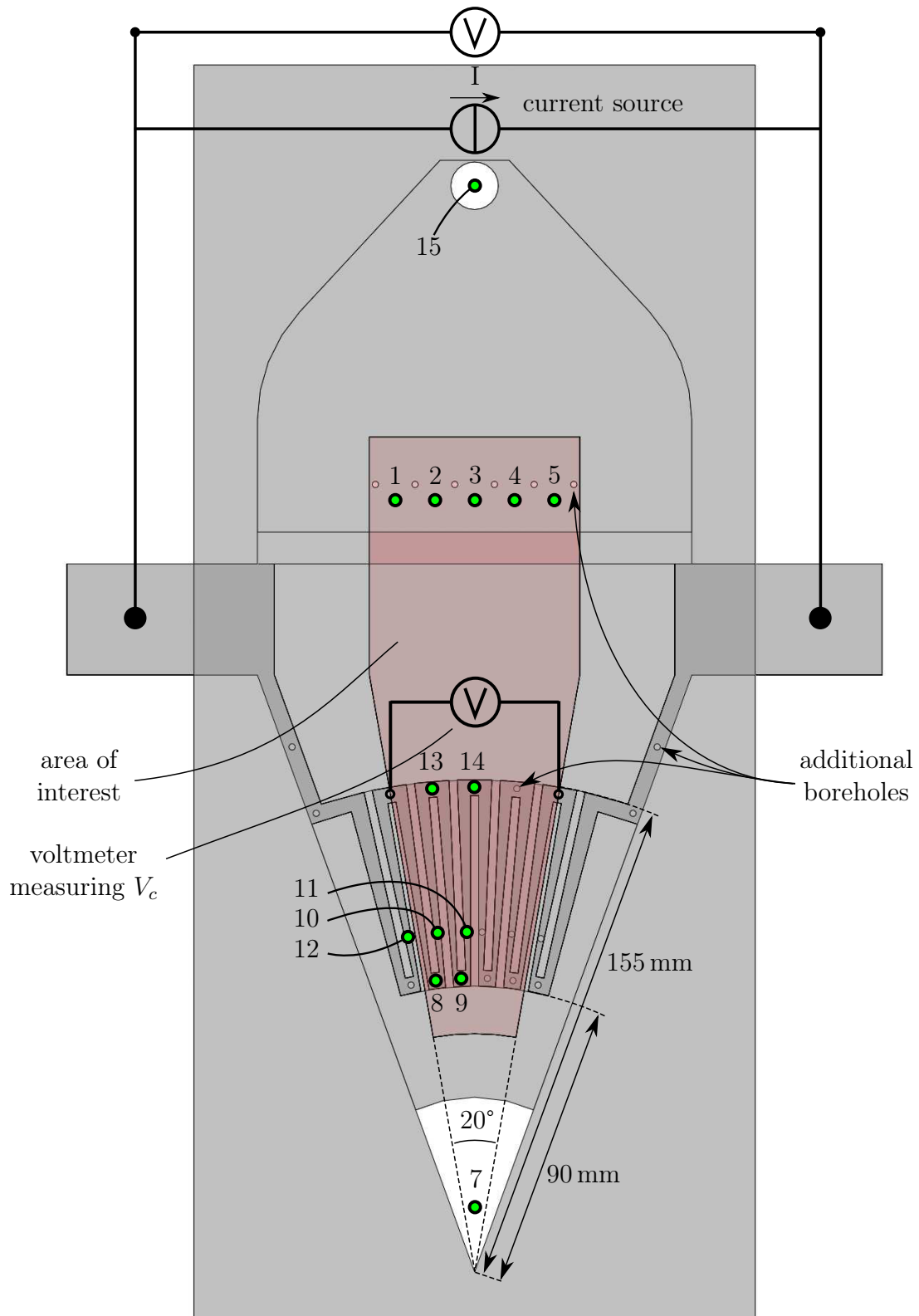


Figure 7.6: Overview of the measurement setup.

$$T_{in} = T_7 \quad (7.6)$$

$$T_m = \frac{T_1 + T_2 + T_3 + T_4 + T_5}{5} \quad (7.7)$$

$$T_c = \frac{T_8 + T_9 + T_{10} + T_{11} + T_{13} + T_{14}}{6} \quad (7.8)$$

$$A_{ht} = A_{al} \approx 15,18 \text{ cm}^2 \quad (7.9)$$

where T_{in} the water temperature at the inlet and $T_{\#}$ the temperature measured by thermocouple No. $\#$ (e.g. T_1 is the temperature measured by thermocouple No. 1).

7.3.3 Calculation errors

Due to the fact that all thermocouples had to be connected through boreholes from the downside, the temperature of the non-cooled side of the coil element was measured. However, the variables A_{ht} and T_s in equation 7.4 and 7.5 relate to the heat transfer area and its average surface temperature. Measuring the average surface temperature of the heat transfer area could however not be done during the experiment which is why some approximations had to be done.

The approximations of the average surface temperature of the coil element on the non-cooled side (T_c) being the surface temperature of the heat transfer area (T_s) and replacing A_{ht} with A_{al} leads to errors when calculating $\bar{\alpha}$ based on these approximations. It is therefore pointed out explicitly, that the calculated average values of heat transfer coefficient ($\bar{\alpha}$) are subject to an error and do not claim to be accurate. The values of $\bar{\alpha}$ were only calculated for being used as an indicator of the cooling performance of the system for various design parameters.

However, the variables which were used to calculate the average heat transfer coefficient were measured with a fairly high accuracy and were used to compare the experimental results with the results from numerical simulations.

7.4 Calibration of thermocouples

The thermocouples that were used in the experiment were calibrated using the calibration device “Amtek RTC-157C“. For doing this, the thermocouples were connected to the thermocouple module which was connected to a computer. The temperatures were set in the calibration device and measured by the thermocouples. During the calibration procedure the temperatures were swept between 0°C and 95°C. The actual calibration was handled by LabVIEW. After the calibration procedure the thermocouples were no longer disconnected from the thermocouple module.

7.5 Flow considerations

A crucial development step of the experimental model was the simulation of the flow through it and was optimized for a uniform flow across the entire coil element surface. A uniform flow distribution was important due to the following reasons:

- The average fluid velocity could not be measured during the experiment. However, without knowledge of the fluid flow for which the measured values were obtained, the results could not have been linked the flow characteristics that were the basis for the obtained results. Therefore, no accurate design parameters could have been derived from the experiment.
- With an unsteady flow, the temperature of the coil element at the measurement points would not have reached a steady state. This would have induced larger measurement inaccuracies.
- The comparison of the obtained results would have been difficult as the flow might have changed with changing the mass flow rate or the gap width.

A large number of simulations were carried out to find a solution to this problem. Therefore, only the most important outcome of these simulations are presented in this section.

7.5.1 Jet effect - horizontal water inlet

Simulations of the flow through the heat test showed an increased velocity in the central area of the coil element and significantly lower velocities at the areas close to the walls. Several changes in the geometry such as smoothing of the edges in the geometry, changing the diameter of the inlet, studying the influence of the inlet length and other parameters

were done, however without solving the problem. A literature review of [22] revealed that this problem was based on the opening angle of the geometry and that the jet effect could not have been avoided without decreasing the covered section. Due to this, the inlet was changed to a be vertical instead of horizontal. Through this angle of 90° the heat test also comes closer to the flow in the actual motor.

7.5.2 Turbulences at the inlet-angle

After the inlet was changed to a vertical one, turbulences that occurred at the 90° -angle, led to a non-uniform velocity distribution across the surface. Again several changes in the geometry were made, trying to get rid of this non-uniformity of the velocity distribution. Prolonging the inlet length, as illustrated in Figure 7.7, showed large improvements of the uniformity of the flow across the coil element. Figure 7.7 illustrates the setup used in the simulation.

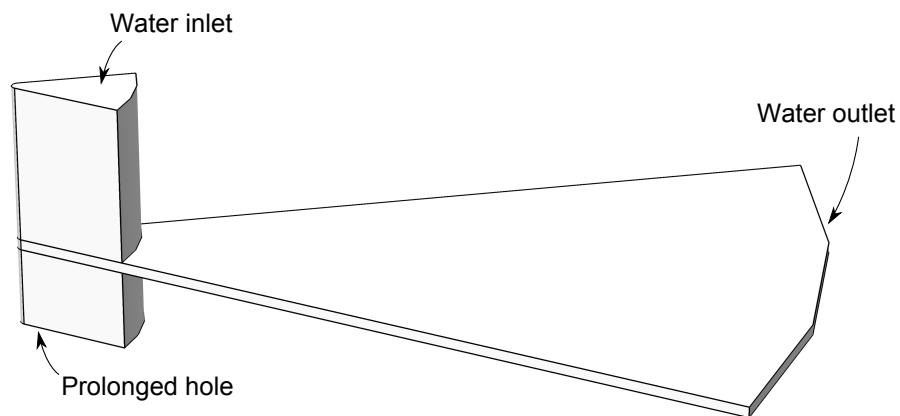


Figure 7.7: Geometry which was used in the simulation setup, representing the area in which water will be able to flow. A prolonged inlet, showed to be an effective tool to reduce the turbulences, which led to a non-uniformity in the velocity profile.

Further simulations showed that the fluid velocity in vertical direction was a parameter of great importance. Larger velocities in this direction led to a larger non-uniformity of the flow across the coil element. For this reason the size of the inlet was increased. Additionally a ring was inserted into the inlet pipe in order to force the fluid to start changing the flow direction into the horizontal direction before hitting against the end wall. The final layout of the inlet can be seen in Figure 7.5.

For an easier handling of the heat test in the laboratory, it was decided to add a water outlet, collecting the water. This outlet however, induced an increase in pressure close to the outlet, which influenced the pressure distribution over the surface. This was solved by prolonging the distance between water outlet and the area at which the coil element was placed. Due to the low pressure losses that were obtained from the simulation, the pressure losses were not measured during the experiment.

7.6 Materials

For the choice of materials used in the model, four criteria were of particular importance:

1. Material properties
2. Knowledge of the thermal properties
3. Processability
4. Price

To estimate the cooling performance of the real motor, the materials modeling the coil and the lamination steel had to have similar material characteristics as the materials which will be used in the motor. Precise knowledge of the thermal properties of all materials was the basis for the quality of the measurement results – more precise knowledge of the material properties leads to better comparability of the results with results from numerical simulations and a more accurate estimation of the cooling performance that can be expected. To minimize measurement errors and for being able to compare the experimental results with numerical simulations in an accurate way, the model had to be manufactured with high precision.

7.6.1 Material selection

In consideration of the criteria mentioned above the following materials were selected:

POM (polyoxymethylene, DIN EN ISO 1043) was used for the main body. The main reason for this was the low thermal conductivity of POM of $0,31 \text{ W/mK}$. A perfect insulating material would have been desirable in order to prevent any heat transport through the material. The aim of the experiment was to measure the average heat transfer coefficient on the surface of the active part of the coil. Thus, any heat transported through the surrounding material is a source of error. Besides the low thermal conductivity POM offers a good processability, a very high electrical volume resistivity ($10^{13} \text{ } \Omega/\text{cm}$) and a sufficiently high melting point ($165 \text{ }^\circ\text{C}$) at a moderate price. The material properties were taken from the data sheet provided by the manufacturer [19].

The coil element was made of aluminum (Al 5052 alloy) as aluminum will most likely be used as coil material in the final motor. This aluminum alloy is usually not used in electrical devices and has a lower electrical and thermal conductivity of 35 % $IACS \approx 20,3 \cdot 10^6 \text{ S/m}$ and 138 W/mK than pure aluminum [1].

For the experiment this was, however, no drawback since the main focus was to measure the average heat transfer coefficient on the coil surface and the thermal conductivity of the material did not limit the measurement results. Moreover the experiment was designed to estimate the lower limit of the cooling capacity, which can be expected for the real motor. A higher electrical conductivity of the coil material used in the final motor will lead to lower resistive losses and consequently to lower temperatures than in the experimental model.

As already mentioned earlier, the use of aluminum seems promising due to the alumina layer, which acts as an insulating layer. In case this alumina layer isolates the coil sufficiently from the coolant no additional isolation layer would be necessary. This would not only improve the cooling performance of the machine but would also be a very cost effective solution. It was, however, not known whether this alumina layer would be sufficient as isolation layer and was therefore tested in the experiment.

For the choice of the material modeling the lamination steel several materials were considered. As the thermal conductivity of the lamination steel used in the final motor was not known yet but is expected to be relatively low, it was decided to fill the gaps of the coil element with a material with a very low thermal conductivity. Besides a low thermal conductivity the material had to be able to withstand temperatures of at least 100°C . After filling the gaps, the surface should furthermore be as smooth as possible in order to estimate the lower limit of the cooling performance of the system. Gypsum and silicone were considered possible choices based on their low thermal conductivity and accessibility. Due to the good adhesion of silicone on aluminum and its flexibility, silicone was the final choice. Adhesion and flexibility were important selection criteria since the coil element had to be removed and reinserted repeatedly during the installation process and gypsum might have broken during this procedure. Table 7.1 lists the materials that were considered possible choices with their thermal conductivity and maximum operating temperatures.

Both silicones from Bossert (Silcoset 151 and AS1745G) offer a low thermal conductivity and a high maximum operating temperature. These products were however not available in Norway and their shipping from abroad would have taken several weeks. Due to time constraints it was decided to use a silicone, which is sold in Norway. However, the thermal conductivity of these sealing materials (Glass Silikon 3985 and Fire Acrylic 6801) were not provided by the manufacturer and had therefore to be measured, as de-

 Table 7.1: Selection list of materials considered to model lamination steel.

Name	manufacturer	κ in W/mK	c_p in MJ/kgK	T_{max} in °C
Silcoset 151	Bossert	0,20 [9]	-	300 [9]
AS1745G	Bossert	0,20 [8]	-	316 [8]
Glass Silikon 3985	Casco	0,173	1,048	180 [3]
Fire Acrylic 6801	Casco	0,479	2,05	very high

scribed in the following section. Based on its low thermal conductivity and sufficiently high maximum operating temperature “Glass Silikon 3985” was used as lamination steel modeling material.

7.6.2 Material properties

Most of the material properties that were of interest for the experiment were provided by the manufacturers. The thermal conductivity and heat capacity of the selected silicone and the temperature coefficient of resistance (γ) of aluminum (Al 5052 alloy) were however unknown and were measured for this reason. The measurement procedure of these properties is described in the following paragraphs.

The thermal conductivity and heat capacity of “Glass Silikon 3985” and “Fire Acrylic 6801” from Casco were measured with the help of the instrument Hot Disk TPS 2500S¹. For this purpose two measurement samples of 5 cm × 5 cm × 1 cm for each of the sealing materials were required. In order to get accurate measurement results, the samples had to be fully dry, which took about 10 days because of the thickness of the samples. The measurement results are listed in Table 7.1. heat capacity of “Glass Silikon 3985” and “Fire Acrylic 6801” were measured to 1,048 MJ/kgK and 2,05 MJ/kgK, respectively.

In order to measure the temperature dependence of the resistance of the coil element, the resistance across the element was measured at various temperatures between room temperature (27 °C) and 95 °C. The resistance at temperature above room temperatures were measured by heating the coil element in an oven. In the oven the coil element was placed on a 3 °C thick wooden plate and the thermocouple was placed between coil element and wooden plate. The resistance was measured after the temperature had stabilized. For the resistance measurement the ohmmeter “GW instek GOM-802” offering a resolution of 1 mΩ was used. The measurement results are displayed in Figure 7.8. By linear regression the temperature coefficient of resistance was calculated to $\gamma \approx 2,11 \cdot 10^{-3}$. Table 7.2 gives an overview of the properties of the materials that were used in the experimental model.

¹These measurements were carried out by Ignat Tolstorebrov and Christian Schlemminger

Table 7.2: Properties of the materials used in the experimental model. The listed values were measured or taken from [19, 1, 3].

Material	ρ in g/cm^3	κ in W/mK	c_p in J/kgK	σ in S/m
Al 5052 alloy	2,68	138	880	$20,3 \cdot 10^6$
Glass Silikon 3985	1,02	0,173	1027,5	-
POM	1,41	0,31	1500	10^{-13}

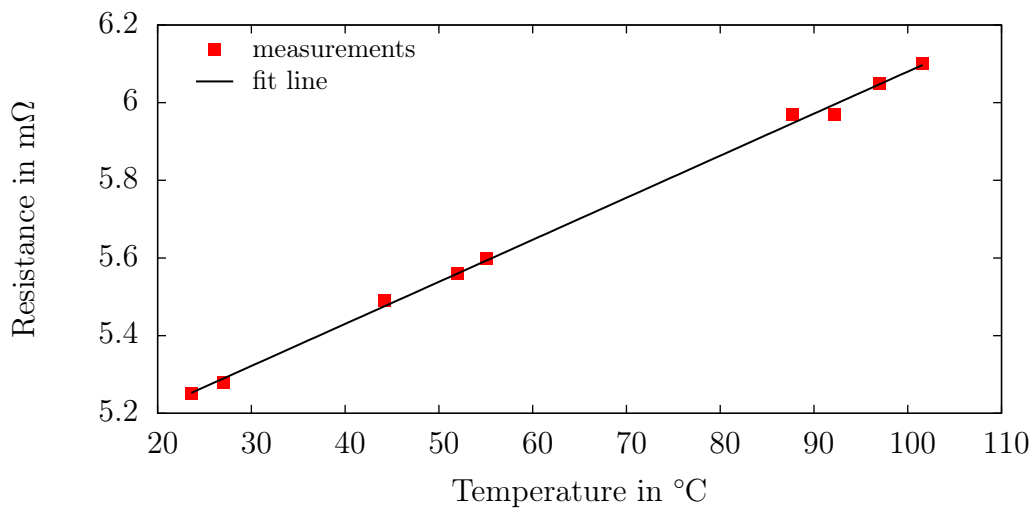


Figure 7.8: Measured resistance of the coil element in dependence of temperature.

7.7 Fabrication

The baseline for the comparison of the experimental and simulation results was that the same cases were studied. Therefore, an accurate fabrication of the experimental geometry was of great importance and was fabricated using a CNC-drilling machine. The geometry was manufactured by Øystein Gjervan Hagemo and will therefore not be described in more detail.

7.8 Experimental procedure

7.8.1 Setup

An overview of the experimental setup is given in Figure 7.9. As it can be seen from the figure, a pump was used to pump the water from a larger container into the heat transfer geometry with a continuous mass flow rate. The water entered the geometry through a pipe at the inlet. After passing through the geometry the water flowed through a hose, connected to the outlet of the geometry, into a bucket. In order to measure the mass flow rate, the bucket was placed on a scale which was logging its weight. The coil element was connected to a power supply, with which the amount of current could be varied. During the experiment the current through the coil element and the voltage drop across it were measured. Additionally the voltage drop across the area of interest (see Figure 7.6) was logged. The water temperature was measured by a total of 14 thermocouples, where seven of them were measuring the water temperature and the other seven the temperature of the coil element. The position of these thermocouples and the voltmeters is explained in detail in section 7.3.2 and illustrated in Figure 7.6. A data logger which was connected to a computer was used to log the data from the thermocouples, the scale and the voltage drop across the inner part of the coil element. LabVIEW developed by National Instruments was used as data acquisition software.

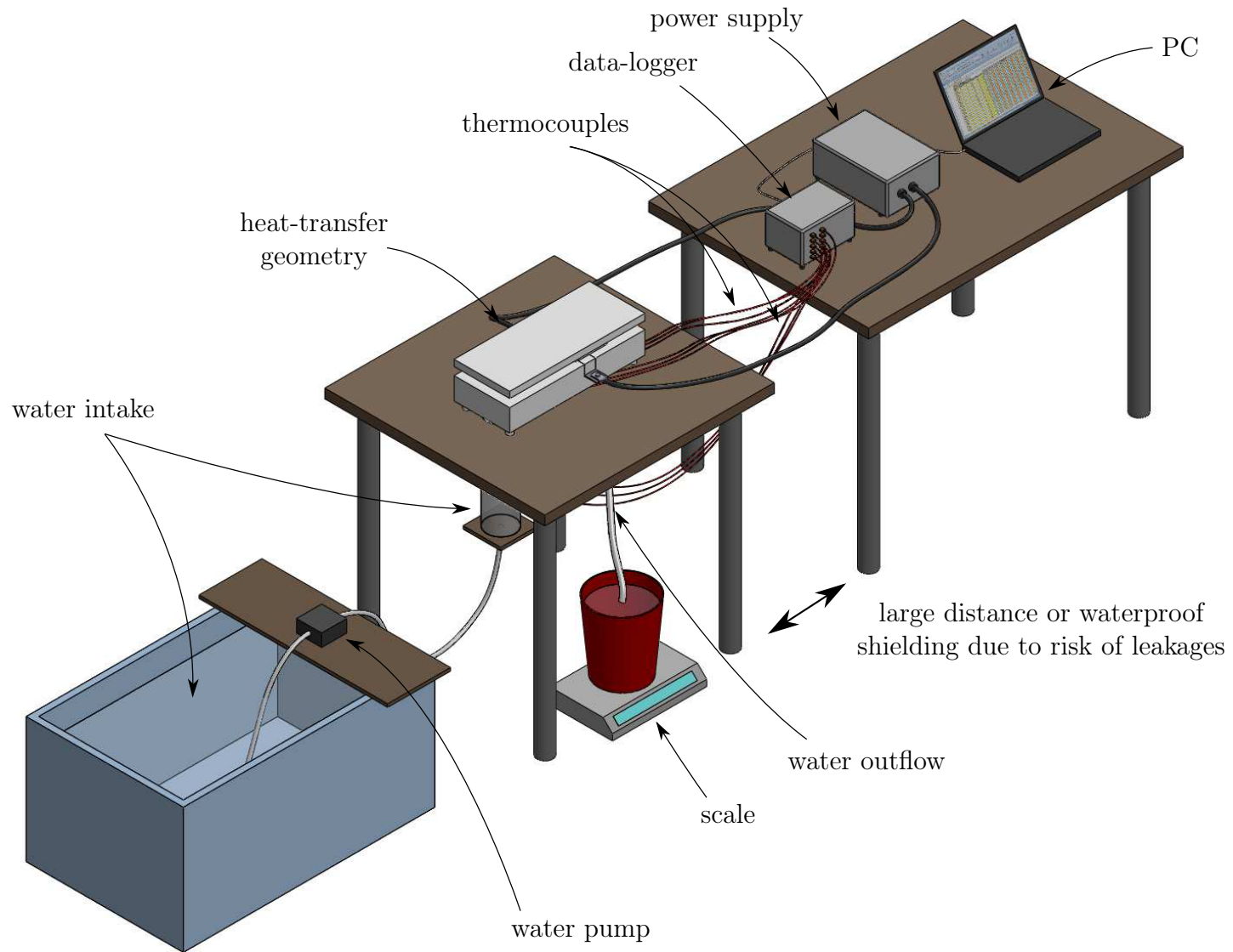


Figure 7.9: Overview of the experimental setup in the lab.

7.8.2 Procedure and data acquisition

As first step of each measurement, the water mass flow rate and the amperage through the coil element were set to the desired level. The flow rate, water temperature and the temperature of the coil element were then monitored using LabVIEW, while the amperage was monitored manually with a clamp meter.

When the temperatures had reached a steady state, measurements were taken.² The data from the scale, the thermocouples and the voltage drop across the inner part of the coil were logged once every second over a period of 200s using LabVIEW. At the end of each measurement, the voltage drop across the coil element and the amperage were measured manually.

7.9 Estimation of the measurement accuracy

7.9.1 Measurement uncertainties

Temperature

Thermocouples of type T were used for the temperature measurements since they offer a better accuracy in the temperature range of the experiment than type K thermocouples. In order to determine the systematic error after the calibration procedure described in section 7.4, the temperature of the calibration instrument (Amtek RTC-157C) was varied between 0 °C and 100 °C. The maximum deviation between the temperature measured with the thermocouples and the temperature that was set was $\pm 0,1$ °C. This value was used as systematic uncertainty for the temperature measurements.

$$\Delta T_{sys} = 0,1 \text{ } ^\circ\text{C} \quad (7.10)$$

The mean value and standard deviation of each measurement series was calculated with equation 7.11 and equation 7.12, respectively.

$$\bar{T} = \frac{1}{n} \sum_{i=1}^n T_i \quad (7.11)$$

$$S = \sqrt{\frac{1}{n-1} \sum_{i=1}^n (T_i - \bar{T})^2} \quad (7.12)$$

To calculate the statistical uncertainty of a measurement series the so called Student's

²Depending on the final temperature level this it could take up to until steady-state conditions were reached.

t-distribution was used. With a confidence level of 99,7 % the correction factor is $t = 3,04$ and the statistical uncertainty (Δx_{stat}) given to

$$T_{stat} = t \frac{S}{\sqrt{n}} = 3,04 \frac{S}{\sqrt{n}} \quad (7.13)$$

Considering that it is not unlikely that the systematic and statistical uncertainties occur simultaneously and deviate the mean value in the same direction, the absolute values of the systematic and statistical uncertainties were added yielding a total uncertainty of

$$\Delta T = T_{sys} + T_{stat} \quad (7.14)$$

for each temperature measurement series.

Current

The current through the coil was measured with a clamp meter (Fluke 336). At a frequency of 50 Hz the clamp meter measures the amperage with an accuracy of $\pm (2 \% + 5 \text{ counts})$. With a resolution of 0,1 A the amperage was thus measured with an uncertainty of

$$\Delta I = 2 \% + 0,5 \text{ A}. \quad (7.15)$$

Voltage

The voltage drop across the coil element (V) was measured with a multimeter (Fluke 77) with an accuracy of $(\pm 2\% + 2 \text{ counts})$ in a range of up to 6 V. Since the measurements were taken manually, the positions on the coil element where the measurements were taken were marked in order to avoid systematic inaccuracies. With a readability of 1 mV the measurement uncertainty for the voltage drop was estimated to

$$\Delta V = 2 \% + 2 \text{ mV} \quad (7.16)$$

The voltage drop across the coil element inside the area of interest (V_c) was measured by an analog input module (NI 9223) using LabView. This module measures the voltage with an accuracy of $\pm 0,3 \%$. As the connecting cables were fixed to the coil element and with a fairly high precision due to the boreholes drilled with a CNC drilling machine, the systematic error was estimated to $\pm 0,5 \%$, leading to a total measurement uncertainty of

$$\Delta V_c = 0,3 \% + 0,5 \% = 0,8 \% \quad (7.17)$$

Mass flow rate

All water flowing out of the experimental geometry, was collected in a bucket which was placed on a scale (Mettler toledo SB32000). The mass flow rate was measured by measuring the change of weight of the bucket with time. Since the experimental geometry and all hoses connected to it were absolutely water proof, the flow rate through the experimental geometry was equal to the flow rate flowing into the bucket. The water pump generated a stable flow rate and the measured values and time were logged each second over a period of 200s with LabView. Therefore, only inaccuracies of the weight measurement were considered to have led to uncertainties. A slight measurement uncertainty might have been created by the fact that the water was dripping into the bucket which was estimated to ± 3 g. With a readability of 1g and a linearity of 0,5g the uncertainty of the mass flow rate measurement was summed up to:

$$\Delta \dot{m} = \frac{1 \text{ g} + 3 \text{ g}}{200 \text{ s}} = \frac{4 \text{ g}}{200 \text{ s}} = 1,2 \text{ g}/\text{min} \quad (7.18)$$

7.9.2 Heat transferred to surrounding

Due to natural convection, heat was transferred from the outer surfaces of the experimental setup to the surrounding air. At steady-state conditions, this heat transfer problem can be expressed by

$$\kappa A \frac{T_i - T_s}{d} = \alpha A (T_s - T_r) \quad (7.19)$$

From the measurement results T_i and T_r can be approximated. To estimate the amount of heat that was transferred, the surface temperature (T_s) and the heat transfer coefficient α had to be calculated. In order to calculate α , correlations which were taken from [18] were used. According to these correlations the Nusselt number for isothermal surfaces can be calculated by the following equation

$$Nu = C (Gr Pr_{air})^m = \frac{\alpha l}{\kappa_{air}} \quad (7.20)$$

where C and the exponent m are geometry dependent constants given in Table 7.3. The Prandtl number is a temperature dependent fluid property which can either be looked up in tables or calculated with equation 3.6. The Grashof number is defined to

$$Gr = \frac{g \beta (T_s - T_r) l^3}{\nu_{air}^2} \quad (7.21)$$

where β is the thermal expansion coefficient of air and l the characteristic length. For the value of β the approximation for ideal gases ($\beta = 1/T_{abs}$) was used. The material

properties were looked up for the so called film temperature T_f :

$$T_f = \frac{T_s + T_r}{2} \quad (7.22)$$

Due to the temperature dependent variables in equation 7.21, the calculation of α is an iterative process and was therefore only done once for the following cases.

Table 7.3: Constants for different geometries used in equation 7.20

Geometry	$Gr Pr$	C	m
vertical plate	$10^4 - 10^9$	0,59	0,25
Upper surface of a heated plate	$2 \cdot 10^4 - 8 \cdot 10^6$	0,54	0,25
Lower surface of a heated plate	$10^4 - 10^{11}$	0,27	0,25

Heat losses through the sides:

For the calculation of the heat transfer coefficient on the sides of the geometry the variables of equation 7.19 and 7.20 were approximated to:

- $d = 5 \text{ cm}$ as average distance from the flow path to the outer geometry surface
- $T_i = 30 \text{ }^\circ\text{C}$ higher average temperatures were not expected since the highest water temperature at the outlet obtained during the experiment was $\approx 30 \text{ }^\circ\text{C}$
- $T_r = 22 \text{ }^\circ\text{C}$ estimated temperature in the lab
- $A = 850 \text{ cm}^2$ which is the area of the sides of the lower part of the geometry
- $l = 7 \text{ cm}$ which is the height of the lower geometry part

With these values and the constants for the case of a vertical plate in Table 7.3, the heat transfer coefficient was calculated to $\alpha_{side} = 3,7 \text{ W/m}^2 \text{ K}$. For the estimation of the heat losses on the side, the surface temperature was calculated with equation 7.19. However, T_i was set to the measured water temperature at the outlet ($T_i = T_{out}$), instead of $30 \text{ }^\circ\text{C}$. Consequently, the heat flow through the sides of the geometry was estimated to:

$$\dot{Q}_{side} = \kappa_{POM} A_{side} \frac{T_{out} - T_s}{d_{side}} \quad (7.23)$$

with $d_{side} = 5 \text{ cm}$ and $A_{side} = 850 \text{ cm}^2$.

Heat losses through the top:

For the calculation of the heat transfer coefficient on top of the geometry the variables of equation 7.19 and 7.20 were approximated to:

- $d = 7 \text{ cm}$ which is the height of the upper geometry part

$T_i = 27^\circ\text{C}$ approximated average water temperature between the inlet and outlet
 $T_r = 22^\circ\text{C}$ estimated temperature in the lab
 $A = 760\text{ cm}^2$ which is the area of the top of the of the geometry
 $l = A/p$ with p being the perimeter of the plate which was estimated to 1,2 m

With these values and the constants for the case of the upper surface of a heated plate in Table 7.3, the heat transfer coefficient was calculated to $\alpha_{top} = 3,1\text{ W/m}^2\text{K}$. For the estimation of the heat losses on the top, the surface temperature was calculated with equation 7.19. However, T_i was set to mean value of the water temperature at the inlet and outlet ($T_i = (T_{in} + T_{out})/2$), instead of 27°C . Consequently, the heat flow through the top surface of the geometry was estimated to:

$$\dot{Q}_{top} = \kappa_{POM} A_{top} \frac{T_{in} + T_{out}}{2} - T_s \quad (7.24)$$

with $d_{side} = 7\text{ cm}$ and $A_{side} = 760\text{ cm}^2$.

Heat losses through the bottom

The heat losses through the bottom of the geometry were expected to have the greatest impact on the measurement results since the coil element was embedded into the lower part of the experimental model parallel to its underside. In order to limit the heat losses, a 5 cm thick plate of expanded polystyrene was placed between the geometry and table. Due to the large surface of the table on which the whole experimental setup was placed, it was assumed that the surface temperature of the table was equal to the temperature in the lab (T_r). the thermal model which was used to estimate the heat losses through the underside of the geometry can be written to:

$$\dot{Q}_b = A_b U (T_i - T_r) \quad (7.25)$$

$$U = \left(\frac{1}{U_{POM}} + \frac{1}{U_{poly}} \right)^{-1} = \left(\frac{d1}{k1} + \frac{d2}{k2} \right)^{-1} \quad (7.26)$$

The average temperature inside the geometry (T_i) was approximated from the measurement results of the average water temperature at the inlet and outlet and the average temperature of the coil element:

$$T_i = \frac{T_{in} + T_c + T_{out}}{3} \quad (7.27)$$

This approximation seemed reasonable as the whole area of the water flow path³ was

³The flow path area was set equal to the area of the underside of the upper part of the experimental

considered as heat transfer area ($A_b \approx 314 \text{ cm}^2$) of which a share of approximately 20 % was heated by the coil element while the rest was cooled by water flowing across it.

Heat losses coil element

As it can be seen from the Figures showing the experimental model, parts of the coil element were standing out of the geometry which was necessary in order to contact the cables of the power supply to it. To limit heat losses, these areas were insulated with a layer of 5 cm of expanded polystyrene on all sides. Due to the very low thermal conductivity of expanded polystyrene and the fact that the temperature difference between these parts of the coil element and the air temperature in the lab did not exceed 6 °C, the heat losses were very small and were therefore neglected.

7.9.3 Propagation of uncertainty

As described in section 7.3.1, the average heat transfer coefficient was measured indirectly and calculated using the following equation.

$$\bar{\alpha} = \frac{V_c I - \dot{Q}_{cond}}{A_{ht} LMTD} \quad (7.28)$$

with

$$LMTD = \frac{(T_c - T_{in}) - (T_c - T_m)}{\ln\left(\frac{T_c - T_{in}}{T_c - T_m}\right)} \quad (7.29)$$

$$LMTD = \frac{T_m - T_{in}}{\ln\left(\frac{T_c - T_{in}}{T_c - T_m}\right)} \quad (7.30)$$

To estimate the uncertainty of the logarithmic temperature difference the variance formula was applied as it seemed rather unlikely that all uncertainties occur simultaneously with all of them deviating in positive or negative direction from the mean temperature value. The uncertainty of the logarithmic mean temperature difference was calculated to

$$\Delta LMTD = \sqrt{\Delta T_m^2 \left[\frac{\delta LMTD}{\delta T_m} \right]^2 + \Delta T_c^2 \left[\frac{\delta LMTD}{\delta T_c} \right]^2 + \Delta T_{in}^2 \left[\frac{\delta LMTD}{\delta T_{in}} \right]^2} \quad (7.31)$$

in which the partial derivatives in equation 7.32 were calculated for the mean values $(\overline{T_m}, \overline{T_c}, \overline{T_{in}})$.

As it was mentioned in section 7.3.1, the average coil element temperature (T_c) and the average fluid temperature after the heat transfer area (T_m) were calculated with equation (see Figure 7.3).

tion 7.8 & 7.7. Therefore, the influence of the uncertainties of the individual temperature measurements ($T_1 - T_5$ and $T_8 - T_{11}, T_{13}, T_{14}$) on T_c and T_m were calculated in the same manner as $\Delta LMTD$ and the uncertainty of each measurement series was calculated according to equation 7.10, 7.13 & 7.14.

The resulting uncertainty of the heat transfer coefficient was calculated using the variance formula as the measurements were taken independently from each other. This resulted in an uncertainty of

$$\left| \frac{\Delta\alpha}{\bar{\alpha}} \right| = \sqrt{\left| \frac{\Delta V_c}{\bar{V}_c} \right|^2 + \left| \frac{\Delta I}{\bar{I}} \right|^2 + \left| \frac{\Delta LMTD}{\bar{LMTD}} \right|^2} \quad (7.32)$$

As the heat losses to the surrounding lowered the amount of heat that was transferred to the water, they were subtracted from the total amount of heat \dot{Q} . Since the losses did not only occur inside the area of interest but also outside of it, the losses were multiplied with the ratio between the voltage drop inside the area of interest and total voltage drop.

$$\Delta\dot{Q} = \dot{Q} - \frac{V_c}{V} (\dot{Q}_{side} + \dot{Q}_{top} + \dot{Q}_b) \quad (7.33)$$

These losses occurred simultaneously and their influence on the average heat transfer coefficient was therefore not calculated with the variance formula but subtracted from \dot{Q} to estimate the lower limit of the average heat transfer coefficient.

8 | Numerical simulation of the experimental setup

In order to be able to compare the measurement results from the experiment with the ones obtained from numerical simulations, a model of the experimental setup was created in “COMSOL Multiphysics 4.3a”. How this model was implemented is the content of this chapter. The presented model was included in the ZIP-file that was submitted with the thesis.

8.1 Setup

The aim of the numerical simulations was to simulate the cases that were carried out in the experiment in order to compare the results with each other. For this reason the experimental model was built up as closely as possible to the experimental setup. The geometry which was used in the simulation was created in “SolidWorks 2012” and subsequently imported into “COMSOL Multiphysics 4.3a”.

For the setup of the simulation, the symmetry of the experimental layout was utilized as illustrated in Figure 8.1. Through this the size of the geometry was cut in half which reduced the number of mesh-elements by 50 % and consequently also the computational time without reducing the quality of the calculated results¹. To further decrease the size of the geometry and thus the number of mesh-elements not the whole POM-body was included in the simulation setup but only the part surrounding the coil element. This part, however, had to be included in the model due to the relatively high temperature gradients in this region. As a consequence of the temperature gradients conductive heat transfer takes place in this part of the POM-body which influence the coil element temperature.

As it can be seen from Figure 8.1 a part of the pipe at the inlet (see Figure 7.9) was incorporated in the layout. This was done to create the same flow conditions at the inlet

¹In order to ensure that the use of symmetry planes did not influence the results, two simulations were carried out with one using the full size of the geometry while the other one utilized symmetry planes. Subsequently the results were compared and did not show any deviations.

as in the experiment.

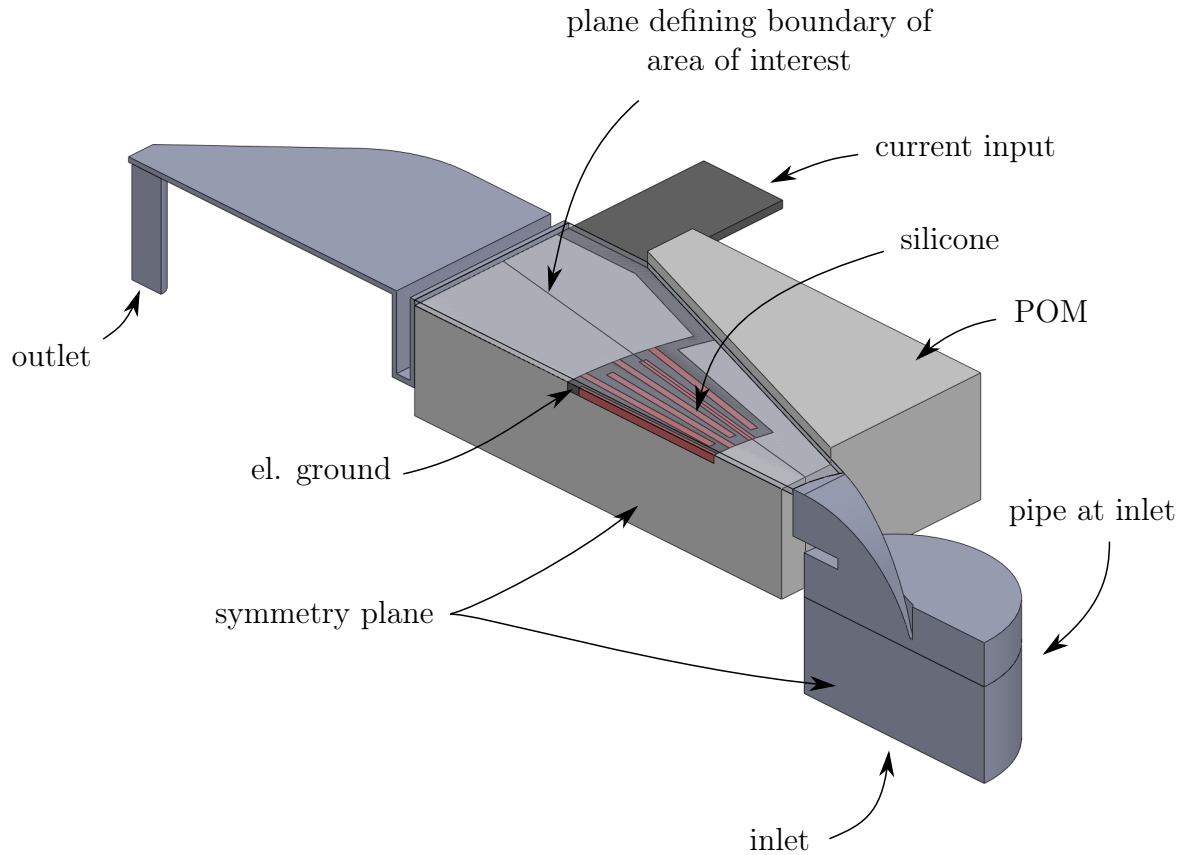


Figure 8.1: Overview of the setup used to simulate the heat transfer experiment in COMSOL.

8.2 Boundary conditions and physical modeling

In order to decide which physical model should be used for the calculation of the fluid flow, the flow characteristics had to be considered. As it was mentioned in the theory chapter, the value of the Reynolds number is decisive for whether the flow is laminar or turbulent. Since the value of the Reynolds number probably reached its maximum value at the start of the gap, its value was calculated for the velocity in this area. The hydraulic diameter for the flow between two parallel plates is defined to twice the plate distance (see section 5.2). In the experiment a maximum flow rate of less than 1 kg/min was applied which is why the Reynolds number was calculated for this mass flow rate. For the radius r in equation 8.1 a value of $4,5 \text{ cm}$ was used since this is the radius at which the gap starts. Due to the fact that an increase of the plate distance increased the cross section

of the flow path but increased the hydraulic diameter by the same amount, the value of the Reynolds number was independent of the gap width and calculated to:

$$Re = \frac{\bar{u} d_h}{\nu} = \frac{\dot{m} \rho}{\frac{40}{360} 2 \pi r \nu} \approx 1057 \quad (8.1)$$

As mentioned in the section describing the definitions of the analytical model (section 5.2), the flow for this flow problem is considered to be laminar for Reynolds number values of less than approximately 2200 – 3600. Consequently the fluid part of the problem was modeled with a physical model for laminar flow.

The temperature distribution and the flow through the geometry was modeled with the “Conjugated Heat Transfer Model for laminar flow”. This physical model combines the ability to calculate the CFD part of the problem and the heat transfer in solids as well as in fluids. The electric part of the problem, namely the current flow through the coil element and the resulting resistive losses were calculated using the “Electrical currents” model. The physical models were linked to each other by defining the heat generated due to the resistive losses in the coil element as heat source in the conjugated heat transfer model.

Due to the fact that only half of the coil element was modeled, the surface of the coil element at the symmetry plane was defined as electrical ground, while the surface facing away from it was defined as current input as illustrated in Figure 8.1. For the current input the current density in normal direction to this boundary was set as boundary condition. The remaining boundary conditions that were applied are listed in Table 8.1.

Table 8.1: Boundary conditions that were applied in the simulation model.

Boundary	Boundary condition	
	thermal	fluid flow
outer surfaces	thermal insulation	No-Slip
Symmetry plane	thermal insulation	Symmetry
Inlet	T_{in}	Mass flow rate (\dot{m})
Outlet	Outflow	$P = 1 \text{ atm}$

Based on the measurements described in section 7.6.2 the electrical resistance of the coil was defined as linearized resistance using the following formula:

$$R = R_{ref} (1 + \gamma (T - T_{ref})) \quad (8.2)$$

with $\gamma = 2,111 e^{-3} K^{-1}$ and $T_{ref} = 27^\circ C$. The reference resistance was taken from the data sheet that was provided by the manufacturer [1]. This value had however to be corrected by a factor of 1,078 to match the resistance that was measured for the coil

element (see section 7.6.2). All other material properties were set in accordance to the values listed in Table 7.2. In order to take into account the influence of the change in density due to changes in temperature in the fluid flow, the gravitational acceleration was applied in the negative y-direction (pointing downwards).

8.3 Solver

All cases were simulated at steady-state conditions and were calculated using a segregated solver. The segregated solver involved three steps. One of them solved the electrical part of the problem, calculating the resistive losses in the coil element. A second step solved the heat transfer problem and a third step the fluid flow. All these steps were linked together and the values of the variables solved by the different solver steps were updated after every iteration.

For the segregated step calculating the current flow through the coil element, the solver “conjugate gradients” was used while the temperature distribution and the fluid flow were solved by the “GMRES” solver. For both of the solvers the default setting were used. The demanded residual convergence condition was however changed from 10^{-3} to 10^{-6} . By setting the value of the demanded residual convergence to 10^{-7} and comparing the results with the ones that were obtained when this value was set to 10^{-6} , it was checked whether the returned solution was fully converged. The comparison of the results showed only very small changes of approximately $0,01\text{ }^{\circ}\text{C}$ for the average coil element temperature and the solution was therefore considered to be fully converged.

8.4 Mesh

As described above, the simulated geometry was reduced as much as possible in order to decrease the number of mesh elements without loss in quality of the obtained results. In order to use the mesh elements in an effective way, different mesh sizes were set depending on the significance of the meshed region on the results. For being able to do so, the geometry was divided into several parts as illustrated by an exploded view of the geometry in Figure 8.2. Various settings were tested in order to optimize the generated mesh. As many parameters and simulations were involved in this process, not all of the tested mesh parameters and the associated results are presented in the following sections, but only a selection to point out the relevance of the mesh settings. These simulations were carried out for a mass flow rate of $\dot{m} = 190\text{ g}/\text{min}^2$, a current of $I = 99\text{ A}$ and a water temperature

²This mass flow rate is the amount of water flowing through the complete model. Since only half of the geometry is modeled in the simulation a flow rate of $95\text{ g}/\text{min}$ was used in the simulation.

of $T_{in} = 22,7^\circ\text{C}$ ³.

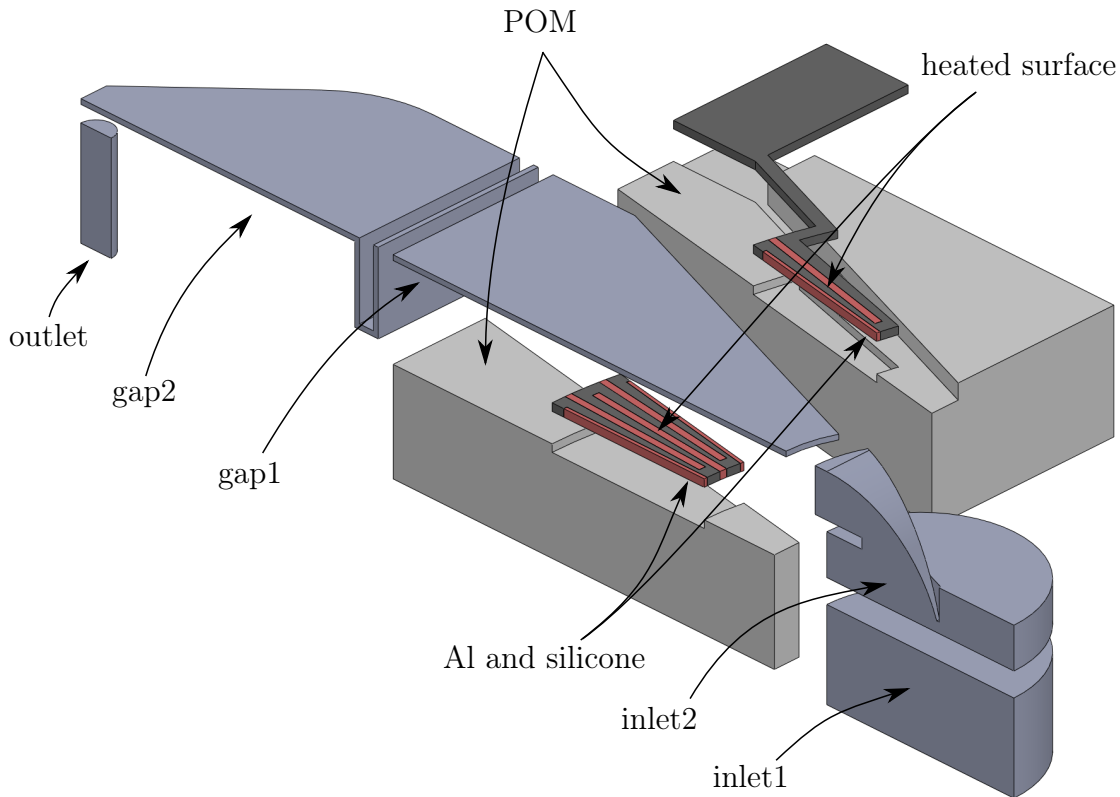


Figure 8.2: Exploded view of the simulation model.

8.4.1 Influence of the number of mesh elements

The influence of the total number of mesh elements on the calculated average heat transfer coefficient ($\bar{\alpha}$) and the average temperature of the coil element T_c is displayed in Figure 8.3.⁴ From the figure it can be seen that the coil element temperature was calculated to $34,5^\circ\text{C}$ using approximately 110.000 mesh elements, while the calculated value of T_c converged to approximately $37,4^\circ\text{C}$ when a mesh consisting of 800.000 or more elements was used. A similar correlation between the number of mesh elements and the resulting average heat transfer coefficient is visible in the figure. The value of $\bar{\alpha}$ was calculated to a value of $1300 \text{ W/m}^2\text{K}$ using a mesh consisting of roughly 110.000 elements, whereas the value of $\bar{\alpha}$ converged to approximately $1000 \text{ W/m}^2\text{K}$ when the number of mesh

³The mesh parameters that were used in these simulations can be found were summarized in an Excel file which was included in the ZIP that was submitted with the thesis.

⁴The value of $\bar{\alpha}$ was calculated using the formulas from section 7.3.1

elements was increased to 800.000 or more. Thus, the calculated value of $\bar{\alpha}$ changed by approximately 30 % in dependence of the number of mesh elements.

This outcome is not surprising and had to be expected but demonstrates the importance of the mesh that is used in the simulation on the results. Obviously, an increase of the number of mesh elements leads to higher computational costs, is however of great importance for the quality of the obtained results. A sufficiently high mesh quality is therefore inevitable for obtaining reliable results.

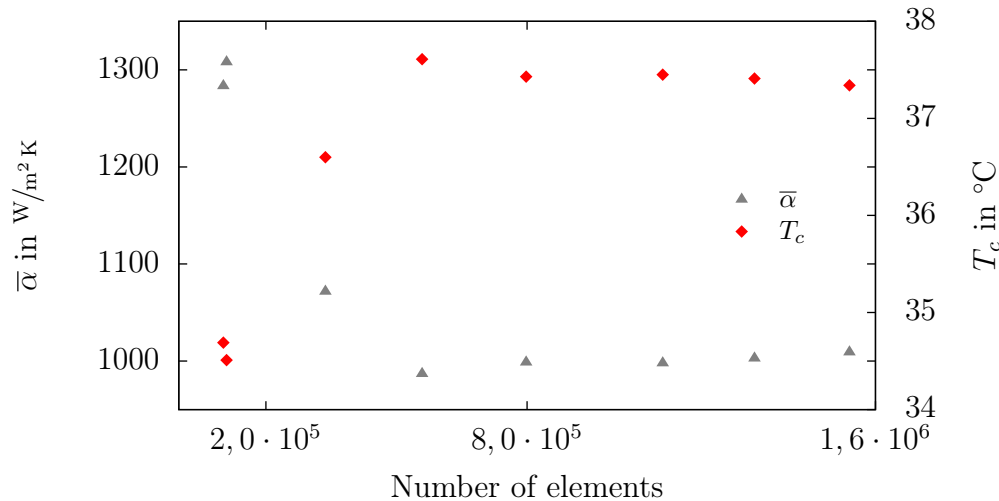


Figure 8.3: Influence of the total number of mesh elements on the calculated values of $\bar{\alpha}$ and T_c .

8.4.2 Influence of the boundary between heated area and water

The influence of the settings used for the thermal boundary between the heated area (surface of aluminum and silicone) and the water side showed large influence on the obtained results. Figure 8.4 shows the simulation results for T_c in dependence of the values that were set for the minimal and maximum element size on the boundary between the heated area and water.

From the figure it can be observed that the temperature of the coil element was calculated to a lower value when the element size limits of the boundary mesh were set to higher values compared to the calculated value of T_c when the limits were set to lower values. When the element size was set to a length between 2 mm and 6,6 mm, T_c was calculated to 34,5 $^{\circ}\text{C}$, whereas the same variable was calculated to approximately 37,4 $^{\circ}\text{C}$ when the minimum and maximum limits for the element size were set to 20 μm and 0,5 mm, respectively. Decreasing the maximum element size further below 1,3 mm caused only relatively small changes in the calculated of less than in 0,3 $^{\circ}\text{C}$.

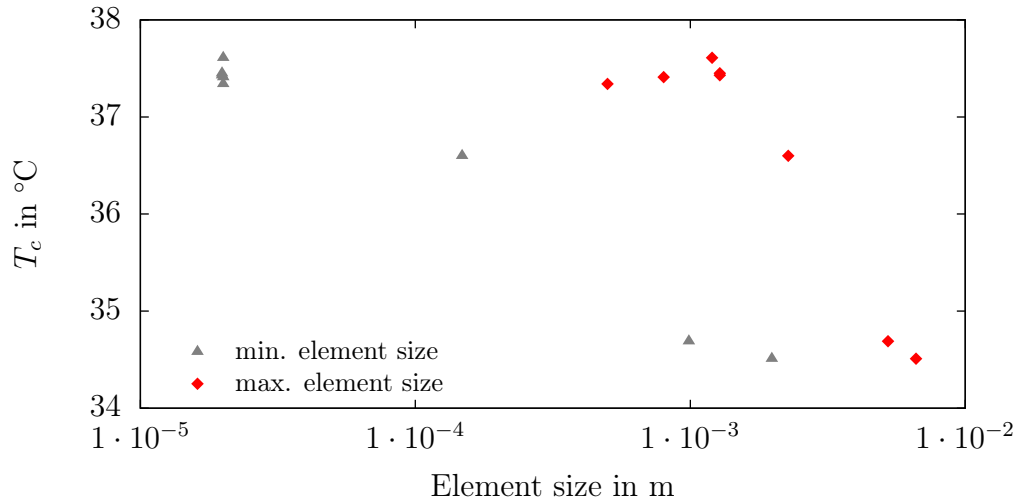


Figure 8.4: Simulation results for T_c in dependence of the minimum and maximum element size limits for the boundary mesh between the heated area and water.

Table 8.2: Element size limits of boundary mesh and resulting total number of mesh elements and calculated value of T_c .

Total number of mesh elements	Element size		T_c in °C
	min. in mm	max. in mm	
102458	0,99	5,24	34,69
797797	0,02	1,28	37,43

Since also other mesh parameters were changed between the different simulations plotted in Figure 8.4 the calculated value of T_c might have been affected by other mesh parameters. To ensure that the boundary mesh between the heated area and water was the mesh size parameter that led to the change in the calculated temperature, two simulations were carried out. Both simulations were using the same mesh parameters except for the element size limits of the boundary mesh elements between heated area and water which are listed in Table 8.2.

As it can be seen from the values listed in Table 8.2 the size of the mesh elements used for the boundary between the heated area and water was the parameter which led to a large change in the calculated coil element temperature.

Based on this correlation between mesh size and the calculated value of T_c , the size of the mesh elements on the boundary between the heated area and water was set to a size between 20 μm and 0,5 mm. This size was chosen although the results showed to be mesh independent for a slightly higher value for the maximum element size in order to ensure that the mesh covers the thermal boundary layer in a sufficiently precise way for cases

with larger temperature gradients at the boundary. The mesh-parameters that were used in the final layout of the simulation are displayed in Table 8.3.

In addition to the considerations concerning the mesh that were described in this and the previous section, the simulation results obtained with the final mesh parameters were checked on mass and energy conservation. The difference between the mass flow entering and exiting the geometry at inlet and outlet was evaluated to less than 0,5 %. Energy conservation was tested by evaluating the energy that was transferred to the water and the resistive losses in the coil element. The difference between these two values was calculated to less than 0,8 %.

Table 8.3: Mesh-parameters that were used in the simulation.

Mesh part	Mesh size limits		Max. element growth rate	Resolution of curvature	Resolution of narrow regions
	Min. mm	Max. mm			
Inlet1	0,395	3,66	1,10	0,40	0,9
Inlet2	0,4	2	1,13	0,50	0,8
Outlet	0,395	3,66	1,10	0,40	0,9
Gap1	0,20	1,50	1,08	0,30	0,95
Gap2	0,40	1,80	1,08	0,30	0,95
Heated surface	0,02	0,50	1,08	0,30	0,95
Al and silicone	1,50	20,00	1,20	0,3	0,85
POM	3,8	30,40	1,45	0,50	0,6

8.5 Evaluation

For being able to compare the simulation results with the measurement results of the experiment, the same values as the ones in the experiment were used for the mass flow through the geometry, the current through the coil and the water temperature at the inlet. The values for the temperatures at the positions of the thermocouples in the experiment were evaluated by deriving the temperatures at these positions using the tools “Data sets” and “Derived values”. These values were then exported and evaluated with a MATLAB code⁵.

The model was divided into several parts as demonstrated by the exploded view of the setup in Figure 8.2. By this division values such as \dot{Q}_{cond} (see section 8.5) could be evaluated by integration over the boundaries of each domain.

For the comparison of the simulation results with the ones that were measured in the experiment, $\bar{\alpha}$ was calculated using the equations in section 7.3.1. The results of this comparison are described in chapter 12. However, this calculation method is based on

⁵The MATLAB code that was used was included in the ZIP file that was submitted with the thesis.

a number of approximations due to the fact that the average surface temperature of the area of interest (see Figure 7.6) could not be measured during the experiment. In contrast to the experiment, the average surface temperature of the heat transfer area T_s could be evaluated in the simulation. With this value, the average heat transfer coefficient could be calculated in a more accurate way by using the actual value of T_s instead of T_c and the heated area (including the surface area of the silicone):

$$A_{ht} = \pi ((150 \text{ mm})^2 - (90 \text{ mm})^2) \cdot \frac{40^\circ}{360^\circ} \approx 50,3 \text{ cm}^2. \quad (8.3)$$

as heat transfer area. With these values average surface heat transfer coefficient (based on T_s) was calculated using the following equations:

$$\bar{\alpha}_{T_s} = \frac{V_c I - \dot{Q}_{cond}}{A_{ht} LMTD} \quad (8.4)$$

with

$$LMTD = \frac{(T_s - T_{in}) - (T_s - T_m)}{\ln \left(\frac{T_s - T_{in}}{T_s - T_m} \right)} \quad (8.5)$$

The results that were obtained using this calculation method are presented in chapter 13.

Part III

Results

9 | Analytical heat transfer model

A parameter sweep was carried out for different design parameters, using the analytical model and MATLAB code described in section 5.3 and 5.4. This was done in order to study the influence of the different parameters on the resulting cooling performance. The results of these parameter sweeps are presented in this chapter.

9.1 Influence of the fluid velocity

The mean fluid velocity, \bar{u} , was varied from 0,05 m/s to 0,5 m/s with a step size of 0,01 m/s. All other parameters were held constant during the velocity sweep and are listed in table 9.1.

The influence of the mean fluid velocity on the outlet fluid temperature, T_{out} , and the heat transfer rate, \dot{Q} , is plotted in figure 9.1.

From figure 9.1 it can be observed that T_{out} declines in an exponential way with increasing \bar{u} -values in the region of relatively low fluid velocities. At higher values of \bar{u} , T_{out} converges to the inlet velocity, T_{in} . The highest and lowest values of T_{out} that were observed are 66,8 °C and 28,1 °C at a fluid velocity of 0,05 m/s and 0,5 m/s, respectively. The heat transfer rate, \dot{Q} , increases with increasing \bar{u} -values. An increase of the fluid velocity leads to a larger increase of \dot{Q} in regions of relatively low \bar{u} -values. At higher velocities the gradient $d\dot{Q}/d\bar{u}$ declines. The average values that were observed for $d\dot{Q}/d\bar{u}$ in different velocity regions are listed in table 9.2.

The influence of the velocity on the heat that is transferred per unit mass (\dot{Q}/\dot{m} , with

Table 9.1: Parameters that were held constant during the fluid velocity sweep.

Parameter	value	unit
b	2	m
L	0,5	m
d	2	mm
T_c	90	°C
T_{in}	15	°C

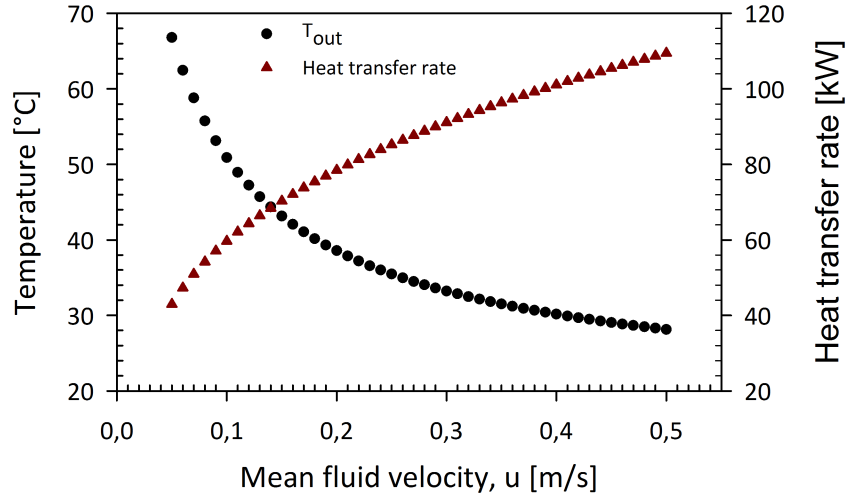


Figure 9.1: Influence of the mean fluid velocity, \bar{u} , on the fluid outlet temperature, T_{out} , and the heat transfer rate, \dot{Q} .

Table 9.2: Values of the gradient $d\dot{Q}/d\bar{u}$ in different fluid velocity regions.

Velocity region	$d\dot{Q}/d\bar{u}$ in kW/m s
0,05 – 0,07 m/s	398,5
0,07 – 0,10 m/s	292,7
0,10 – 0,15 m/s	212,6
0,15 – 0,20 m/s	163,0
0,20 – 0,30 m/s	126,4
0,30 – 0,40 m/s	99,7
0,40 – 0,50 m/s	83,9

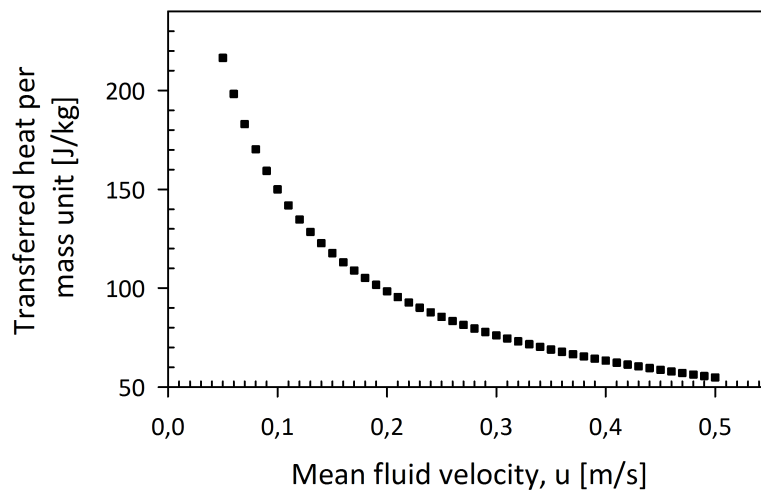


Figure 9.2: Influence of the mean fluid velocity on the heat transfer per mass unit.

\dot{m} being the Mass flow rate) is plotted in figure 9.2. It can be seen that the amount of heat removal per mass unit decreases significantly with increasing fluid velocities in regions of relatively low \bar{u} -values. At a fluid velocity of 0,05 m/ s an amount of heat of 216,5 J is removed per kg, while 54,9 J are removed per kg at a velocity of 0,5 m/ s. The effect that an increasement of the Mass flow rate will have on the heat that is removed per mass unit ($d\dot{Q}/d\dot{m}$) is displayed in figure 9.3. Figure 9.3 shows the same characteristics as the gradient of $d\dot{Q}/d\bar{u}$, listed in table 9.2.

Figure 9.4 shows that the Reynolds number increases approximately linearly with increasing \bar{u} -values with a minimum value of 309 at $\bar{u} = 0,05$ m/s and a maximum value of 2064 at $\bar{u} = 0,5$ m/s. The Nusselt number describes a similar shape as \dot{Q} with the minimum and maximum values of 6,16 at $\bar{u} = 0,05$ m/s 10,68 at $\bar{u} = 0,5$ m/s, respectively.

9.2 Influence of the plate distance

The plate distance, d , was varied from 1 mm to 1 cm with a step size of 0,1 mm. All other parameters were held constant during the velocity sweep and are listed in table 9.3.

The influence of the plate distance on the outlet fluid temperature, T_{out} , and the heat transfer rate, \dot{Q} , is plotted in figure 9.5.

Figure 9.5 indicates that the smaller the distance between the plates is, the higher the temperature of the fluid at the outlet gets. The maximum outlet temperature was calculated to 73,5°C at the minimum plate distance of 1 mm. T_{out} drops by 41,7°C when the plate distance is increased from 1 mm to 3 mm. When the plate distance is increased further, T_{out} converges to the fluid inlet temperature, T_{in} , of 15 °C. Increasing d from 3 mm to 1 cm leads to a fluid outlet temperature drop of 8,1 °C. The minimum outlet

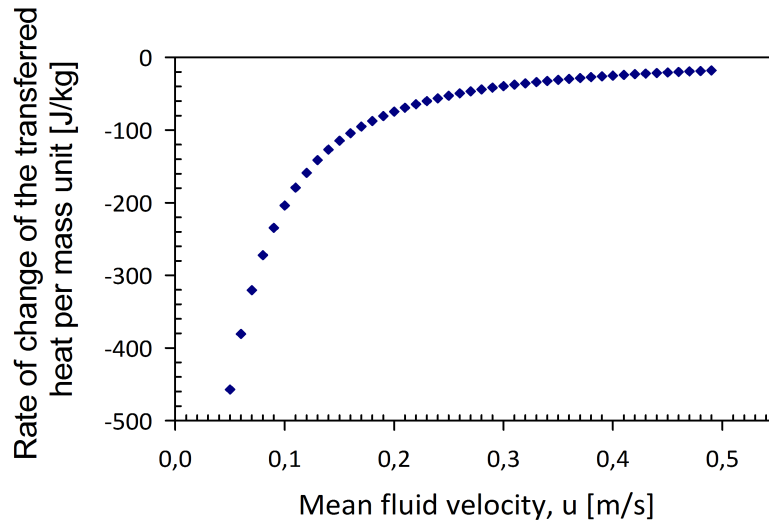


Figure 9.3: Influence of the mean fluid velocity on the rate of change of the heat that is transferred per mass unit.

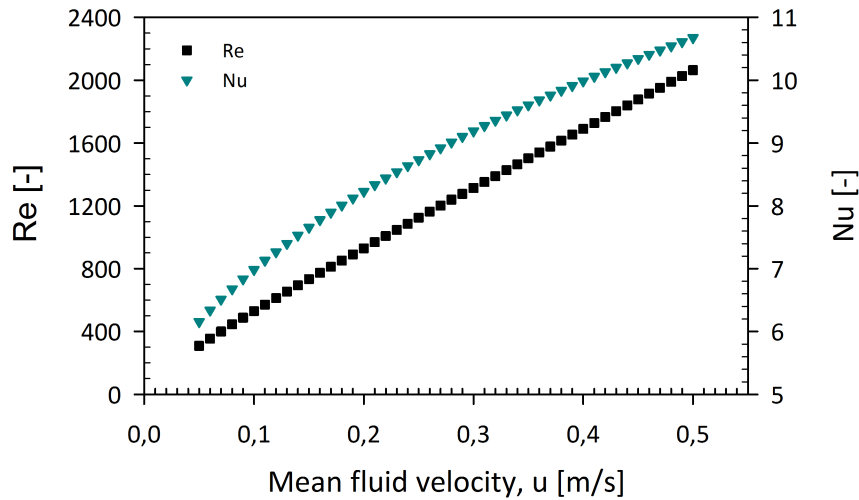


Figure 9.4: Influence of the mean fluid velocity, \bar{u} , on the resulting Reynolds number, Re , and average Nusselt number, Nu .

Table 9.3: Parameters that were held constant during the fluid plate distance sweep.

Parameter	value	unit
b	2	m
L	0,5	m
\bar{u}	0,15	m/s
T_c	90	°C
T_{in}	15	°C

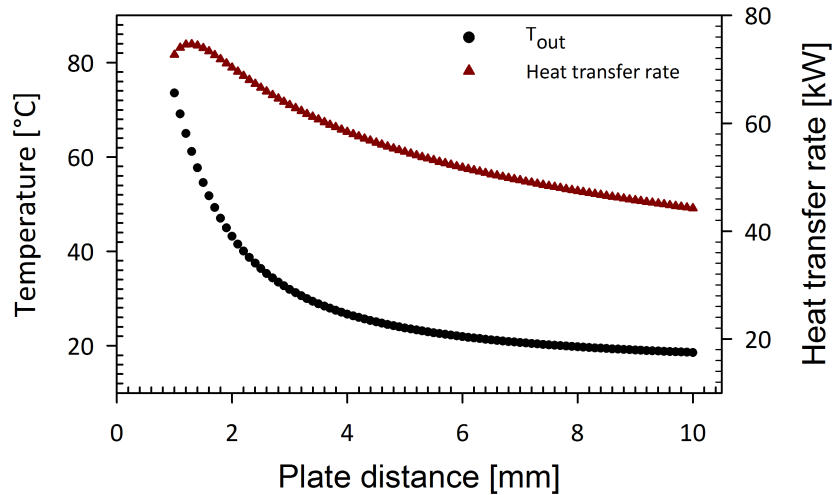


Figure 9.5: Influence of the plate distance, d , on the fluid outlet temperature, T_{out} , and the heat transfer rate, \dot{Q} .

temperature of 18,52 °C was obtained at the maximum plate distance of 1 cm.

The heat transfer rate, \dot{Q} , reaches its maximum value of 74,7kW at a plate gap of 1,3mm. An increase or decrease of d from this point leads to a decrease of \dot{Q} . The increase of the gap between the plates shows the largest influence on \dot{Q} in regions close to the maximum value of \dot{Q} . At larger plate distances, this influence decreases.

The influence of the plate distance on the rate of transferred heat per mass unit is displayed in figure 9.6. Figure 9.7 shows the rate of change of the heat removal per mass unit ($d\dot{Q}/d\dot{m}$) when the Mass flow rate is increased by increasing the plate distance.

At small plate distances an increase of d leads to a significant drop in the amount of heat that is removed from the plate per kg water (figure 9.6 & 9.7). At a plate distance of 1 mm 244,2 J heat are removed per kg water, which is approximately five times the amount that is removed by one kg at a plate distance of 4 mm

Figure 9.8 displays the calculated Reynolds number, Re , and average Nusselt number, Nu , over the swept plate distance range. An observation of figure 9.8 shows that an increase of the plate distance has a similar influence on the Reynolds number and the average Nusselt number as the increase of the mean fluid velocity, \bar{u} , which was studied in section 9.1. The Reynolds number increases almost linearly from 492 and 2750 between the minimum and maximum plate distance. The average Nusselt number increases approximately linearly from its minimum value of 5,92 to its maximum value of 20,40 when the plate distance is increased from 1 mm to 1 cm.

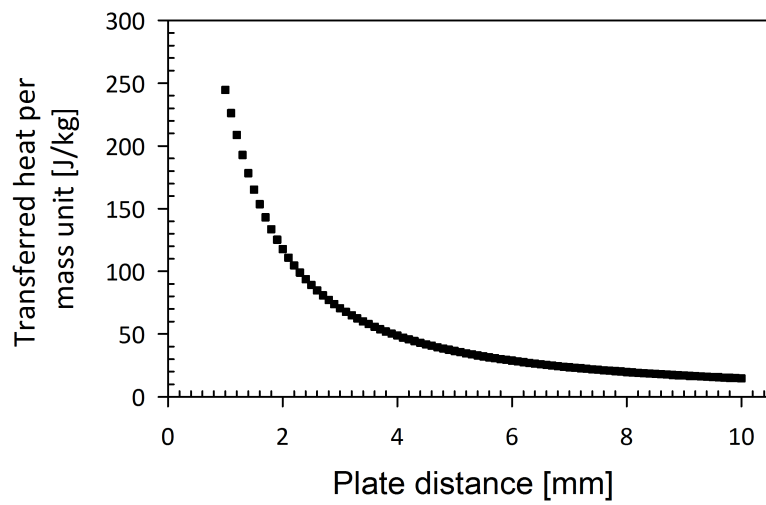


Figure 9.6: Influence of the mean fluid velocity on the heat transfer per mass unit.

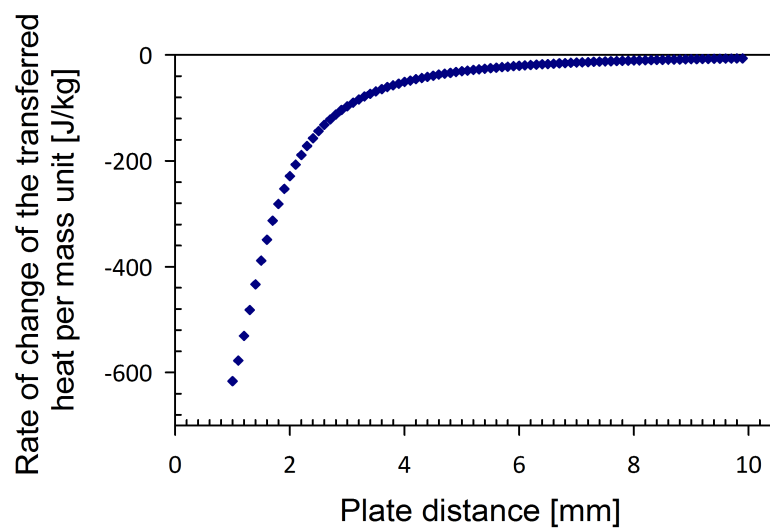


Figure 9.7: Influence of the plate distance on the rate of change of the heat that is transferred per mass unit.

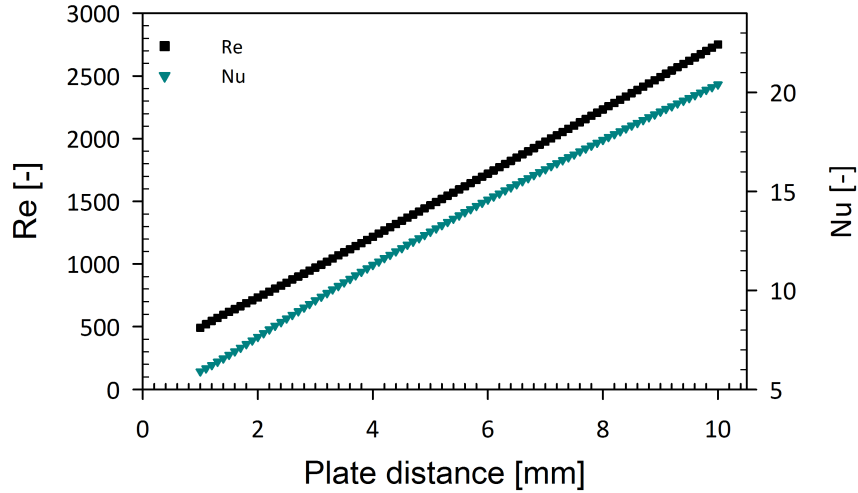


Figure 9.8: Influence of the plate distance, d , on the resulting Reynolds number, Re , and average Nusselt number, Nu .

Table 9.4: Parameters that were held constant during the parameter sweep of the heated plate length.

Parameter	value	unit
b	2	m
d	2	mm
\bar{u}	0,15	m/s
T_c	90	°C
T_{in}	15	°C

9.3 Influence of the heated plate length

The length of the heated plate, L , was varied from 0 to 2 m with a step size of 10 cm. All other parameters were held constant during the velocity sweep and are listed in table 9.4. The influence of the heated plate length on the outlet fluid temperature, T_{out} , and the heat transfer rate, \dot{Q} , is plotted in figure 9.9. Figure 9.10 displays the calculated Reynolds number, Re , and average Nusselt number, Nu , over the swept heated plate length range.

From figure 9.9 it can be seen that both, T_{out} and \dot{Q} , increase with the heated plate length. The gradient dT_{out}/dL is largest in the region of short plate lengths. With increasing L -values the gradients dT_{out}/dL and $d\dot{Q}/dL$ decrease. Table 9.5 gives an overview of the gain of \dot{Q} and increase of T_{out} that results from adding half a meter to the plate length, depending on how long the plate was before.

The average Nusselt number Nu decreases with an increase of L , as shown in figure 9.10. This drop of Nu is especially large when the plate is prolonged in the region of plate lengths of 0 – 0,5 m. The Reynolds number, increases with increasing values of L .

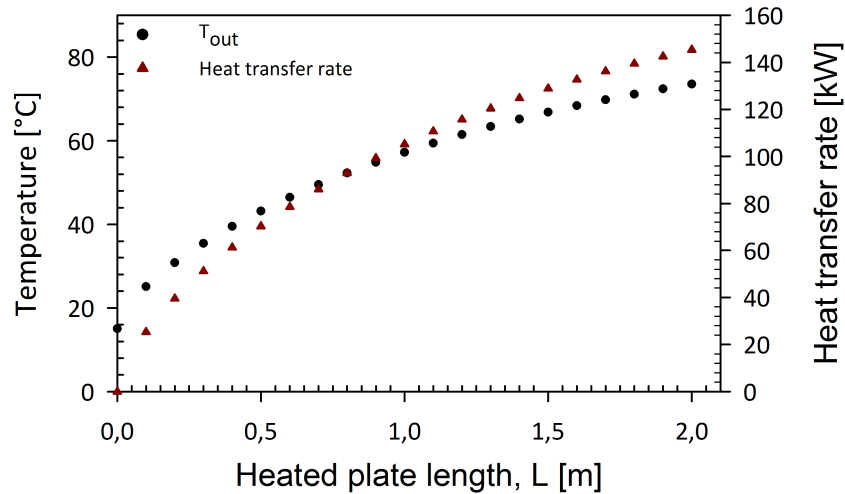


Figure 9.9: Influence of the heated plate length, L , on the fluid outlet temperature, T_{out} , and the heat transfer rate, \dot{Q} .

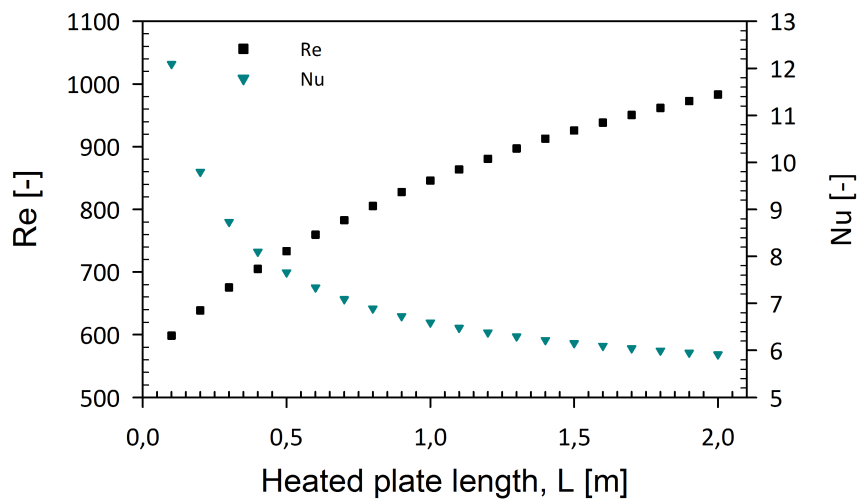


Figure 9.10: Influence of the heated plate length, L , on the resulting Reynolds number, Re , and average Nusselt number, Nu .

Table 9.5: Increase of \dot{Q} and T_{out} resulting from adding half a meter to the plate length for different initial plate lengths.

Increase in plate length from – to	\dot{Q} gain due to added plate length in kW	Rise of T_{out} due to added plate length in °C
0,0 m – 0,5 m	70,3	28,2
0,5 m – 1,0 m	34,8	14,1
1,0 m – 1,5 m	23,7	9,6
1,5 m – 2,0 m	16,5	6,7

This increase of Re with increasing L -values flattens, however, out at longer plate lengths and seems to converge to a value of approximately 1000 – 1100.

10 | 2D Heat transfer simulation

In order to estimate the accuracy of the simulation which was carried out, the results were compared to the ones of the analytical model, which is shown in figure 10.1. An observation of figure 10.1 reveals that the simulation results are almost identical with the analytical ones for velocities up to 0,3 m/s. Above this velocity a slight difference of the calculated outlet temperature can be seen, which has a larger effect on the heat transfer rate. The maximum deviation of T_{out} and \dot{Q} is found at a velocity with a value of 1,33 °C and 11,38 kW.

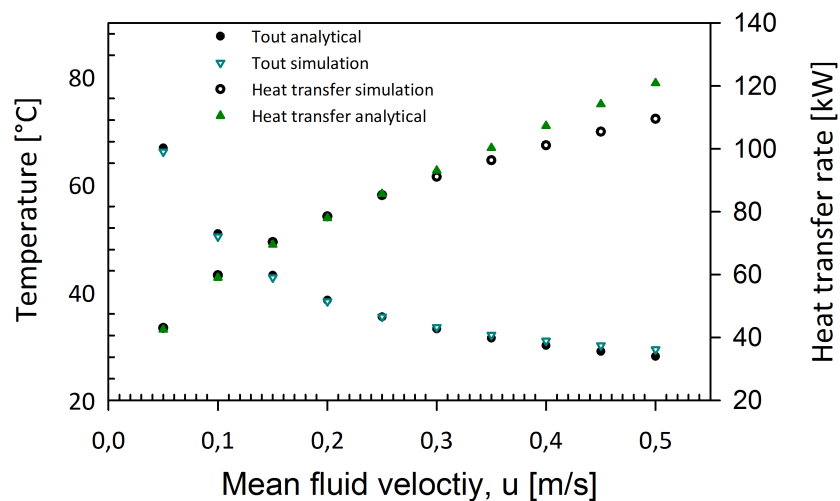


Figure 10.1: Comparison between the results from the analytical model and numerical simulation for the heat transfer problem with one heated plate and laminar flow.

11 | Experiment

11.1 Nonuniform flow

To investigate the effect that nonuniform flow distributions will have in the cooling system, half of the flow path was blocked with an obstacle at the start of the gap. For being able to measure the resulting temperature of the coil element on the blocked side, the obstacle was placed on the side of the thermocouples (see Figure 7.6. Subsequently the air gap was set to 2 mm, the current to $I = 80 \text{ A}$ and a mass flow rate of 770 g/min was applied. The resulting temperature level of T_c in dependence of time is displayed in Figure 11.1 in which the time scale starts at the point when the current was switched on. After approximately 8 minutes, the power supply was turned off.

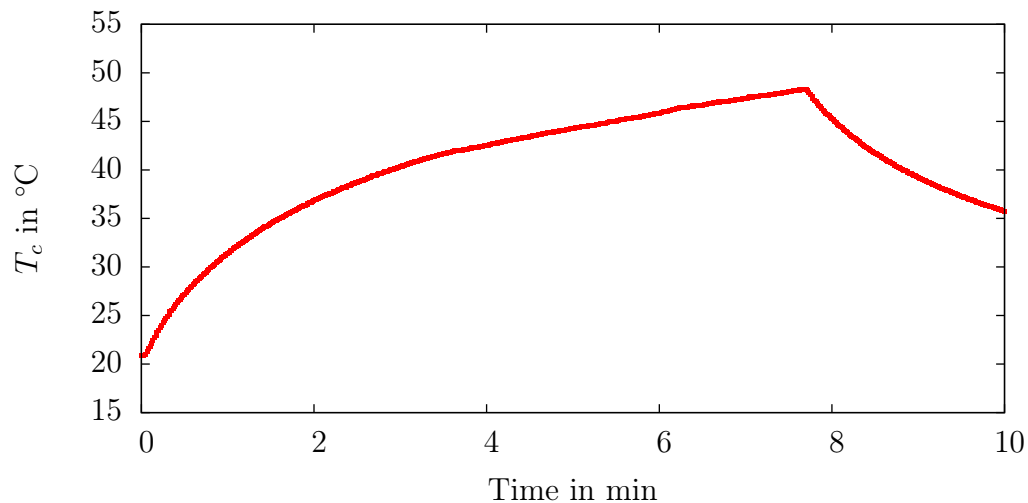


Figure 11.1: Resulting average coil element temperature which was measured with nonuniform flow distribution throughout across the coil element.

As it can be seen in Figure 11.1, the T_c raised by $27,5^\circ\text{C}$ from $20,8^\circ\text{C}$ to $48,3^\circ\text{C}$ within less than 8 minutes. Right after the current was switched on the temperature increased drastically. After approximately 4 minutes the temperature rise slowed down to a almost linearly increase with time. To prevent damages of the experimental setup, the current

was switched off at a temperature of almost 50°C. After the power source was turned off, the temperature declined rapidly in a logarithmic way.

11.2 Maximum cooling capacity

In order to evaluate the maximum cooling performance of the experimental model, the current flowing through the coil and the water flow rate were set to the highest possible values which were $I \approx 195 \text{ A}$ and $\dot{m} \approx 900 \text{ g/min}$. After these parameters were applied it was waited until the temperature of the coil element had reached a steady level. At the end of the experiment, the current was switched off to estimate how quickly the coil element is cooled down by the water when no current is flowing through it. The resulting temperature of T_c is displayed in Figure 11.2 in which the current was switched of at $t = 165 \text{ s}$.

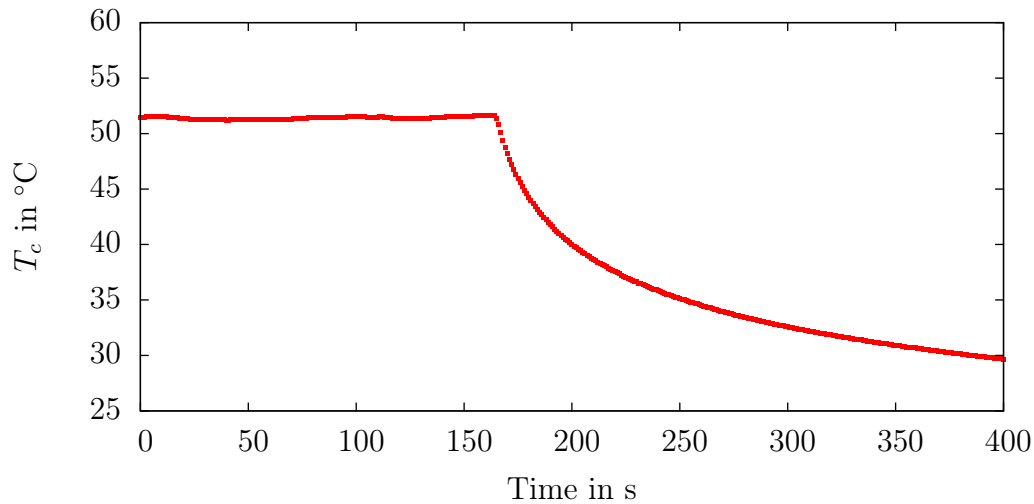


Figure 11.2: Resulting average coil element temperature at maximal current and flow rate. At $t = 165 \text{ s}$, the current was switched off.

As it can be seen from Figure 11.2, the T_c converged to a temperature level of approximately 51,4°C. After the current was switched off the temperature decreased exponentially. The temperature fell by 5,25, 8,4, and 10,7°C within the first 10, 20, and 30 seconds.

12 | Comparison of experimental and simulation results

As already mentioned, the cases that were investigated in the experiment were subsequently simulated using the same parameters (\dot{m} , T_{in} , I) as in the experiment. The values that were obtained for the average surface heat transfer coefficient ($\bar{\alpha}$)¹ from the measurements taken during the experiment and the ones that were simulated are presented in Figure 12.1 and Figure 12.2. In both figures $\bar{\alpha}$ is plotted in dependence of the mass flow rate \dot{m} . The results that were obtained with a gap width of 2 mm are shown in Figure 12.1 and the ones with a gap width 4 mm in Figure 12.2. The results of the most important variables with a gap width of 2 mm and 4 mm are listed in Table 12.1 and 12.2, respectively.

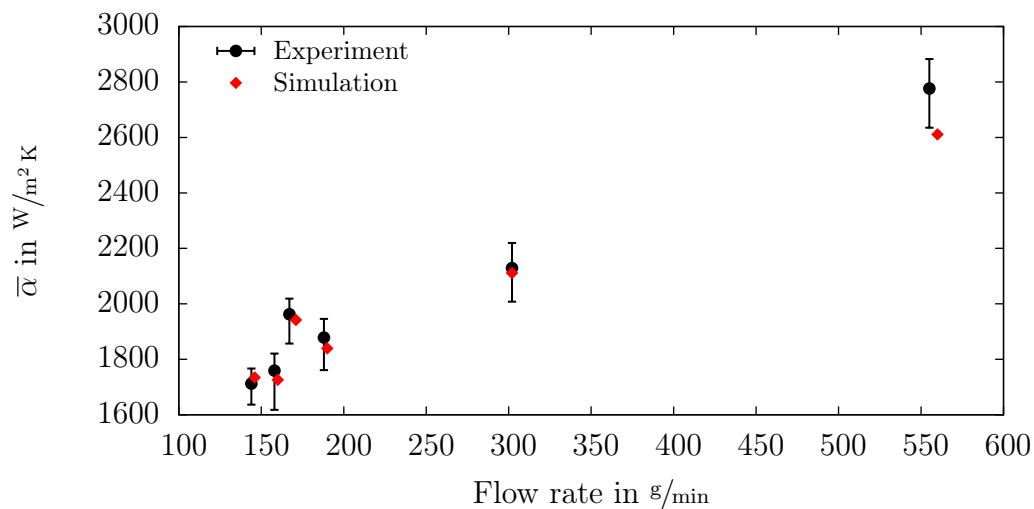


Figure 12.1: Comparison of the experimental and simulation results for $\bar{\alpha}$ in dependence of the mass flow rate at a gap width of 2 mm.

¹These values were calculated using the equations given in section 7.3.1. As it was mentioned in section 7.3.2 a number of assumptions were made in this calculation method. Therefore, the calculated values of $\bar{\alpha}$ are subject to an error (see section 7.3.3) and were only used for being able to compare the simulation results with the experimental ones.

Table 12.1: Overview of the results obtained from numerical simulations and experiment for a gap width of 2 mm.

	\dot{m} g/min	I A	T_{in} °C	T_{out} °C	T_c °C	T_{max} °C	$\bar{\alpha}$ W/m ² K	ΔT_c °C	$\Delta LMTD$ °C	$\Delta\bar{\alpha}_+$ %	$\Delta\bar{\alpha}_-$ %
Sim.	171	151,3	22,0	32,9	56,8	64,1	1942	-	-	-	-
Ex.	167	151,3	22,0	32,4	55,8	60,3	1962	0,11	0,40	2,9	5,4
Sim.	146	109,2	19,5	25,8	39,2	42,8	1734	-	-	-	-
Ex.	144	109,2	19,6	25,7	39,0	40,8	1713	0,05	0,29	3,2	4,4
Sim.	160	80,6	23,8	26,9	34,3	36,1	1726	-	-	-	-
Ex.	158	80,6	23,8	26,8	34,1	35,9	1759	0,04	0,18	3,5	8,0
Sim.	302	100,5	22,2	24,8	34,6	37,3	2111	-	-	-	-
Ex.	302	100,5	22,2	24,3	34,7	36,9	2129	0,04	0,36	4,2	5,7
Sim.	560	128,5	22,4	24,9	38,3	42,5	2611	-	-	-	-
Ex.	555	128,5	23,5	24,8	37,9	41,5	2777	0,05	0,39	3,8	5,1
Sim.	190	99,0	22,7	26,8	37,3	40,2	1839	-	-	-	-
Ex.	188	98,7	22,6	26,4	37,0	40,3	1879	0,05	0,28	3,6	6,3

12.0.1 Results obtained with a 2 mm gap width

From Figure 12.1 it can be seen that the value of $\bar{\alpha}$ increased with increasing mass flow rates. The values of $\bar{\alpha}$ measured in the experiment varied between 1713 W/m² K and 2777 W/m² K at flow rates of 144 g/min and 555 g/min. In the simulation $\bar{\alpha}$ reached its maximum value of 2611 W/m² K at a flow rate of 560 g/min and its minimal value of 1726 W/m² K at a flow rate of 160 g/min.

The $\bar{\alpha}$ -values obtained from the experiment deviated between -1,3% and 2,1% from the simulated values at flow rates from ≈ 145 g/min to 302 g/min. The largest deviation between the simulation and experimental results was observed with 6% at a flow rate of ≈ 560 g/min.

From the values in Table 12.1 and the error-bars in Figure 12.1 it can be observed that the measurement uncertainty of $\bar{\alpha}$ in negative direction ($\Delta\bar{\alpha}_-$) reached from 4,4% to 8,0%, while the uncertainty of $\bar{\alpha}$ in positive direction ($\Delta\bar{\alpha}_+$) varied between 2,9% and 4,2%. As mentioned in section 7.9.1, the uncertainty of the mass flow rate ($\Delta\dot{m}$) was considered to be constant with 1,2 g/min. The error-bars corresponding error-bars were plotted in Figure 12.1, can however not be seen due to the low value of $\Delta\dot{m}$. The measurement uncertainty of the logarithmic mean temperature difference, $\Delta LMTD$ varied between 0,18 and 0,40 °C, while the measurement uncertainty of the average coil temperature on the non-cooled side, ΔT_c , was varied between 0,04 and 0,11 °C.

T_{max} which represents the temperature of the hottest part of the coil element was calculated as the average of the temperatures measured by thermocouple number 10 and

11 ($T_{max} = (T_{10} + T_{11})/2$)(see Figure 7.6). The lowest temperature obtained for this part of the coil element was 36,1 °C in the simulation and measured to 35,9 °C in the experiment with a current of 80,6 A and a flow rate of ≈ 160 g/min. A maximum value of 64,1 °C was calculated for T_{max} in the simulation and measured to 60,3 °C in the experiment when a current of 151,3 A and a flow rate of ≈ 170 g/min were applied.

12.0.2 Results obtained with a 4 mm gap width

From Figure 12.2 it can be seen that also for a gap width of 4 mm the value of $\bar{\alpha}$ increased with increasing mass flow rates. The values of $\bar{\alpha}$ measured in the experiment varied between 1034 W/m²K and 1661 W/m²K at flow rates of 197 g/min and 523 g/min. In the simulation $\bar{\alpha}$ reached its maximum value of 1683 W/m²K at a flow rate of 525 g/min and its minimal value of 1052 W/m²K at a flow rate of 198 g/min. The $\bar{\alpha}$ -values obtained from the experiment deviated between -1,7 % and 2,3 % from the simulated values.

Table 12.2: Overview of the results obtained from numerical simulations and experiment for a gap width of 4 mm.

	\dot{m} g/min	I A	T_{in} °C	T_{out} °C	T_c °C	T_{max} °C	$\bar{\alpha}$ W/m ² K	ΔT_c °C	$\Delta LMTD$ °C	$\Delta \bar{\alpha}_+$ %	$\Delta \bar{\alpha}_-$ %
Sim.	198	50,1	22,0	22,9	27,8	28,7	1052	-	-	-	-
Ex.	197	50,1	22,0	22,8	27,8	28,8	1034	0,04	0,35	7,3	9,4
Sim.	300	80,0	22,1	23,8	33,6	35,5	1377	-	-	-	-
Ex.	297	80,0	22,2	23,7	33,4	35,8	1409	0,05	0,67	7,1	8,8
Sim.	525	122,0	22,5	24,8	44,2	48,7	1683	-	-	-	-
Ex.	523	121,9	22,6	24,7	44,4	47,8	1661	0,06	1,13	6,1	7,3

From the values in Table 12.2 and the error-bars in Figure 12.2 it can be observed that the measurement uncertainty of $\bar{\alpha}$ in negative direction ($\Delta \bar{\alpha}_-$) reached from 7,3 % to 9,4 %, while the uncertainty of $\bar{\alpha}$ in positive direction ($\Delta \bar{\alpha}_+$) varied between 6,1 % and 7,3 %. Also in Figure 12.2 the error-bars representing the measurement uncertainty of the mass flow rate cannot be seen due to the same reason as mentioned in the previous section. The measurement uncertainty of the logarithmic mean temperature difference, $\Delta LMTD$, increased with increasing mass flow rates from 0,35 °C to 1,13 °C, while the measurement uncertainty of the average coil temperature on the non-cooled side, ΔT_c , was relatively constant and varied between 0,04 and 0,06 °C between the minimum and maximum mass flow rates that were applied.

The lowest temperature obtained for the hottest part of the coil element was calculated to $T_{max}=28,7$ °C in the simulation and measured to 28,8 °C in the experiment with a current of 50,1 A and a flow rate of ≈ 198 g/min. A maximum value of 48,7 °C was calculated

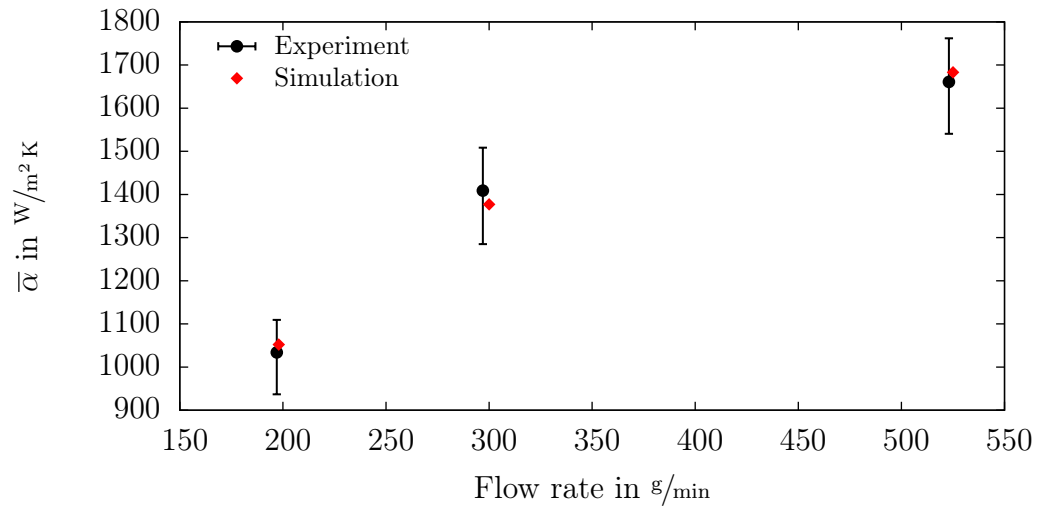


Figure 12.2: Comparison of the experimental and simulation results for $\bar{\alpha}$ in dependence of the mass flow rate at a gap width of 4 mm.

for T_{max} in the simulation and measured to $47,8^\circ\text{C}$ in the experiment when a current of 122 A and a flow rate of $\approx 525 \text{ g}/\text{min}$ were applied.

13 | Simulation

Due to the fact that several assumptions were made when the average surface heat transfer coefficient ($\bar{\alpha}$) was calculated using the calculation method that was described in section 7.3, the calculated values were only an estimation used to compare the measurement results with the ones from numerical simulations. Since the average surface temperature within the area of interest (displayed in Figure 7.6) could be evaluated in the simulation, the average heat transfer coefficient ($\bar{\alpha}_{T_s}$) based on the average surface temperature of the heated part within the area of interest (T_s) was calculated from the equations in section 8.5. The obtained results of $\bar{\alpha}_{T_s}$ are presented in this chapter and are compared to the ones of $\bar{\alpha}$. Since the distribution of the $\bar{\alpha}$ -values was already described in chapter 12 and will be discussed in chapter 17, the distribution of the calculated values of $\bar{\alpha}$ are not described in this chapter nor discussed in chapter 18.

The values of $\bar{\alpha}_{T_s}$ and $\bar{\alpha}$ that were calculated are illustrated graphically in Figure 13.1 and Figure 13.2. A summary of the most important values that were derived from the numerical simulations is given in Table 13.1 and Table 13.2 for a gap width of 2 and 4 mm, respectively. The variables in these tables stand for the surface temperatures within the area of interest (cooled side) of aluminum (T_{al}), silicone (T_{si}) and the average surface temperature within this region (T_s) which includes both, the silicone and aluminum surfaces. The variables for the heat transfer rate for each of the materials within the region of interest were named accordingly.

Table 13.1: Simulation results for a gap width of 2 mm.

\dot{m}	I	T_{al}	T_{si}	T_s	\dot{Q}_{al}	\dot{Q}_{si}	\dot{Q}_{POM}	\dot{Q}_{cond}	$\frac{\dot{Q}_{si}}{\dot{Q}_{al}}$	$\bar{\alpha}$	$\bar{\alpha}_{T_s}$	$\frac{\bar{\alpha}}{\bar{\alpha}_{T_s}}$
g/min	A	°C	°C	°C	W	W	W	W	—	W/m ² K	W/m ² K	—
171	151	56,8	35,9	47,3	32,7	5,6	0,72	0,45	0,17	1942	1632	1,19
146	109	39,4	28,2	34,3	16,3	2,8	0,40	0,29	0,17	1734	1407	1,23
160	81	34,3	28,5	31,7	8,8	1,5	0,22	0,16	0,17	1726	1375	1,26
302	101	34,6	27,0	31,1	14,1	2,1	0,33	0,18	0,15	2111	1706	1,24
560	129	38,1	27,8	33,4	23,8	3,1	0,52	0,21	0,13	2611	2162	1,21
190	99	37,4	29,0	33,6	13,5	2,2	0,33	0,22	0,16	1839	1476	1,25

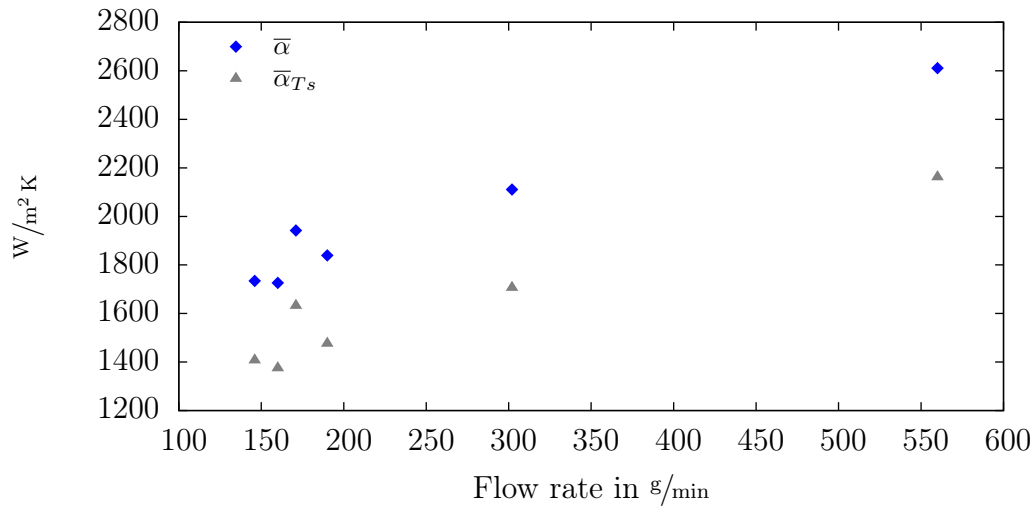


Figure 13.1: Comparison of $\bar{\alpha}$ and $\bar{\alpha}_{T_s}$ for a gap width of 2 mm.

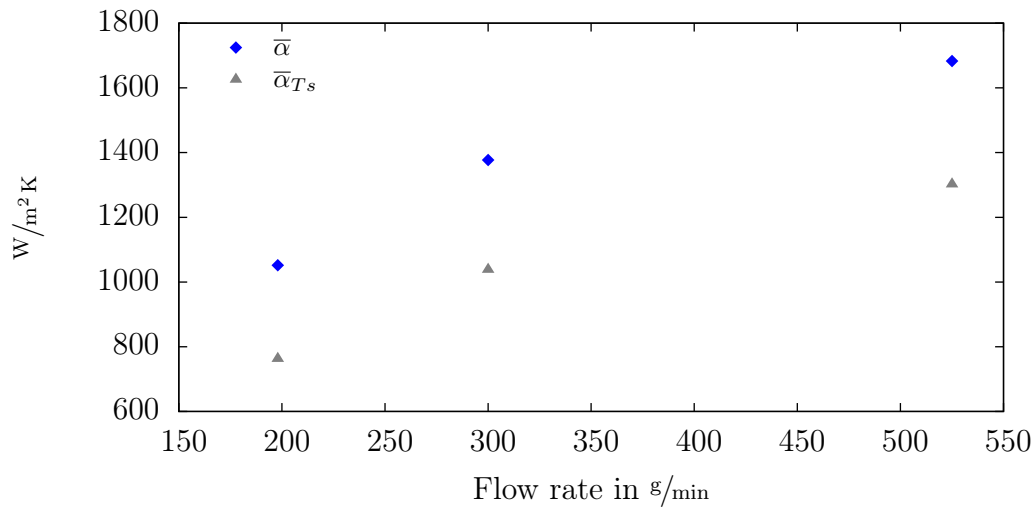


Figure 13.2: Comparison of $\bar{\alpha}$ and $\bar{\alpha}_{T_s}$ for a gap width of 4 mm.

Table 13.2: Simulation results for a gap width of 4 mm.

\dot{m}	I	T_{al}	T_{si}	T_s	\dot{Q}_{al}	\dot{Q}_{si}	\dot{Q}_{POM}	\dot{Q}_{cond}	$\frac{\dot{Q}_{si}}{\dot{Q}_{al}}$	$\bar{\alpha}$	$\bar{\alpha}_{T_s}$	$\frac{\bar{\alpha}}{\bar{\alpha}_{T_s}}$
g/min	A	°C	°C	°C	W	W	W	W	—	W/m ² K	W/m ² K	—
198	50	27,8	25,0	26,5	3,2	0,7	0,12	0,08	0,20	1052	763	1,38
300	80	33,5	27,4	30,7	16,7	3,2	0,55	0,31	0,19	1377	1038	1,33
525	122	43,9	31,4	38,2	40,9	7,0	1,18	0,56	0,17	1683	1302	1,29

An observation of the plotted values in Figure 13.1 and Figure 13.2 reveals that the values of $\bar{\alpha}$ were calculated to significantly higher values than $\bar{\alpha}_{T_s}$. However, the obtained results for $\bar{\alpha}_{T_s}$ showed the same distribution characteristics as the ones of $\bar{\alpha}$ for both gap widths. The fraction $\bar{\alpha}/\bar{\alpha}_{T_s}$, listed in Table 13.1 and Table 13.2, reveals that the deviation between the two values reached from 19 % to 26 % for a gap width of 2 mm and from 29 % to 38 % for a gap width of 4 mm. By taking a closer look at the results, it can be observed that the value of this fraction increased with increasing current densities in the coil element for both gap widths.

Furthermore, the fraction of the heat transferred from the silicone surface into the water compared to the heat which was transferred from the surface of the coil element ($\dot{Q}_{si}/\dot{Q}_{al}$) decreased from 17 %, at flow rates of less than 180 g/min, to 13 % at a flow rate of 560 g/min and a gap width of 2 mm. This fraction also declined with increasing flow rates for a gap width of 4 mm. Here the fraction decreased its value from 20 % to 17 % at $\dot{m} = 198$ g/min and $\dot{m} = 525$ g/min, respectively.

The heat transferred from the area of interest to the outer regions by conduction increased with rising temperature levels of the coil element. For a gap width of 2 mm the values of \dot{Q}_{cond} varied between 0,16 W and 0,45 W and between 0,08 W and 0,56 W for a gap width of 4 mm.

A comparison of the calculated values of T_c (listed in Table 12.1 and Table 12.2) and T_{al} showed a maximum deviation of 0,2 °C and 0,3 °C for a gap width of 2 mm and 4 mm, respectively. The results that were presented in this chapter are discussed in chapter 18.

Part IV

Discussion

14 | Analytical heat transfer model

14.1 Influence of the fluid velocity

At low fluid velocities an increase of \bar{u} showed to have a large influence on the fluid outlet temperature (figure 9.1). This is in accordance with the expected result. The wall temperature was set to a fixed value and the low fluid velocity does not decrease the surface heat transfer coefficient in a significant way (figure 9.4). However, equation 4.1 still needs to be satisfied, which therefore leads to an increase of T_{out} when the mean fluid velocity is decreased. This increase in outlet temperature with decreasing \bar{u} -values, leads to the large amount of heat that is transferred per unit mass at low fluid velocities, as it was observed in figure 9.2. Thus, the amount of water that is made use of in an effective way at low fluid velocities.

14.2 Influence of the plate distance

In section ?? a large drop of the outlet temperature with increasing plate distances and a peak of the heat transfer rate at a plate distance of 1,3 mm was observed. This can be explained by the shape of the laminar flow profile. Even though the inlet velocity was kept constant during the plate distance sweep, the velocity close to the wall did not stay constant. This is due to the fact that the laminar flow profile, with an approximately quadratic shape, did not change its shape when the value of d was changed. With a constant mean velocity, the velocity of the flow close to the wall therefore increased with decreasing plate distances. Based on this increase in velocity, the heat transfer coefficient increased with decreasing values of d . This relation can also be seen from equation 5.3.

An increase of T_{out} , however, leads in turn to a decrease of $LMTD$. Consequently \dot{Q} reached a maximum value at a plate distance of 1,3 mm and decreased when the plate distance was further decreased. Due to this correlation of the velocity close to the wall and T_{out} , the amount of heat removed per unit mass of water decreased with increasing plate distances (figure 9.6).

14.3 Influence of the heated plate length

A parameter-sweep of the heated plate length showed to have a significant influence on the average Nusselt number. This effect can be explained by the average thickness of the thermal boundary layer (see section 3.3). The thermal boundary layer starts to develop at the point (in flow direction) at which the heating begins and increases in thickness in flow direction. At short plate lengths the average thermal boundary thickness will therefore be very small, leading to a high surface heat transfer coefficient and average Nusselt number.

On the other hand the heated plate area increases linearly when L is prolonged. Thus, the outlet temperature as well as the heat transfer rate increase when the heated plate is chosen longer. Since T_{out} will converge closer to the wall temperature the longer the heated plate is, leading to a declination of $LMTD$. Consequently, T_{out} and \dot{Q} will reach a maximum value if the plate length is chosen to be very long.

15 | 2D Heat transfer simulation

The numerical simulation and the analytical model are in good accordance. This is especially true for velocities below 0,35 m/s. In this velocity region it is hard to tell the difference of the analytical solution and the numerical one from figure 10.1. The small deviation between the compared solutions at higher velocities might be explained by the higher Reynolds number of about 2064 at $\bar{u} = 0,5$ m/s. At a Reynolds number of approximately 2300 the transition to turbulent flow begins, which also marks the upper limit of the validity range of the analytical model.

16 | Experiment

For being able to evaluate the outcome of the investigation which influence a nonuniform flow distribution has, the results for this setup are compared to the measurement results that were obtained for a uniform flow across the entire coil element with a similar input current. From Table 12.2 in section 12.0.2 it can be seen that for a uniform flow, a gap width of 2 mm a flow rate of 158 g/min and an input current of 80,6 A, T_c converged to a temperature of 35,9°C. By comparing these results with the ones of the investigated case, it can be obtained that the temperature of the coil element was significantly higher when one side of the gap entrance was blocked than for a uniform flow. This was the case even though the mass flow rate was almost five-fold compared to the uniform flow case. Which final temperature level T_c might have converged to in the studied case is, however, not known since the experiment was aborted to prevent damages on the experimental setup. Similar results were observed when the part of the coil element close to the inlet flipped up slightly. Through this the coil element was not in line with the surface of the surrounding geometry which led to a changed flow through the geometry.

17 | Comparison of experimental and simulation results

For both gap widths that were studied (2 mm and 4 mm) the value of $\bar{\alpha}$ increased with increasing mass flow rates. This correlation between the mass flow rate and the average surface heat transfer coefficient was expected since an increase of the mass flow rate leads to an increase of the average fluid velocity across the heated area. The increased velocity in turn decreases the hydraulic boundary layer thickness, resulting in a thinner thermal boundary layer. With a thinner thermal boundary layer the temperature gradient is increased which leads to an increase of the average surface heat transfer coefficient¹.

With a maximal deviation of 2,1 % between the simulated $\bar{\alpha}$ -values and the ones obtained from measurements during the experiment with a gap width of 2 mm, the results showed to be in good accordance at flow rates between approximately 145 g/min and 302 g/min. Also the results from the simulation and experiment with a gap width of 4 mm deviated only slightly from each other with a maximal deviation of 2,3 %. However, the $\bar{\alpha}$ -value measured for a flow rate of approximately 560 g/min was 6 % higher compared to the one that was simulated. A possible explanation for this deviation might be the fact that all surfaces were assumed to be perfectly smooth in the simulation model. In the experimental setup this was however not the case. The slight surface roughness of the coil element, silicone and POM did not influence the flow characteristics at lower flow rates, but might have caused small local turbulences at a flow rate of 560 g/min. These turbulences might have led to an increase of the average surface heat transfer coefficient and consequently caused the deviation between the simulated and measured value.

As it can be seen from Figure 12.2 this increased deviation between the measured and simulated value was not obtained for higher flow rates using a gap width of 4 mm. Most likely, the lower fluid velocities that resulted from the larger gap width was the reason for this. By increasing the gap width by a factor of two, the average fluid velocity in the geometry was lowered by 50 %. Since the hydraulic diameter was also doubled by doubling

¹The theoretical background of the connection between the average surface heat transfer coefficient and the thermal boundary layer is given in the theory chapter.

the gap width, the value of the Reynolds number (equation 3.3) was not influenced by this change. Therefore, it was less likely that turbulences were induced by the surface roughness.

By an observation of the results plotted in Figure 12.1 the relatively high $\bar{\alpha}$ -value that was measured and calculated to approximately $1950 \text{ W/m}^2 \text{ K}$ for a flow rate of $\approx 171 \text{ g/min}$ attracts attention. Also the fact that the average surface heat transfer coefficient was calculated to approximately the same value of approximately $1730 \text{ W/m}^2 \text{ K}$ for the flow rates of 146 g/min and 160 g/min seems surprising.

To find a possible reason for this, a closer look was taken on the temperatures that were obtained from the simulation results for the temperature of the coil element and water. An overview of the temperatures that were considered for this is given in Table 17.1. The value of the mean water temperature \bar{T}_w was calculated with the following formula.

$$\bar{T}_w = \frac{T_{in} + T_{out}}{2} \quad (17.1)$$

Table 17.1: Simulated coil element and water temperatures for different flow rates.

Flow rate g/min	T_{in} °C	T_{out} °C	T_c °C	\bar{T}_w °C	$T_c - \bar{T}_w$ °C
171	22.0	32.9	56.8	27.4	29.3
146	19.5	25.8	39.2	22.7	16.6
160	23.8	26.9	34.3	25.3	8.9
190	22.7	26.8	37.3	24.7	12.6

From the values of the average temperature difference between water and coil element ($T_c - \bar{T}_w$) listed in Table 17.1, it can be seen that this value was calculated to be higher for the two flow rates of 146 g/min and 171 g/min than the one calculated for 160 g/min and 190 g/min . Considering the fact that the coil element was embedded into the lower part of the geometry, the relatively high $\bar{\alpha}$ -values that were obtained at flow rates of 146 g/min and 171 g/min , when compared to the ones obtained at flow rates of 160 g/min and 190 g/min , might be explained by the influence of natural convection. This reasoning seems logical since the $\bar{\alpha}$ was simulated for relatively low flow rates and consequently low fluid velocities. The low fluid velocity leads to that the share of $\bar{\alpha}$ caused by natural convection is not negligibly small compared to the share resulting from forced convection.

Thus, the difference between the average coil element temperature and average water temperatures, which were almost twofold for a flow rate of 146 g/min and more than threefold at a flow rate of 171 g/min when compared to the value calculated for a flow rate of 160 g/min , might have been the reason for the relatively high value of $\bar{\alpha}$ calculated for these flow rates.

With an estimated measurement uncertainty reaching from 0,04 °C to 0,11 °C for a gap width of 2 mm and from 0,04 °C to 0,06 °C for a gap width of 4 mm, the measurement of the average coil element temperature can be considered to be rather accurate. The overall measurement uncertainty of the obtained $\bar{\alpha}$ -values in positive direction was below 4,3 % for all measurements taken at a gap width of 2 mm, which seems fairly small, considering the number of variables this value was based on. For a gap width of 4 mm, the measurement uncertainty of $\bar{\alpha}$ in positive direction decreased with increasing current densities in the coil element with a maximum value of 7,1 % with a total current of 50,1 A. The reason for the measurement uncertainties being larger for a gap width of 4 mm than the ones at a gap width of 2 mm was that the measurement uncertainty of the water temperature after the heated area (T_m) increased with increasing gap widths which increased the measurement uncertainty of the logarithmic temperature difference. This result shows that even though the temperature difference of the water across the gap width (from bottom to top) was identified as possible source of error and considered in the design of the experimental geometry, the water temperature level at the position of thermocouples 1-5 was not all steady. Although the uncertainty of $LMTD$ increased with the flow rate, the uncertainty of $\bar{\alpha}$ in positive direction decreased with increasing flow rates. The reason for this was that also the current was increased at the same time, which led to higher values of \dot{Q} and therefore lower relative uncertainties of $\bar{\alpha}$.

Due to the same reason as described above, the measurement uncertainty in negative direction increased also with an increase of the gap width. The uncertainty in negative direction were however larger than the ones in positive direction due to the heat losses to the surrounding which were described in section 7.9.2.

18 | Simulation

The results which were presented in chapter 13, showed that the calculated values of $\bar{\alpha}$ were significantly higher than the ones calculated for $\bar{\alpha}_{T_s}$. Based on the approximation that had to be made in order to calculate the average heat transfer coefficient despite the fact that the average surface temperature of the heated area within the area of interest could not be measured in the experiment, a deviation of the obtained results of $\bar{\alpha}$ and $\bar{\alpha}_{T_s}$ was expected. However, these deviation did not limit the comparability of the simulated and measured results (presented and discussed in chapter 12 and 17). Due to the relatively large deviations between the two values, it has to be pointed out that $\bar{\alpha}_{T_s}$ is a more accurate measure for the average surface heat transfer coefficient. Therefore, this value should be taken if further developments are based on the presented results.

The decrease of the fraction of heat that was transferred from the surface of the silicone into the water, compared to the amount of heat that was transferred from the aluminum (coil element) surface ($\dot{Q}_{si}/\dot{Q}_{al}$) with increasing mass flow rates, can be explained by the low thermal conductivity of silicone. As it was obtained from the results of the analytical model as well as the simulated values and measured values for the experimental geometry, an increase of the mass flow rate leads to an increase of the average surface heat transfer coefficient¹. However, the amount of heat that is transferred to the water from the silicone surface has to be transported from the coil element to the silicone surface by conduction first. Since the thermal conductivity of the used silicone was relatively low with a value of approximately $0,17 \text{ W/mK}$, the amount of heat that could be transferred to the water from the silicone surface was limited. With a value of 138 W/mK , the thermal conductivity of the coil element was more than 800 times higher than the one of silicone. Due to this, the amount of heat that was transferred to the water from the surface of the coil element, was not limited in a way as it was the case for silicone. Consequently, the value of the fraction $\dot{Q}_{si}/\dot{Q}_{al}$ decreased with increasing mass flow rates.

Since a larger gap width led to a lower fluid velocity close to the heat transfer surface, the heat transfer coefficients for a gap width of 4 mm were lower than the ones which were obtained for a gap width of 2 mm. As a consequence of this, the heat could not be

¹An explanation for this connection is given in chapter 17

removed from the coil element as effectively for a gap width of 4 mm, which led to an increase of the coil element temperature. This in turn led to an increase of the conductive heat transfer in the silicone, which is why a larger fraction of the heat could be transferred into the water through the silicone surface when the gap width was increased.

Since an increase of the current density leads to increased resistive losses in the coil element, a larger amount of heat was generated per unit area when the current was set to higher values. Due to this, the temperature gradient between the aluminum and silicone raised. Consequently, the conductive heat transfer into the silicone was increased and therefore higher values for the fraction of $\bar{\alpha}/\bar{\alpha}_{T_s}$ were obtained for higher current densities.

An increase of \dot{Q}_{cond} was observed for higher temperature levels in the coil element. This is in accordance with the expected result, as the increase of T_c led to a larger temperature gradient between the coil element and the surrounding material and consequently a larger amount of heat which was transferred into the surrounding material by conductive heat transfer.

Based on the small deviations between the aluminum surface temperature and T_c , it was shown that the difference in temperature between the non-cooled side and the cooled side of the coil element were relatively small. Additionally, this results showed that the calculation method of T_c , which is described in section 7.3.2, was fairly accurate.

Part V

Conclusions

19 | Experiment

From the results that resulted from the experiment in which the influence of a nonuniform flow across the coil element was investigated, it can be concluded that a uniform flow across the entire coil element is of great importance to the performance of the cooling system. This might not lead to larger problems when the motor is rotating since the velocity of the rotor will add a second flow direction and therefore lead to that water will most likely flow across the entire stator surface. However, when the motor is standing still and the flow is not distributed evenly across the stator surface based on the way of how the fluid enters the motor, this might lead to very high coil temperatures. Consequently this outcome has to be considered in the final design of the cooling system.

In the experiment that was investigating the maximum cooling capacity of the system, the input current was set to 195 A. With a minimum cross-section area (above the thermocouples 10 and 11) of $1,5 \text{ mm} \cdot 3 \text{ mm} = 4,5 \text{ mm}^2$ and a maximum cross-section of $5 \text{ mm} \cdot 3 \text{ mm} = 15 \text{ mm}^2$, this corresponded to a maximum and minimum current density in the coil element of approximately $43,3 \text{ A/mm}^2$ and 13 A/mm^2 . In the motor, however, current densities of maximum 10 A/mm^2 will be reached as higher current densities would lead to very large resistive losses [15]. One of the demands that was set for the cooling system was that the cooling system should keep the coil temperature below 90°C at all times. Since the temperature level in the coil did not exceed approximately 52°C , although the maximum current density was more than 4-fold compared to the one that will probably be reached in the motor, it can be concluded that the cooling system fulfills this demand. Furthermore, the electrical conductivity of the coil element was significantly lower than the coil material that will be used in the final motor layout. Due to this, the resistive losses in the coil element were larger than the ones that can be expected in the coil of the motor. Thus, the temperature of the motor coil would most likely have been lower when the same current density and parameters of the cooling system would have been applied.

As it was expected due to the results from the analytical model, a gap width of 2 mm resulted in higher values of the average surface heat transfer coefficient. When the same flow rate was applied, the measured values of $\bar{\alpha}$ were higher by a factor of up to 1,8 when the gap width was set to 2 mm compared to the ones that were obtained with a gap width

of 4 mm.

A comparison of the simulation results with the measurements from the experiment, showed that the results were in good accordance with a maximal deviation of 2,1% and 2,3% for the studied cases using a gap width of 2 mm and 4 mm, respectively. A larger deviation of the results of 6,0% was, however, obtained at a flow rate of approximately 560 g/min and a gap width of 2 mm. This deviation was probably caused by turbulences which were induced by small unevenesses of the surfaces of the experimental geometry. Therefore, it can be concluded that the heat transfer experiment that was developed in throughout this thesis performed very well. As an additional outcome, natural convection seems to add to the heat transfer coefficient with a non-neglectable amount at low flow rates.

20 | Simulation

From the simulation results of the setup that was used in the heat transfer experiment, it can be concluded that a heat transfer coefficient of approximately $2160 \text{ W/m}^2\text{K}$ can be achieved when water is flowing through a 2 mm air gap between the stator and rotor with an average fluid velocity of approximately $0,055 \text{ m/s}$. When the fluid flows through the air gap with an average velocity of approximately $0,0156 \text{ m/s}$, an average surface heat transfer coefficient of roughly $1400 \text{ W/m}^2\text{K}$ can be expected¹. With these average heat transfer coefficients, the demand on the cooling system to offer a cooling capacity of approximately 40 kW/m^2 can be fulfilled with a logarithmic mean temperature difference of approximately $18,5 \text{ }^\circ\text{C}$ when the higher average fluid velocity is applied and $29 \text{ }^\circ\text{C}$ when the fluid is flowing with the lower average fluid velocity.

Although the silicone covered a share of approximately 45 % of the heat transfer area within the region of interest, only a share between 17 % and 13 % of the heat was transferred into the water through the silicone surface. Due to the fact that a material with a very low thermal conductivity was chosen as filling material in the coil element, in order to model the “worst case szenario“ in the experiment, this outcome was expected. However, the results indicate that the cooling performance of the system could be improved significantly by considering the thermal conductivity when the material of the lamination steel is chosen for the final motor layout.

¹These values were based on the obtained values of $\bar{\alpha}_{T_s}$. The average fluid velocity was evaluated at the middle of the coil element in radial direction ($r=122,5 \text{ mm}$ in Figure 7.6).

21 | Overall outcome of the thesis

The key design parameters for the cooling system were identified by an analytical model of the heat transfer problem. Their influence on the performance of the system were studied in detail by parameters-sweeps. Through a comparison of the analytical model with the results from numerical simulations (2D) for the same setup, it was shown that the obtained results were in good accordance.

The main content of the thesis was, however, the development of an experimental model with which the cooling performance of the system was experimentally investigated. The experimental results were subsequently compared with the ones that were simulated with the 3D-simulation model that was created. Due to the fact that the deviations between the results were marginal and the influence of the parameters that were used in the simulation were studied thoroughly, the obtained results can be expected to be rather accurate and fairly reliable.

Based on the fact that both numerical simulation setups were modeling the heat transfer problem using the same physical models and showed good accordance to the corresponding analytical and experimental results, it can be expected that also the results of the 2D-simulation model deliver relatively accurate results for the average surface heat transfer coefficient. This is an important outcome since the fine mesh that was used in the 3D-model led to high computational costs. Each simulation that was carried out for the developed 3D-simulation took about 3 hours to be solved, although a computer with a very high computational power with 32 cores and a main memory of 32 GB was used. Since the computation of the fluid flow is the reason for this long solving time, the calculation of the average surface heat transfer coefficient using a 2D-simulation model or the analytical model and including the obtained values into the simulation used to investigate the electrical performance of the machine, would lead to large time savings. However, the measurement results indicated that the uniformity of the flow across the entire stator surface is of great importance for the resulting temperature level in the coil. Therefore, the flow path of the fluid in the final motor design should ensure a uniform flow and should be designed carefully.

Based on the obtained results, the gap of the fluid path for the presented cooling

system should be set to the lowest possible value. However, this parameter should be chosen in consideration of the temperature limitations of the stator, the length of the area that is to be cooled in coolant flow direction and the required mass flow rate.

As a final outcome it can be concluded that the all demands that were set for the cooling system are fulfilled by the presented system.

22 | Recommendations for future work

In conclusion of the presented thesis the following recommendations are given for the final development and implementation of the cooling system:

- Creating a 2D or 3D simulation model to finalize the layout of the cooling system in respect to the final motor design. This model should include the possibility to study the influence of rotation on the cooling performance.
- A final decision on the cooling fluid should be made in consideration of the application of the motor. For this decision the possibility of improving the cooling performance by the use of nanofluids should be considered [17].
- The cooling system should be included in the final motor design with special focus on the creation of a homogenous flow across the entire stator surface since this was identified to be a critical parameter.

Bibliography

- [1] Aalco Metals Ltd. Aluminium alloy 5052 - h32. <http://www.aalco.co.uk>, Sep. 2011. Retrieved: 10 Dez. 2012.
- [2] G. Airoidi, G. Ingram, K. Mahkamov, J. Bumby, R. Dominy, N. Brown, A. Mebarki, and M. Shanel. Computations on heat transfer in axial flux permanent magnet machines. In *Electrical Machines, 2008. ICEM 2008. 18th International Conference on*, pages 1–6, 2008.
- [3] Akzo Nobel Coatings AS. Data sheet casco glass silikon 2985/3985. <http://www.casco.no>, Mar. 2012. Retrieved: 25 April 2013.
- [4] A. Boglietti. Guest editorial. *IEEE Transactions on Industrial Electronics*, 55(10):3498–3499, 2008.
- [5] R. Camilleri, T. Woolmer, A. Court, and M. D. McCulloch. Investigation into the temperature profile of a liquid cooled yasa x00a9; afpm machine. In *Power Electronics, Machines and Drives (PEMD 2012), 6th IET International Conference on*, pages 1 –8, march 2012.
- [6] F. Caricchi, F. Crescimbinì, and O. Honrati. Modular axial-flux permanent-magnet motor for ship propulsion drives. *IEEE Transactions on Energy Conversion*, 14(3):673–679, 1999.
- [7] F. Caricchi, F. Crescimbinì, F. Mezzetti, and E. Santini. Multistage axial-flux pm machine for wheel direct drive. *IEEE Transactions on Industry Applications*, 32:882–888, 1996.
- [8] Fritz Bossert e.K. Technisches datenblatt as1745g. <http://www.bossert-hamburg.de>, Jul. 2012. Retrieved: 22 April 2013.
- [9] Fritz Bossert e.K. Technisches datenblatt silcoset 151. <http://www.bossert-hamburg.de>, Feb. 2013. Retrieved: 22 April 2013.

- [10] J. Holman. *Heat transfer*. Number 9th ed. McGraw-Hill, New York, 2002.
- [11] W. Hufschmidt and E. Burck. Der einfluss temperaturabhängiger stoffwerte auf den wärmeübergang bei turbulenter strömung von flüssigkeiten in rohren bei hohen wärmestromdichten und prandtlzahlen. *International Journal of Heat and Mass Transfer*, 11(6):1041–1048, June 1968.
- [12] C. Hwang and J. Chang. Design and analysis of a high power density and high efficiency permanent magnet dc motor. *Journal of Magnetism and Magnetic Materials*, 209(1–3):234–236, Feb. 2000.
- [13] V. Ingenieure, V. Chemieingenieurwesen, and G. u. *VDI-Wärmeatlas. Buch-Version.: Berechnungsblätter für den Wärmeübergang*. Springer-Verlag GmbH, 9th edition, 2002.
- [14] C. Lim, G. Airoidi, J. Bumby, R. Dominy, G. Ingram, K. Mahkamov, N. Brown, A. Mebarki, and M. Shanel. Experimental and cfd investigation of a lumped parameter thermal model of a single-sided, slotted axial flux generator. *International Journal of Thermal Sciences*, 49(9):1732–1741, Sept. 2010.
- [15] S. Lomheim. Investigation of a novel coil design suited for axial flux permanent magnet machines. Master’s thesis, Norwegian University of Science and Technology, Department of Electrical Power Engineering, 2013.
- [16] F. Marignetti, V. Delli Colli, and Y. Coia. Design of axial flux pm synchronous machines through 3-d coupled electromagnetic thermal and fluid-dynamical finite-element analysis. *Industrial Electronics, IEEE Transactions on*, 55(10):3591–3601, 2008.
- [17] C. T. Nguyen, G. Roy, C. Gauthier, and N. Galanis. Heat transfer enhancement using al₂o₃-water nanofluid for an electronic liquid cooling system. *Applied Thermal Engineering*, 27(8–9):1501 – 1506, 2007.
- [18] B. Palm. *Short notes on Heat Transfer and heat exchangers*. KTH Royal Institute of Technology, Kungl Tekniska Högskolan, SE-100 44 STOCKHOLM, 1st edition, Aug. 2011.
- [19] Röchling Sustaplast KG. Technical data sheet - sustarin c. <http://www.roechling.com>, March 2012. Retrieved: 14 April 2013.
- [20] S. Scowby, R. Dobson, and M. Kamper. Thermal modelling of an axial flux permanent magnet machine. *Applied Thermal Engineering*, 24(2–3):193–207, Feb. 2004.

- [21] R.-J. Wang, M. Kamper, and R. Dobson. Development of a thermofluid model for axial field permanent-magnet machines. *Energy Conversion, IEEE Transactions on*, 20(1):80 – 87, march 2005.
- [22] F. M. White. *Fluid mechanics*. WCB/McGraw-Hill, Boston, 4th edition, 1999.
- [23] P. Zheng, X. Gan, and L. Li. Analysis and design of a high power density axial flux permanent magnet linear synchronous machine used for stirling system. In *Proceedings of the 2010 First International Conference on Pervasive Computing, Signal Processing and Applications, PCSPA '10*, pages 398–401, Washington, DC, USA, 2010. IEEE Computer Society.

Appendices

A |

A.1 Risk-report



Risikovurderingsrapport

Vannkjølt, strømførende spole-element

Prosjekttittel	Vannkjøling av et strømførende spole-element
Apparatur	Vannkjølt strømførende spole-element
Enhet	NTNU
Apparaturansvarlig	Trygve Magne Eikevik
Prosjektleder	Trygve Magne Eikevik
HMS-koordinator	Morten Grønli
HMS-ansvarlig (linjeleder)	Olav Bolland
Plassering	VVSLab
Romnummer	C163
Risikovurdering utført av	Lars Clad og Sigbjørn Lomheim i samarbeid med Håvard Rekstad

Godkjenning:

	Navn	Dato	Signatur
Prosjektleder	Trygve Magne Eikevik	3/5-2013	
HMS koordinator	Morten Grønli	3/5 2013	
HMS ansvarlig (linjeleder)	Olav Bolland	3/5 2013	

INNHOLDSFORTEGNELSE

1	INNLEDNING	1
2	KONKLUSJON	1
3	ORGANISERING.....	1
4	RISIKOSTYRING AV PROSJEKTET	1
5	TEGNINGER, FOTO, BESKRIVELSER AV FORSØKSOPPSETT	2
6	EVAKUERING FRA FORSØKSOPPSETNINGEN.....	2
7	VARSLING.....	2
7.1	Før forsøkskjøring.....	2
7.2	Ved uønskede hendelser	3
8	VURDERING AV TEKNISK SIKKERHET	3
8.1	Fareidentifikasjon, HAZOP.....	3
8.2	Brannfarlig, reaksjonsfarlig og trykksatt stoff og gass	4
8.3	Trykkpåkjent utstyr	4
8.4	Påvirkning av ytre miljø (utslipp til luft/vann, støy, temperatur, rystelser, lukt)	4
8.5	Stråling.....	4
8.6	Bruk og behandling av kjemikalier	4
8.7	El sikkerhet (behov for å avvike fra gjeldende forskrifter og normer).....	4
9	VURDERING AV OPERASJONELL SIKKERHET.....	5
9.1	Prosedyre HAZOP	5
9.2	Drifts og nødstopps prosedyre	5
9.3	Opplæring av operatører.....	5
9.4	Tekniske modifikasjoner.....	5
9.5	Personlig verneutstyr	5
9.6	Generelt.....	5
9.7	Sikkerhetsutrustning	5
9.8	Spesielle tiltak.....	5
10	TALLFESTING AV RESTRISIKO – RISIKOMATRISSE	6
11	LOVER FORSKRIFTER OG PÅLEGG SOM GJELDER.....	7
12	DOKUMENTASJON.....	7
13	VEILEDNING TIL RAPPORTMAL.....	8

1 INNLEDNING

Formålet med eksperimentet er å måle det gjennomsnittlige varmeovergangstallet mellom kjølevæske (vann) og et strømførende spole-element for forskjellige vannhastigheter og varierende strømtettheter i spole-elementet. Forsøksoppsetningen er vist skjematisk i figur 1 i vedlegg A.

Plassering: VVSLab, rom C163

2 KONKLUSJON

Riggen er bygget til god laboratorium praksis (GLP).

Apparaturkortet får en gyldighet på **8 måneder**
Forsøk pågår kort får en gyldighet på **8 måneder**

3 ORGANISERING

Rolle	NTNU
Prosjektleder	Trygve Magne Eikevik
Apparaturansvarlig	
Romansvarlig	
HMS koordinator	Morten Grønli
HMS ansvarlig (linjeleder):	Olav Bolland

4 RISIKOSTYRING AV PROSJEKTET

Hovedaktiviteter risikostyring	Nødvendige tiltak, dokumentasjon	DTG
Prosjekt initiering	Prosjekt initiering mal	
Veiledningsmøte	Skjema for Veiledningsmøte med pre-risikovurdering	
Innledende risikovurdering	Fareidentifikasjon – HAZID Skjema grovanalyse	
Vurdering av teknisk sikkerhet	Prosess-HAZOP Tekniske dokumentasjoner	
Vurdering av operasjonell sikkerhet	Prosedyre-HAZOP Opplæringsplan for operatører	
Sluttvurdering, kvalitetssikring	Uavhengig kontroll Utstedelse av apparaturkort Utstedelse av forsøk pågår kort	



5 TEGNINGER, FOTO, BESKRIVELSER AV FORSØKSOPPSETT

Forsøksoppsettningen er vist skjematisk i figur 1 i vedlegg A.

Ved utføring av eksperimentet blir vann-massestrømmen, bredden på den vannførende spalten og strømtettheten i spole-elementet variert. Det resulterende gjennomsnittlige varmeovergangstallet blir målt indirekte ved å måle temperaturforskjellen på vannet mellom inn- og utløpet, måle temperaturen på spole elementet og styring av massestrømmen med en vannpumpe.

Forsøksoppsettet er laget av POM og to forskjellige spole-elementer laget av aluminium og kobber kommer til å bli testet. Forsøket blir kjørt med en relativ lav spenning på (1-5 V) og en høy strømstyrke på (50-100 A). Vann-massestrømmen blir variert mellom 0,3 og 2,1 L/min. Temperaturen på spole-elementet er begrenset til 160°C siden dette er den maksimale temperaturen som POMen tåler. Selve forsøksoppsettet er vanntett og forskjellen på vanntrykket mellom inn- og utløp kommer til å være relativt lavt (under 1 bar). Elektrisk utstyr (data-logger, strømforsyning, PC osv.) skal befinde seg i god avstand til forsøket eller i en vanntett boks.

Operatøren oppholder seg i nærheten av eksperimentet med stadig adgang til brytern til strømforsyningen til spole-elementet og vannpumpen.

Prosess og Instrumenterings Diagram finnes i vedlegg A.

6 EVAKUERING FRA FORSØKSOPPSETNINGEN

Evakuering skjer på signal fra alarmklokker eller lokale gassalarmstasjon med egen lokal varsling med lyd og lys utenfor aktuelle rom, se 6.2

Evakuering fra rigg området foregår igjennom merkede nødutganger til møteplass, (hjørnet gamle kjemi/kjelhuset eller parkeringsplass 1a-b.)

Aksjon på rigg ved evakuering: Før området forlates, skal strømforsyningen til spole-elementet og vannpumpen bli slått av.

7 VARSLING

7.1 Før forsøkskjøring

Varsling per e-post, til Liste iept-experiments@ivt.ntnu.no

I e-posten skal det stå::

- Navn på forsøksleder:
- Navn på forsøksrigg:
- Tid for start: (dato og klokkeslett)
- Tid for stop: (dato og klokkeslett)

All forsøkskjøringen skal planlegges og legges inn i aktivitetskalender for lab. Forsøksleder må få bekrefteelse på at forsøkene er klarert med øvrig labdrift før forsøk kan iverksettes.

7.2 Ved uønskede hendelser

BRANN

Ved brann en ikke selv er i stand til å slukke med rimelige lokalt tilgjengelige slukkemidler, skal nærmeste brannalarm utløses og arealet evakueres raskest mulig. En skal så være tilgjengelig for brannvesen/bygningsvaktmester for å påvise brannsted.

Om mulig varsles så:

NTNU	SINTEF
Morten Grønli, Mob: 918 97 515	Harald Mæhlum, Mob: 930 14 986
Olav Bolland: Mob: 918 97 209	Anne Karin T. Hemmingsen Mob: 930 19 669
NTNU – SINTEF Beredskapstelefon	800 80 388

GASSALARM

Ved gassalarm skal gassflasker stenges umiddelbart og området ventileres. Klarer man ikke innen rimelig tid å få ned nivået på gasskonsentrasjonen så utløses brannalarm og laben evakueres. Dedikert personell og eller brannvesen sjekker så lekkasjested for å fastslå om det er mulig å tette lekkasje og lufte ut området på en forsvarlig måte.

Varslingsrekkefølge som i overstående punkt.

PERSONSKADE

- Førstehjelpsutstyr i Brann/førstehjelpsstasjoner,
- Rop på hjelp,
- Start livreddende førstehjelp
- **Ring 113** hvis det er eller det er tvil om det er alvorlig skade.

ANDRE UØNSKEDE HENDELSER (AVVIK)

NTNU:

Rapportering av uønskede hendelser, Innsida, avviksmeldinger

<https://innsida.ntnu.no/wiki/-/wiki/Norsk/Melde+avvik>

SINTEF:

Synergi

8 VURDERING AV TEKNISK SIKKERHET

8.1 Fareidentifikasjon, HAZOP

Se kapittel 13 "Veiledning til rapport mal.

Forsøksoppsetningen deles inn i følgende noder:

Node 1	Vannkjølt, strømførende spole
Node 2	Spenningsforsyning, elektrisk anlegg

Vedlegg B: Hazop_mal

Vurdering: Sikkerhet ivaretatt

Når testen gjennomføres kan det komme til vannlekkasje. Hvis dette hender må strømforsyningen til spole-elementet og vannpumpen bli brudd for å stoppe og vannflyten oppvarming av spole-elementet. Under forsøket er det berøringsfare på spole-elementet på grunn av høy temperatur (max. 160°C) og dermed forbrenningsfare.



Når testen gjennomføres er det berøringsfare på kabelskoene mellom spoleelement og kabler, men siden spenningen er lav er det ikke krav om berøringsikkerhet. I tillegg er det et galvanisk skille mellom spenningskilden og testen, og det kreves da to jordingspunkter før det blir fare for strømgjennomgang. Under endring/justering av forsøket blir spenningskilden koblet fra nettet med synlig brudd, for å sikre at det ikke er spenningsatt.

8.2 Brannfarlig, reaksjonsfarlig og trykksatt stoff og gass

NEI	
-----	--

8.3 Trykkpåkjent utstyr

Inneholder forsøksoppsetningen trykkpåkjent utstyr:

NEI	
-----	--

8.4 Påvirkning av ytre miljø (utslipp til luft/vann, støy, temperatur, rystelser, lukt)

NEI	
-----	--

8.5 Stråling

NEI	
-----	--

8.6 Bruk og behandling av kjemikalier

NEI	
-----	--

8.7 El sikkerhet (behov for å avvike fra gjeldende forskrifter og normer)

NEI	
-----	--

I dette forsøket blir montasje og bruk utført i forhold til normer og forskrifter med tanke på berøringsfare.

Vurdering:

I testen brukes transformator som kortsluttes over spole-elementet. Høyspenningssiden er berørings sikker og opererer på 220 V. Lavspenningssiden er ikke berørings sikkert, men spenningsnivået er under 50V og kan dermed regnes som et lavspenningsforsøk. Det er ikke krav om berøringsikkerhet for lavspenningsanlegg.

9 VURDERING AV OPERASJONELL SIKKERHET

Sikrer at etablerte prosedyrer dekker alle identifiserte risikoforhold som må håndteres gjennom operasjonelle barrierer og at operatører og teknisk utførende har tilstrekkelig kompetanse.

9.1 Prosedyre HAZOP

Metoden er en undersøkelse av operasjonsprosedyrer, og identifiserer årsaker og farekilder for operasjonelle problemer.

Vedlegg: HAZOP_MAL_Pro prosedyre

Vurdering: Prosedyren er enkel. Det kan ikke oppstå varlige situasjoner selv om operatøren gjør noe feil. Derfor er skjemaet ikke fylt ut.

9.2 Drifts og nødstopps prosedyre

Se kapittel 13 "Veiledning til rapport mal."

Driftsprosedyren er en sjekklister som skal fylles ut for hvert forsøk.

Nødstopps prosedyren skal sette forsøksoppsettningen i en harmløs tilstand ved uforutsette hendelser.

Vedlegg: E Forsøksprosedyre

Nødstopps prosedyre: Bryte strømforsyningen til spole-elementet og vannpumpen.

9.3 Opplæring av operatører

Dokument som viser Opplæringsplan for operatører utarbeides for alle forsøksoppsettninger.

Vedlegg: F Opplæringsplan for operatører

9.4 Tekniske modifikasjoner

- Tekniske modifikasjoner som kan gjøres av Operatør:
Alle tekniske modifikasjoner kan gjøres av operatøren.
- Dersom strømforsyningen til spole-elementet blir endret (høyere spenning eller strømstyrke), må en ny risikovurdering utføres.

9.5 Personlig verneutstyr

9.6 Generelt

- *Vann og trykklufttilførsel i slanger skal stenges/kobles fra ved nærmeste fastpunkt når riggen ikke er i bruk.*

9.7 Sikkerhetsutrustning

- *Ikke nødvendig*

9.8 Spesielle tiltak



10 TALLFESTING AV RESTRISIKO – RISIKOMATRISE

Se kapittel 13 "Veiledning til rapport mal."

Risikomatrisen vil gi en visualisering og en samlet oversikt over aktivitetens risikoforhold slik at ledelse og brukere får et mest mulig komplett bilde av risikoforhold.

IDnr	Aktivitet-hendelse	Frekv-Sans	Kons	RV
1	Varmt spole-element, berøringsfare	3	B	B3
2	Vannlekkasje	3	A	A3
3	Fare for å snuble i utstyr	3	A	A3
4	Fare for strømgjennomgang	1	E	E1

Vurdering restrisiko: Restrisiko er akseptabel.

11 LOVER FORSKRIFTER OG PÅLEGG SOM GJELDER

Se <http://www.arbeidstilsynet.no/regelverk/index.html>

- Lov om tilsyn med elektriske anlegg og elektrisk utstyr (1929)
- Arbeidsmiljøloven
- Forskrift om systematisk helse-, miljø- og sikkerhetsarbeid (HMS Internkontrollforskrift)
- Forskrift om sikkerhet ved arbeid og drift av elektriske anlegg (FSE 2006)
- Forskrift om elektriske forsyningsanlegg (FEF 2006)
- Forskrift om utstyr og sikkerhetssystem til bruk i eksplosjonsfarlig område NEK 420
- Forskrift om håndtering av brannfarlig, reaksjonsfarlig og trykksatt stoff samt utstyr og anlegg som benyttes ved håndteringen
- Forskrift om Håndtering av eksplosjonsfarlig stoff
- Forskrift om bruk av arbeidsutstyr.
- Forskrift om Arbeidsplasser og arbeidslokaler
- Forskrift om Bruk av personlig verneutstyr på arbeidsplassen
- Forskrift om Helse og sikkerhet i eksplosjonsfarlige atmosfærer
- Forskrift om Høytrykksspyling
- Forskrift om Maskiner
- Forskrift om Sikkerhetsskiltning og signalgivning på arbeidsplassen
- Forskrift om Stillaser, stiger og arbeid på tak m.m.
- Forskrift om Sveising, termisk skjæring, termisk sprøyting, kullbuemeisling, lodding og sliping (varmt arbeid)
- Forskrift om Tekniske innretninger
- Forskrift om Tungt og ensformig arbeid
- Forskrift om Vern mot eksponering for kjemikalier på arbeidsplassen (Kjemikalieforskriften)
- Forskrift om Vern mot kunstig optisk stråling på arbeidsplassen
- Forskrift om Vern mot mekaniske vibrasjoner
- Forskrift om Vern mot støy på arbeidsplassen

Veiledninger fra arbeidstilsynet

se: <http://www.arbeidstilsynet.no/regelverk/veiledninger.html>

12 DOKUMENTASJON

- Tegninger, foto, beskrivelser av forsøksoppsetningen
- Hazop_mal
- Sertifikat for trykkpåkjent utstyr
- Håndtering avfall i NTNU
- Sikker bruk av LASERE, retningslinje
- HAZOP_MAL_Procedyre
- Forsøksprosedyre
- Opplæringsplan for operatører
- Skjema for sikker jobb analyse, (SJA)
- Apparaturløstet
- Forsøk pågår kort

13 VEILEDNING TIL RAPPORTMAL

Kapittel 7 Vurdering av teknisk sikkerhet

Sikre at design av apparatur er optimalisert i forhold til teknisk sikkerhet.

Identifisere risikoforhold knyttet til valgt design, og eventuelt å initiere re-design for å sikre at størst mulig andel av risiko elimineres gjennom teknisk sikkerhet.

Punktene skal beskrive hva forsøksoppsetningen faktisk er i stand til å tåle og aksept for utslipp.

7.1 Fareidentifikasjon, HAZOP

Forsøksoppsetningen deles inn i noder: (eks *Motorenhet, pumpeenhet, kjøleenhet.*)

Ved hjelp av ledeord identifiseres årsak, konsekvens og sikkerhetstiltak. Konkluderes det med at tiltak er nødvendig anbefales disse på bakgrunn av dette. Tiltakene lukkes når de er utført og Hazop sluttføres.

(eks *"No flow"*, årsak: *rør er deformert*, konsekvens: *pumpe går varm*, sikkerhetsforanstaltning: *måling av flow med kobling opp mot nødstoppe eller hvis konsekvensen ikke er kritisk benyttes manuell overvåkning og punktet legges inn i den operasjonelle prosedyren.*)

7.2 Brannfarlig, reaksjonsfarlig og trykksatt stoff.

I henhold til Forskrift om håndtering av brannfarlig, reaksjonsfarlig og trykksatt stoff samt utstyr og anlegg som benyttes ved håndteringen

Brannfarlig stoff: Fast, flytende eller gassformig stoff, stoffblanding, samt stoff som forekommer i kombinasjoner av slike tilstander, som i kraft av sitt flammepunkt, kontakt med andre stoffer, trykk, temperatur eller andre kjemiske egenskaper representerer en fare for brann.

Reaksjonsfarlig stoff: Fast, flytende, eller gassformig stoff, stoffblanding, samt stoff som forekommer i kombinasjoner av slike tilstander, som ved kontakt med vann, ved sitt trykk, temperatur eller andre kjemiske forhold, representerer en fare for farlig reaksjon, eksplosjon eller utslipp av farlig gass, damp, støv eller tåke.

Trykksatt stoff: Annet fast, flytende eller gassformig stoff eller stoffblanding enn brann- eller reaksjonsfarlig stoff, som er under trykk, og som derved kan representere en fare ved ukontrollert utslipp.

Nærmere kriterier for klassifisering av brannfarlig, reaksjonsfarlig og trykksatt stoff er fastsatt i vedlegg 1 i veiledningen til forskriften "Brannfarlig, reaksjonsfarlig og trykksatt stoff"

<http://www.dsb.no/Global/Publikasjoner/2009/Veiledning/Generell%20veiledning.pdf>

http://www.dsb.no/Global/Publikasjoner/2010/Tema/Temaveiledning_bruk_av_farlig_stoff_Del_1.pdf

Rigg og areal skal gjennomgås med hensyn på vurdering av Ex sone

- Sone 0: Alltid eksplosiv atmosfære, for eksempel inne i tanker med gass, brennbar væske.
- Sone 1: Primær sone, tidvis eksplosiv atmosfære for eksempel et fyllingstappestpunkt

- Sone 2: Sekundert utslippssted, kan få eksplosiv atmosfære ved uhell, for eksempel ved flenser, ventiler og koblingspunkt

7.4 Påvirkning av ytre miljø

Med forurensning forstås: tilførsel av fast stoff, væske eller gass til luft, vann eller i grunnen støy og rystelser påvirkning av temperaturen som er eller kan være til skade eller ulempe for miljøet.

Regelverk: <http://www.lovddata.no/all/hl-19810313-006.html#6>

NTNU retningslinjer for avfall se: <http://www.ntnu.no/hms/retningslinjer/HMSR18B.pdf>

7.5 Stråling

Stråling defineres som

Ioniserende stråling: Elektromagnetisk stråling (i strålevernssammenheng med bølgelengde <100 nm) eller hurtige atomære partikler (f.eks alfa- og beta-partikler) som har evne til å ionisere atomer eller molekyler
Ikke-ioniserende stråling: Elektromagnetisk stråling (bølgelengde >100 nm), og ultralyd ₁ , som har liten eller ingen evne til å ionisere.
Strålekilder: Alle ioniserende og sterke ikke-ioniserende strålekilder.
Ioniserende strålekilder: Kilder som avgir ioniserende stråling, f.eks alle typer radioaktive kilder, røntgenapparater, elektronmikroskop
Sterke ikke-ioniserende strålekilder: Kilder som avgir sterk ikke-ioniserende stråling som kan skade helse og/eller ytre miljø, f.eks laser klasse 3B og 4, MR ₂ -systemer, UVC ₃ -kilder, kraftige IR-kilder ₄
<small>¹ Ultralyd er akustisk stråling ("lyd") over det hørbare frekvensområdet (>20 kHz). I strålevernforskriften er ultralyd omtalt sammen med elektromagnetisk ikke-ioniserende stråling. ² MR (eg. NMR) - kjernemagnetisk resonans, metode som nyttes til å «avbilde» indre strukturer i ulike materialer. ³ UVC er elektromagnetisk stråling i bølgelengdeområdet 100-280 nm. ⁴ IR er elektromagnetisk stråling i bølgelengdeområdet 700 nm – 1 mm.</small>

For hver laser skal det finnes en informasjonsperm(HMSRV3404B) som skal inneholde:

- Generell informasjon
- Navn på instrumentansvarlig og stedfortreder, og lokal strålevernskoordinator
- Sentrale data om apparaturen
- Instrumentspesifikk dokumentasjon
- Referanser til (evt kopier av) datablader, strålevernbestemmelser, o.l.
- Vurderinger av risikomomenter
- Instruks for brukere
- Instruks for praktisk bruk; oppstart, drift, avstenging, sikkerhetsforholdsregler, loggføring, avlåsing, evt. bruk av strålingsmåler, osv.
- Nødprosedyrer

Se ellers retningslinjen til NTNU for laser: <http://www.ntnu.no/hms/retningslinjer/HMSR34B.pdf>

7.6 Bruk og behandling av kjemikalier.

Her forstås kjemikalier som grunnstoff som kan utgjøre en fare for arbeidstakers sikkerhet og helse.

Se ellers: <http://www.lovddata.no/cgi-wift/ldles?doc=/sf/sf/sf-20010430-0443.html>

Sikkerhetsdatablar skal være i forøkenes HMS perm og kjemikaliene registrert i Stoffkartoteket.

Kapittel 8 Vurdering av operasjonell sikkerhet

Sikrer at etablerte prosedyrer dekker alle identifiserte risikoforhold som må håndteres gjennom operasjonelle barrierer og at operatører og teknisk utførende har tilstrekkelig kompetanse.

8.1 Prosedyre Hazop

Prosedyre-HAZOP gjennomføres som en systematisk gjennomgang av den aktuelle prosedyren ved hjelp av fastlagt HAZOP-metodikk og definerte ledeord. Prosedyren brytes ned i enkeltstående arbeidsoperasjoner (noder) og analyseres ved hjelp av ledeordene for å avdekke mulige avvik, uklarheter eller kilder til mangelfull gjennomføring og feil.

8.2 Drifts og nødstop prosedyrer

Utarbeides for alle forsøksoppsetninger.

Driftsprosedyren skal stegvis beskrive gjennomføringen av et forsøk, inndelt i oppstart, under drift og avslutning. Prosedyren skal beskrive forutsetninger og tilstand for start, driftsparametere med hvor store avvik som tillates før forsøket avbrytes og hvilken tilstand riggen skal forlates.

Nødstop-prosedyre beskriver hvordan en nødstop skal skje, (utført av uinnvidde), hva som skjer, (strøm/gass tilførsel) og hvilke hendelser som skal aktivere nødstop, (brannalarm, lekkasje).

Kapittel 9 Risikomatrix Tallfesting av restrisiko

For å synliggjøre samlet risiko, jevnfør skjema for risikovurdering, plottes hver enkelt aktivitets verdi for sannsynlighet og konsekvens inn i risikomatriksen. Bruk aktivitetens IDnr. Eksempel: Hvis aktivitet med IDnr. 1 har fått en risikoverdi D3 (sannsynlighet 3 x konsekvens D) settes aktivitetens IDnr i risikomatriksens felt for 3D. Slik settes alle aktivitetenes risikoverdier (IDnr) inn i risikomatriksen.

I risikomatriksen er ulike grader av risiko merket med rød, gul eller grønn. Når en aktivitets risiko havner på rød (= uakseptabel risiko), skal risikoreduserende tiltak gjennomføres. Ny vurdering gjennomføres etter at tiltak er iverksatt for å se om risikoverdien er kommet ned på akseptabelt nivå.

KONSEKVENNS	Svært alvorlig	E1	E2	E3	E4	E5
	Alvorlig	D1	D2	D3	D4	D5
	Moderat	C1	C2	C3	C4	C5
	Liten	B1	B2	B3	B4	B5
	Svært liten	A1	A2	A3	A4	A5
		Svært liten	Liten	Middels	Stor	Svært Stor
SANSYNLIGHET						



Prinsipp over akseptkriterium. Forklaring av fargene som er brukt i risikomatriksen.

Farge	Beskrivelse
Rød	Uakseptabel risiko. Tiltak skal gjennomføres for å redusere risikoen.
Gul	Vurderingsområde. Tiltak skal vurderes.
Grønn	Akseptabel risiko. Tiltak kan vurderes ut fra andre hensyn.

A.2 Risk-report appendix

Vedlegg til Risikovurderingsrapport

Vannkjølt, strømførende spole-element

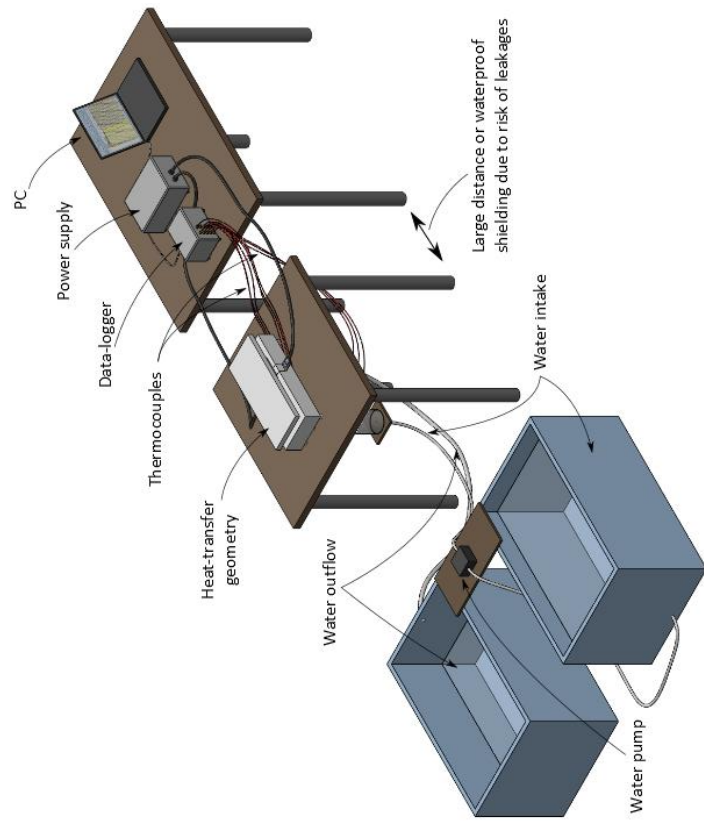
Prosjekttittel	Vannkjøling av et strømførende spole-element
Apparatur	Vannkjølt, strømførende spole-element
Enhet	NTNU
Apparaturansvarlig	Trygve Magne Eikevik
Prosjektleder	Trygve Magne Eikevik
HMS-koordinator	Morten Grønli
HMS-ansvarlig (linjeleder)	Olav Bolland
Plassering	VVSLab
Romnummer	C163
Risikovurdering utført av	Lars Clad og Sigbjørn Lomheim i samarbeid med Håvard Rekstad

INNHOLDSFORTEGNELSE

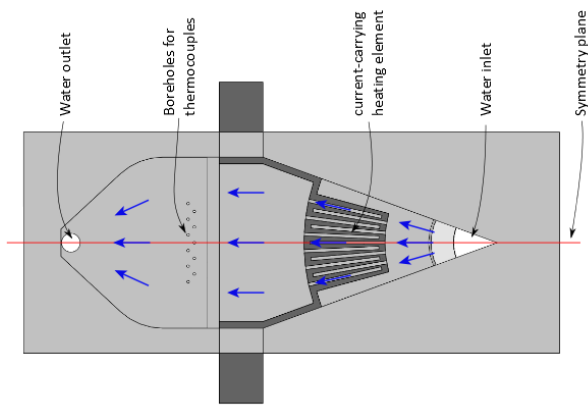
VEDLEGG A: PROSESS OG INSTRUMENTERINGSDIAGRAM.....	1
VEDLEGG B: HAZOP (MAL)	3
VEDLEGG C: PRØVESERTIFIKAT FOR LOKAL TRYKKTESTING.....	8
VEDLEGG D: HAZOP PROSEDYRE (MAL).....	9
VEDLEGG E: FORSØKSPROSEDYRE	10
VEDLEGG F: OPPLÆRINGSPLAN FOR OPERATØRER.....	11
VEDLEGG G: SKJEMA FOR SIKKER JOBB ANALYSE.....	12
APPARATURKORT / UNITCARD.....	14
FORSØK PÅGÅR /EXPERIMENT IN PROGRESS	15

VEDLEGG A: PROSESS OG INSTRUMENTERINGSDIAGRAM

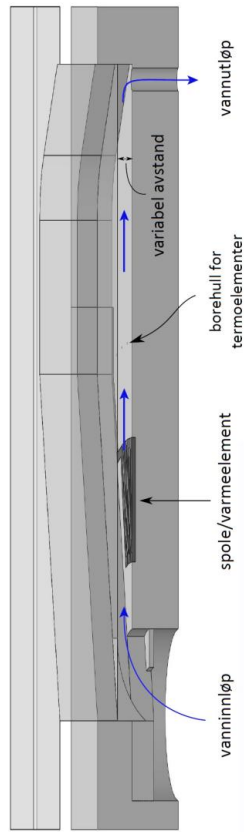
Komponentliste:	
-	Vannpumpe – max. 2,1 Liter/min
-	Transformator som strømforsyning med en spenning mellom 1 og 5 V og en stømstyrke mellom 50 og 100 A
-	Data-logger
-	Termoelmenter
-	PC



Figur 1: Generell eksperiment-oppsett



Figur 2: Top view av varmetest-geometrien



Figur 3: Varmetest-geometrien fra siden.

VEDLEGG B: HAZOP MAL

Project: Vannkjøling av et strømførende spole-element Node 1: Vannkjølt, strømførende spole, VVSLab rom C163		Page:					
Ref#	Guideword	Causes	Consequences	Safeguards	Recommendations	Action	Date/Sign
1	No flow	Feil med vannpumpen, vannslangen til forsøksoppsettet/ lekkasje, eller vanninn-/utløpet er tilstoppet	Spole-elementet blir ikke kjølt	Slå av strømforsyningen til spole-elementet og vannpumpen. Kontroller vannpumpe, vannslange og vanninn- og utløp	Slå av strømforsyningen til instrumenteringen hvis det er fare for at den blir våt.		
2	Reverse flow	Feil med vannpumpe	Spole-elementet blir ikke kjølt	Slå av strømforsyningen til spole-elementet og vannpumpen, kontroller vannpumpen.			
3	More flow	Feil med vannpumpen eller lekkasje	Ved lekkasje blir spole-elementet ikke kjølt bra nok	Slå av strømforsyningen til spole-elementet og vannpumpen. Kontroller vannpumpen og forsøksoppsettet på feil og lekkasje.	Slå av strømforsyningen til instrumenteringen hvis det er fare for at den blir våt.		
4	Less flow	Feil med vannpumpe, lekkasje eller vanninn-/utløpet er tilstoppet	Spole-elementet blir ikke kjølt bra nok.	Slå av strømforsyningen til spole-elementet. Ved lekkasje, slå av strømforsyningen til vannpumpen. Kontroller vannpumpen og forsøksoppsettet.	Slå av strømforsyningen til instrumenteringen hvis det er fare for at den blir våt.		

Project: Vannkjøling av et strømførende spole-element Node 1: Vannkjølt, strømførende spole, VVSLab rom C163						Page:	
Ref#	Guideword	Causes	Consequences	Safeguards	Recommendations	Action	Date/Sign
	More level						
	Less level						
5	More pressure	Vanninn-/utløpet er forstoppet eller spaltebredden er for liten.	Mindre vannstrømm, spole-elementet blir ikke kjølt bra nok.	Kontroller temperaturen på spole-elementet. Slå av strømforsyningen til spole-elementet hvis temperaturen blir høyere enn 140°C. Kontroller spaltebredden og vanninn-/utløpet.			
6	Less pressure	Feil med vannpumpen, lekkasje eller spaltebredden er for stor.	Mindre vannstrømm, spole-elementet blir ikke kjølt bra nok.	Slå av strømforsyningen til spole-elementet (og vannpumpen ved lekkasje). Kontroller vannpumpen og forsøksoppsettet på feil og lekkasje.	Slå av strømforsyningen til instrumenteringen hvis det er fare for at den blir våt.		
7	More temperature	Spole-elementet blir ikke kjølt bra nok.	Forsøksoppsettet kan ta skade hvis temperaturen stiger over 160°C.	Slå av strømforsyningen til spole-elementet. Kontroller vannstrømmen.			
8	Less temperature	Vannstrømmen er for høy eller feil med strømforsyningen til spole-	Ingen		Kontroller vannstrømmen og strømforsyningen til spole-elementet.		

Project: Vannkjøling av et strømførende spole-element Node 1: Vannkjølt, strømførende spole, VVSLab rom C163						Page:	
Ref#	Guideword	Causes	Consequences	Safeguards	Recommendations	Action	Date/Sign
		elementet.					
	More viscosity						
	Less viscosity						
9	Composition Change	Temperaturen på spole-elementet er for høy.	POMen smelter, forsøksoppsettet tar skade.	Slå av strømforsyningen til spole-elementet. Kontroller vannstrømmen.	Slå av strømforsyningen til instrumenteringen hvis det er fare for at den blir våt.		
	Contamination						
	Relief						
10	Instrumentation gets wet	lekkasje	Instrumentene kan ta skade.	Slå av strømforsyningen til spole-elementet, vannpumpen og insturmenteringen.	Forsøk å stoppe vannstrømmen til instrumenteringen og å tørke insturmenteringen.		
	Sampling						
	Corrosion/erosion						
11	Service failure	Vannslangen hopper av	lekkasje	Slå av strømforsyningen til spole-elementet og vannpumpen, stopp lekkasjen.	Kontroller at vannet ikke kommer til insturmenteringen. Slå av strømforsyningen til instrumenteringen hvis det er fare for at den blir våt.		
	Abnormal						



Project: Vannkjøling av et strømførende spole-element Node 1: Vannkjølt, strømførende spole, VVSLab rom C163						Page:	
Ref#	Guideword	Causes	Consequences	Safeguards	Recommendations	Action	Date/Sign
	operation						
	Maintenance						
	Ignition						
	Spare equipment						
	Safety						

Project: Vannkjøling av et strømførende spole-element						Page:	
Node 2: Spenningsforsyning, elektrisk anlegg							
Ref#	Guideword	Causes	Consequences	Safeguards	Recommendations	Action	Date/Sign
1	Skadet isolasjon på kabler og utstyr	Slitasje, brukt utstyr	Strømgjennomgang ved berøring	Bytte ut skadet utstyr med nytt	Kontrollsjekke alt utstyr før det tas i bruk (teste isolasjonsstyrke)		
2	Feil i strømforsyning, kabelbrudd,	Slitasje, brukt utstyr, løse kontakter, varmgang pga løse kontakter	Kortslutning kan føre til brann, varmgang, lysbue.	Nettet som spenningskilden er koblet til har sikringer som slår ut spenningen ved kortslutning	Sjekk kva sikring som er installert på forsyningsnettet		
3	Høy strøm i kabler	Lav motstand i spoleelementet	Kabel blir varm, kan smelte og gi kortslutning	Kabel blir dimensjonert etter NEK-400:2010 for forventet strømstyrke			
4	Strømbrytning under drift	Løse kontakter, kabel faller ut	Fare for lysbue, høyspenning på trafo i kort periode	Kabler er riktig festet slik at det ikke faller av, og ikke ligger slik at andre kommer borti	Dette etter sees kontinuerlig		



VEDLEGG C: PRØVESERTIFIKAT FOR LOKAL TRYKKTESTING

Trykk testen skal utføres i følge NS-EN 13445 del 5 (Inspeksjon og prøving).
Se også prosedyre for trykktesting gjeldende for VATL lab

Trykkpåkjent utstyr:	
Benyttes i rigg:	
Design trykk for utstyr (bara):	
Maksimum tillatt trykk (bara): (i.e. burst pressure om kjent)	
Maksimum driftstrykk i denne rigg:	

Prøvetrykket skal fastlegges i følge standarden og med hensyn til maksimum tillatt trykk.

Prøvetrykk (bara):	
X maksimum driftstrykk: I følge standard	
Test medium:	
Temperatur (°C)	
Start tid:	Trykk (bara):
Slutt tid:	Trykk (bara):
Maksimum driftstrykk i denne rigg:	

Eventuelle repetisjoner fra atm. trykk til maksimum prøvetrykk:.....

Test trykket, dato for testing og maksimum tillatt driftstrykk skal markeres på
(skilt eller innslått)

Sted og dato

Signatur



VEDLEGG D: HAZOP PROSEDYRE (MAL)



VEDLEGG E: FORSØKSPROSEDYRE

Prosjekt Vannkjøling av et strømførende spole-element		Dato/Signatur
Apparatur Vannkjølt, strømførende spole-element		
Prosjektleder Trygve Magne Eikevik	3/5	<i>[Signature]</i>
Operatør(er)		
Lars Clad	3. Mai 2013	<i>[Signature]</i>
Sigbjørn Lomheim	3. Mai 2013	<i>[Signature]</i>

	Conditions for the experiment:	Completed
	Experiments should be run in normal working hours, 08:00-16:00 during winter time and 08.00-15.00 during summer time. Experiments outside normal working hours shall be approved.	
	One person must always be present while running experiments, and should be approved as an experimental leader.	
	An early warning is given according to the lab rules, and accepted by authorized personnel.	
	Be sure that everyone taking part of the experiment is wearing the necessary protecting equipment and is aware of the shut down procedure and escape routes.	
	Preparations	Carried out
	Post the "Experiment in progress" sign.	
	Prepare all equipment for the experiment. Switch on the power supply of the water pump before switching on the power supply of the coil-element.	
	During the experiment	
	Control the water mass flow rate through the experimental setup, log the temperature of the coil, the water temperature at the inlet and outlet and the voltage and current through the coil-element.	
	End of experiment	
	Switch off the power supply of the coil-element, thereafter the power supply of the water pump.	
	Remove all obstructions/barriers/signs around the experiment.	
	Tidy up and return all tools and equipment.	
	Tidy and cleanup work areas.	
	Return equipment and systems back to their normal operation settings (fire alarm)	
	To reflect on before the next experiment and experience useful for others	
	Was the experiment completed as planned and on scheduled in professional terms?	
	Was the competence which was needed for security and completion of the experiment available to you?	
	Do you have any information/ knowledge from the experiment that you should document and share with fellow colleagues?	



VEDLEGG F: OPPLÆRINGSPLAN FOR OPERATØRER

Prosjekt Vannkjøling av et strømførende spole-element	Dato/Signatur
Apparatur Vannkjølt, strømførende spole-element	
Prosjektleder Trygve Magne Eikevik	3/5/2013 - B. Lund

Kjennskap til EPT LAB generelt		
Lab		
- adgang		
-rutiner/regler		
-arbeidstid		
Kjenner til evakueringsprosedyrer		
Aktivitetsskalender		
Innmelding av forsøk til: iept-experiments@ivt.ntnu.no		
Kjennskap til forsøkene		
Prosedyrer for forsøkene		
Nødstop		
Nærmeste brann/førstehjelpsstasjon		

Jeg erklærer herved at jeg har gjennomgått og forstått HMS-regelverket, har fått hensiktsmessig opplæring for å kjøre dette eksperimentet og er klar over mitt personlige ansvar ved å arbeide i EPT laboratorier.

Operatører

Navn	Dato	Signatur
Lars Clad	3. Mai 2013	
Sigbjørn Lomheim	3. Mai 2013	



VEDLEGG G: SKJEMA FOR SIKKER JOBB ANALYSE

SJA tittel:	
Dato:	Sted:
Kryss av for utfylt sjekkliste:	

Deltakere:		
SJA-ansvarlig:		

Arbeidsbeskrivelse: (Hva og hvordan?)
Risiko forbundet med arbeidet:
Beskyttelse/sikring: (tiltaksplan, se neste side)
Konklusjon/kommentar:

Anbefaling/godkjenning:	Dato/Signatur:	Anbefaling/godkjenning:	Dato/Signatur:
SJA-ansvarlig:		HMS koordinator	
Ansvarlig for utføring:		Annen (stilling):	
HMS aspekt	Ja	Nei	NA
Kommentar / tiltak			Ansv.



Dokumentasjon, erfaring, kompetanse					
Kjent arbeidsoperasjon?					
Kjennskap til erfaringer/uønskede hendelser fra tilsvarende operasjoner?					
Nødvendig personell?					
Kommunikasjon og koordinering					
Mulig konflikt med andre operasjoner?					
Håndtering av en evt. hendelse (alarm, evakuering)?					
Behov for ekstra vakt?					
Arbeidsstedet					
Uvante arbeidsstillinger?					
Arbeid i tanker, kummer el.lignende?					
Arbeid i grøfter eller sjakter?					
Rent og ryddig?					
Verneutstyr ut over det personlige?					
Vær, vind, sikt, belysning, ventilasjon?					
Bruk av stillaser/lift/seler/stropper?					
Arbeid i høyden?					
Ioniserende stråling?					
Rømningsveier OK?					
Kjemiske farer					
Bruk av helseskadelige/giftige/etsende kjemikalier?					
Bruk av brannfarlige eller eksplosjonsfarlige kjemikalier?					
Er broken risikovurdert?					
Biologisk materiale?					
Støv/asbest/isolasjonsmateriale?					
Mekaniske farer					
Stabilitet/styrke/spenning?					
Klem/kutt/slag?					
Støy/trykk/temperatur?					
Behandling av avfall?					
Behov for spesialverktøy?					
Elektriske farer					
Strøm/spenning/over 1000V?					
Støt/krypstrøm?					
Tap av strømtilførsel?					
Området					
Behov for befaring?					
Merking/skilting/avsperring?					
Miljømessige konsekvenser?					
Sentrale fysiske sikkerhetssystemer					
Arbeid på sikkerhetssystemer?					
Frakobling av sikkerhetssystemer?					
Annet					

APPARATURKORT

Enhet (unit) og bygg/romnr. (building/room no.):

NTNU-E 302 C163 1. etg

Laboratorium

VVSLab

Dette kortet SKAL henges godt synlig ved maskinen!
This card MUST be posted on a visible place on the unit!

Apparatur (Unit) Vannkjølt, strømførende spole-element	Dato Godkjent (Date Approved) 6. mai 2013
Prosjektleder (Project Leader) Trygve Magne Eikevik	Telefon mobil/privat (Phone no. mobile/private) 930 59 196
Apparaturansvarlig (Unit Responsible) Trygve Magne Eikevik	Telefon mobil/privat (Phone no. mobile/private) 930 59 196
Sikkerhetsrisikoer (Safety hazards) Vannlekkasje; Varmt spole-element, berøringsfare; Fare for strømgjennomgang, berøringsfare	
Sikkerhetsregler (Safety rules) Operatøren har stadig tilgang til strømbryteren til spole-elementet og vannpumpen	
Nødstopprosedyre (Emergency shutdown) Slå av strømforsyningen til spole-elementet og vannpumpen.	
Her finner du (Here you will find):	
Prosedyrer (Procedures)	Ved riggen
Bruksanvisning (User manual)	Ved riggen
Brannslukningsapparat (Fire extinguisher)	1. etasje VVSLab (syd)
Førsthjelpsskap (First aid cabinet)	1. etasje VVSLab (syd)

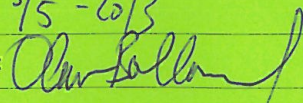
NTNU

Institutt for energi og prosessteknikk

Dato

3/5 - 2013

Signert




FORSØK PÅGÅR

Enhet (unit) og bygg/romnr. (building/room no.):

NTNU-E 302 C163 1. etg

Laboratorium VVSLab

Dette kortet SKAL henges opp før forsøk kan starte!
This card MUST be posted on the unit before the experiment startup!

Apparatur (Unit) Vannkjølt, strømførende spole-element	Dato godkjent (Date Approved) 6. mai 2013		
Prosjektleder (Project Leader) Trygve Magne Eikevik	Telefon mobil/privat (Phone no. mobile/private) 930 59 196		
Apparaturansvarlig (Unit Responsible) Trygve Magne Eikevik	Telefon mobil/privat (Phone no. mobile/private) 930 59 196		
Godkjente operatører (Approved Operators)	Navn/Name	Telefon/Phone	Mobil
	Clad, Lars		45174489
	Lomheim, Sigbjørn		
Prosjekt (Project) Vannkjølt, strømførende spole-element			
Forsøksstid / Experimental time (start - stop) 06.05.2013 - 31.12.2013			
Kort beskrivelse av forsøket og relaterte farer (Short description of the experiment and related hazards) Et strømførende spole-element blir kjølt med vann for å måle det gjennomsnittlige varmeovergangstallet mellom vann og spole-elementet. Relaterte farer: Vannlekkasje; Varmt spole-element, berøringsfare; Fare for strømgjennomgang, berøringsfare.			

NTNU

Institutt for energi og prosessteknikk

Dato 3/5-2013

Signert

 NTNU

 SINTEF